POLITECNICO
MILANO 1863

SCUOLA DI INGEGNERIA INDUSTRIALE
E DELL'INFORMAZIONE

Executive Summary of the Thesis

# An engineering model for power generation estimation of Airborne Wind Energy Systems

Laurea Magistrale in Energy Engineering - Ingegneria Energetica

**Author:** Gregorio Pasquinelli

**Advisor:** Prof. Alessandro Croce

**Co-advisors:** Prof. Carlo Emanuele Dionigi Riboldi, Filippo Trevisi

**Academic year:** 2021-2022

## 1. Introduction

Airborne Wind Energy (AWE) is a new renewable energy sector which aims to harvest energy from high-altitude winds with tethered flying devices (kites). The pioneer of the technology is Miles L. Loyd with his paper published in the '80s [1]. The main potential advantage of Airborne Wind Energy Systems (AWESs) compared to conventional wind turbines is the exploitation of the higher quality wind resource with an extremely lower amount of material for the same power output.
In the thesis, the focus is on crosswind AWESs which can be divided into two categories, based on the generation type. Ground Generation Airborne Wind Energy Systems (GG-AWESs) are based on the so-called 'pumping cycles'. During the production phase, the kinetic power in the wind is transformed by the flying device in traction power that unwinds the tether. The reel-out makes the ground generator to rotate and to generate power. During the retraction phase the kite is brought back with minimum energy requirement. Fly Generation Airborne Wind Energy Systems (FG-AWESs) produce power with on-board wind turbines and transmit it to the ground using electric cables embedded in the tether.
The sector is evolving and many start-ups are emerging. One of the main, Makani, has developed a cutting-edge FG-AWES prototype of the $MW$ scale flying circular trajectory. Makani recently stopped activities and published all the findings in three technical reports. In addition to Makani, other start-ups are studying several different concepts since there is no certainty about which technology is the best and which are the most suitable features. To improve the fundamental knowledge, on its 2021 report about AWE, NREL states that one of the main academic research goals must be to increase the simulation environment through low, medium and high-fidelity models.
Since most of the models in the literature have little focus on analytical analysis, the thesis aims to estimate the power generation of generic crosswind AWESs introducing a quasi-analytical model.
This introduction is a summary of the first part of the thesis including the first chapter. In the following, each section of the summary represents a chapter of the thesis and reports the relevant findings.

## 2. Physical modelling of generic crosswind AWESs

In Chapter 2 of the thesis, a semi-analytical model related to power generation of generic AWESs is introduced. The model can be considered a generalization of the one introduced by Trevisi et al. in [2] which investigates the effects of centrifugal forces on FG-AWESs flying circular path. The proposed model considers elevation, gravity and centrifugal forces and it is representative of both FG-AWES and GG-AWES, and, above all, it is suitable also for non-circular trajectories. For this reason it is called as Generic Model for Tethered Kites (GeMo-KiTe). For the model derivation, the cylindrical reference system present in Figure 1 is adopted. The main assumptions needed are reported:

i. The forces acting on a wing are condensed into a single point which is a point mass representation of the kite.
ii. The span-wise direction, represented by the unit vector $\vec{s}$, is always perpendicular to the relative wind velocity.
iii. Constant lift coefficient $C_L$ and drag coefficient $C_D$.
iv. The tether is considered inelastic without any sagging.
v. Constant and uniform wind speed.
vi. High system glide ratio.
vii. The radial kite speed is much lower compared to the kite tangential speed.
viii. The axial kite speed is much lower compared to the kite tangential speed.

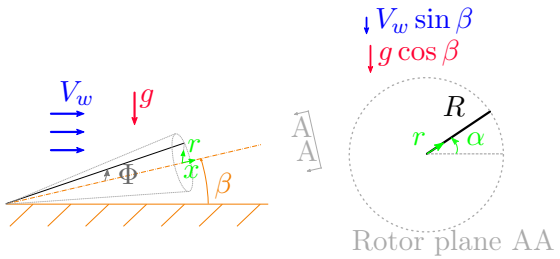


Figure 1: Reference system

The starting point of the model derivation is the prescription of the trajectory. In these sense, three vectors relating to the kite behaviour are defined in the aforementioned cylindrical reference system. The first represents the kite position, in which the axial, $x$, and radial, $r$, components are left as generic functions, $x(\alpha)$ and $r(\alpha)$, of the angular position $\alpha$. Then, the kite speed and acceleration vectors are found through the derivatives. Defining the relative wind velocity $V_a$ felt by the kite, the lift and drag forces can be found as a function of $\alpha$ and of the span-wise vector components, $s_x$, $s_\alpha$ and $s_r$.

At this point, the axial, radial and tangential equilibrium can be written. The problem is characterized by 7 equations: the three force balances, $|\vec{s}| = 1$, $\vec{V}_a \cdot \vec{s} = 0$ (Hp. (ii)), $r = r(\alpha)$ and $x = x(\alpha)$. The 7 time-dependent unknowns are: the three components of $s$, the tether traction force $T$, $\alpha$, $r$, $x$. The last two are identified by the prescription of the trajectory through the explication of $x(\alpha)$ and $r(\alpha)$.

By solving the system, it is possible to find the equations related to the kite attitude, motion and tether traction as a function of only $\alpha$ and $\dot{\alpha}$. Therefore, the equations can be written in a quasi-closed form solution that can be implemented in a time-marching code to quickly obtain the results. Having solved the kite motion, the power generation and the efficiency of the system can be found.

The advantage of this model is that the parameterization of the trajectory and its prescription are independent of the closure of the equations of motion. Different trajectories can be prescribed, by defining $x(\alpha)$ and $r(\alpha)$, and relative power generation estimated.

## 3. Power generation of FG-AWESs flying circular path

In Chapter 3 of the thesis, the GeMo-KiTe is used to derive the equations in the case of FG-AWESs flying circular path. In particular, functions $x(\alpha)$ and $r(\alpha)$ are made explicit to represent the circular path. The obtained equations are referred to as the Circular Model for Fly Generation Tethered Kites (CiMo-FG-KiTe). To understand the main physical effects related to elevation, centrifugal and gravity forces, the results are shown by steps.

### 3.1. Analyses with no elevation and no gravity

The results, shown in Figure 2, turn out to be identical to those derives by Trevisi et. al. in [2] since only centrifugal forces are considered. Therefore, the efficiency, the optimal optimal opening angle $\Phi$ and the optimal non-

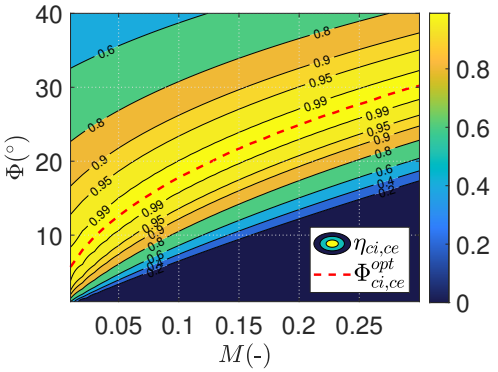


Figure 2: $\eta_{ci,ce}$ as a function of $M$ and $\Phi$

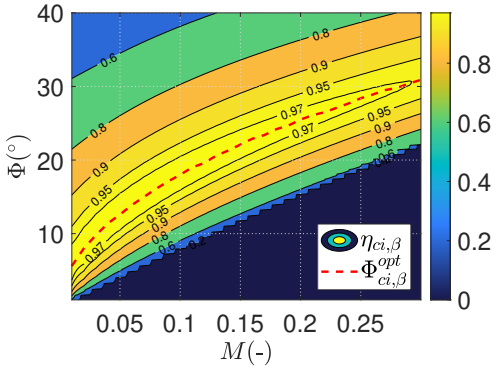


Figure 3: $\eta_{ci,\beta}$ as a function of $M$ and $\Phi$

dimensional parameter $M$ can be found with the analytical expression present in [2]. $M$ represents the ratio between centrifugal and aerodynamic forces [2]. In the optimal conditions, the efficiency is unitary. In the figure, the dark-blue zone, called 'no-fly zone', represents the conditions for which the kite is not able to fly. The parameters related to this analysis have the subscript $ci, ce$.

Power losses are present when $\Phi \neq \Phi^{opt}_{ci,ce}$ because the tether traction does not balances the centrifugal force. The kite rolls to provide a radial component of the aerodynamic resultant which ensure equilibrium. The roll angle reduces the effective wind speed and so the power extraction.

### 3.2. Analysis with Elevation and no Gravity

If elevation is considered together with centrifugal forces, power losses are present even in the optimal conditions. Higher is the elevation, higher are power losses. However, they turn out to be very limited in numerical terms. The results in the case of a mean elevation angle $\beta = 40°$ are show in Figure 3 and the related parameters have the subscript $ci, \beta$.

Power losses due to elevation are caused by the roll angle and the kite speed variation during the loop. Both effects are due to the slight upwind (ascending phase) and downwind (descending phase) motion which determines the presence of a wind speed component in the rotor plane. From one side, it alters the radial equilibrium promoting the kite roll. On the other side, it causes the kite to accelerate or decelerate making the slower part of the motion more relevant over time than the faster part and causing efficiency loss.

### 3.3. Analysis with Gravity and no Elevation

The results, if gravity together with centrifugal forces is considered, are shown in Figures 4 and 5. The related parameters have the subscript $ci, g$. The results are expressed as a function of the non-dimensional parameter $G_r$, introduced in this thesis. It represents the ratio between the gravity and centrifugal forces or, alternatively, the ratio between the potential energy exchange in the loop and the kinetic energy.

Figure 4 shows the maximum efficiency as a function of $M$ and $G_r$. Higher are $G_r$ and $M$, higher is the gravity influence and lower is efficiency. The presence of gravity causes a large no-fly zone: above certain values of $M$ and $G_r$, the kite is not able to fly. The causes of power losses are again the speed variation and the kite roll angle. The first phenomena is due to the tangential component of the gravitational force in the rotor plane that makes the kite accelerate or decelerate. As for the second, the radial component makes the kite rolls to ensure radial balance. Moreover, the upper half of the loop results to be more penalizing.

Figure 5 shows the optimal opening angle as a function of $M$ and $G_r$. Given a certain $M$, higher is $G_r$, lower is $\Phi^{opt}_{ci,g}$. Knowing from Figure 1 that $R = l_t \sin\Phi$ ($R$ is the circular path radius and $l_t$ is the constant tether length), lower $\Phi^{opt}_{ci,g}$ translates in narrower path. The optimal path radius is lower because it limits power losses due to gravity. It provides benefits in terms of roll angle in the more impactful upper half of the

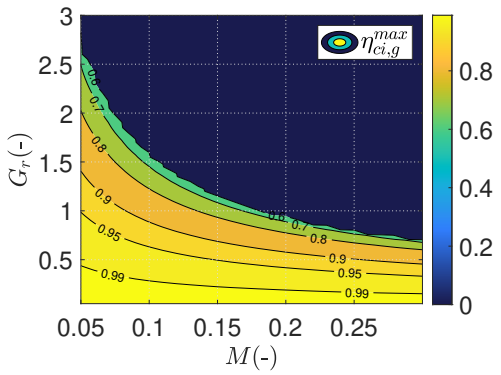


Figure 4: $\eta^{max}_{ci,g}$ as a function of $M$ and $G_r$

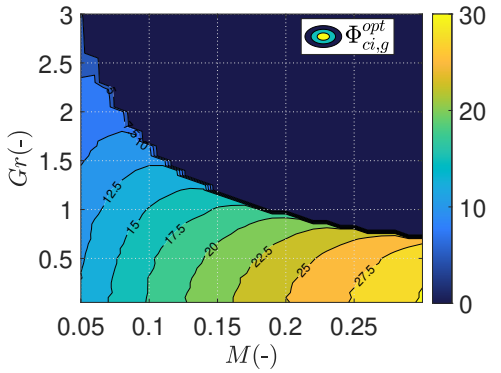


Figure 5: $\Phi^{opt}_{ci,g}$ as a function of $M$ and $G_r$

loop and in terms of speed variation since the potential energy exchange in the loop is reduced.

### 3.4. Analysis with all phenomena

The main finding of considering all phenomena together is the penalizing effects of the coupling between gravity and elevation. The results are shown in Figure 6, in the case of $\beta = 30°$, as a function of $M$ and $G_r$ and the related parameters have the subscript $ci$.

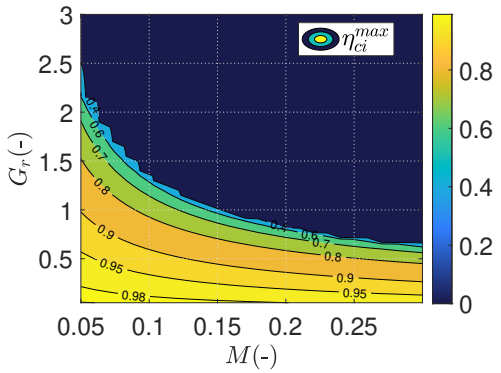


Figure 6: $\eta^{max}_{ci}$ as a function of $M$ and $G_r$

The addition of elevation does not affect the qualitative shape of the trend but enlarge the no-fly zone. Moreover, comparing with Figure 4, efficiency values are decreased noticeably. When only the elevation is considered, its influence on energy generation is negligible, when instead it is considered together with gravity there are non-linear effects that penalize system performance.

## 4. Derivation of Makani Model and comparison

In Chapter 4 of the thesis, the simple analytical model proposed by Makani in [3] for FG-AWESs flying circular path is derived, analyzed and compared with the CiMo-FG-KiTe. The assumptions of the model are the same reported for the GeMo-KiTe.

### 4.1. Model derivation

Makani's team aims to decouple power losses to derive an analytical expression for each contribution. Therefore, the power equation becomes: $P = C_1 C_2 \dots C_n P_{id}$ where $P_{id}$ is the ideal power generation obtained with no elevation angle and $C_1, C_2, \dots, C_n$ are power coefficients related to each power losses. Those considered are the ones related to elevation, centrifugal and gravity forces.

The power factor related to centrifugal effects is derived knowing that the centrifugal force makes the kite rolls. The roll angle reduces the effective wind speed and the related power losses are represented by the cosine of the roll angle at the cube.

To model the gravity effects, Makani's team assumes that:

1. The average kite speed is the average with respect to the angular position rather than to time. With this assumption, it is not considered that more time is spent in the slower portion of the loop than the faster one.
2. Instant by instant, the weight force is the only cause of the kite acceleration as it is assumed that the other forces balance each other.

From assumption 2, the power factor is written as a function of the kite speed. Then, the latter is expressed as a function of the loop angle thanks to hypothesis 1.

The power factor related to power losses due

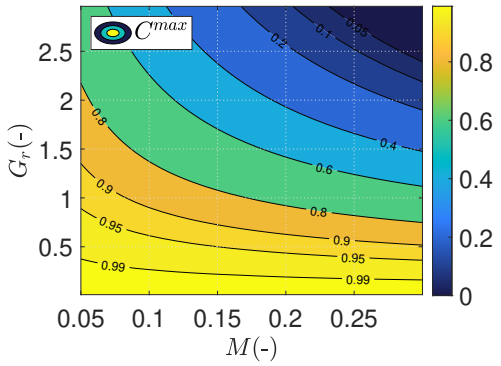


Figure 7: Results of Makani Model: $C^{max}$ as a function of $M$ and $G_r$ without considering elevation

to elevation is represented by the cosine of the mean elevation angle at the cube.

### 4.2. Comparison

For a better clarity, the comparison is divided into two steps: comparison without considering elevation and then with it.
Figure 7 shows the power coefficient without including elevation as a function of $M$ and $G_r$. Comparing with Figure 4, strong similarities are present for low values of $M$ and $G_r$. The main difference is in the no-fly zone. It is almost absent in the case of the Makani results because of mainly hypothesis 2.
Regarding the results with elevation, they are extremely similar to those without elevation in Figure 7. Therefore, the differences with Figure 6 are quite evident. By modeling the power losses for elevation with $\cos\beta^3$ and decoupling the various contributions, Makani's team does not catch the penalizing non-linear effect due to the combination between gravity and elevation.

## 5. Performance enhancement through non-circular trajectories

After using the proposed model to understand the effects of the main phenomena and after having shown its better modelling of physics, Chapter 5 introduces a methodology that exploits the GeMo-KiTe to investigate performance enhancement through flying non-circular trajectories.
Starting from the circular path, the analysis focuses on a three-dimensional trajectory having

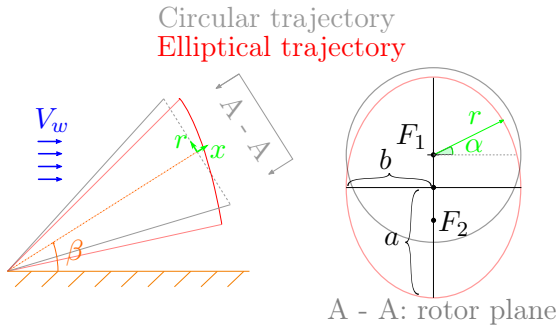


Figure 8: 3D path with elliptical projection on the rotor plane

an elliptical shape as a projection on the rotor plane. Figure 8 shows the orbit in a qualitative way. Through the elliptical path the tether is actively used to reduce the roll angle of the kite during the motion. On the contrary, the vertical range is increased together wind the potential energy exchange that might lead to higher velocity fluctuation and related power losses.
As for the derivation, the functions $r(\alpha)$ and $x(\alpha)$ are defined to prescribed the elliptical orbit. The results show that given a certain $M$, the larger $G_r$, the more promising the ellipse appears to be in terms of energy output. Indeed, higher is $G_r$, lower is $\Phi^{opt}$ and so is the vertical range. In these conditions, power losses due to roll angle are relatively higher than those to speed variation. Consequently, the ellipse is beneficial for system performance.
In the last part of the chapter, other promising trajectories, which can be analyzed with this methodology, are discussed. However, intuitively, the best flight path may depend on the conditions expressed by $M$, $G_r$ and $\beta$.

## 6. Conclusions

In this thesis, the main physical phenomena present in the AWESs are analyzed through the use of a new quasi-analytical model related to power generation.
Firstly, the derivation of a quasi-analytical model (GeMo-KiTe) for a generic crosswind AWES flying a generic trajectory is derived. The model considers centrifugal, elevation and gravity effects leaving the equations as a function of a generic trajectory. No model in the literature concerning the mentioned phenomena presents such a thorough approach to the analytical derivation and closure of equations.

Then, the model is applied for FG-AWES flying a crosswind circular trajectory. A detailed presentation of how centrifugal forces, elevation and gravity affect the kite attitude and the system performance is shown. Two contributions summarize how these three phenomena affect efficiency: power losses due to kite roll and power losses due to kite speed variation during the loop. The effects of elevation on power losses and, in particular, its coupling with gravity turn out to be extremely penalizing. All the discussion is carried out in function of two non-dimensional terms. One of them, $G_r$, represents the ratio between the gravity and centrifugal forces and has been introduced for the first time in this thesis.
In the following, the analytical model proposed by Makani is derived and compared with the CiMo-FG-KiTe. The assumption made by Makani's team for which all the kite acceleration is due to the weight force, while the other forces are constantly in equilibrium, does not match, above certain values of $M$ and $G_r$, results predicted by CiMo-FG-KiTe. Moreover, the power losses decoupling made by Makani's team does not catch the degrading effects due to the combination of gravity and elevation. The results show that a further progress is made in the physics modeling through a low-fidelity model such as the CiMo-FG-KiTe (and so the GeMo-KiTe).
The last part of the thesis shows a qualitative methodology that exploits the GeMo-KiTe to investigate performance enhancement through flying non-circular trajectories. With this aim, the elliptical path is analyzed. The results show that this orbit has the potential to increase performance especially when the power losses due to kite roll are relatively higher than those due to kite speed variation. The higher is $G_r$, the more likely this condition is met. In addition, hints to investigate other promising non-circular trajectories are given.
This work can be useful to AWE community to enrich the basic physical knowledge about the main phenomena present in AWESs. Researchers could use the GeMo-KiTe to study, in a conceptual design phase, the main physical effects of design quantities on system performance and investigate non-circular trajectories to enhance power generation.

## 7. Acknowledgements

I want to acknowledge Università di Pisa, which taught me the right approach to face many challenges of the academic world.
I acknowledge Politecnico di Milano, which allowed me to broaden my vision of the energy sector and to focus my studies on renewable energy. I acknowledge my advisor Prof. Alessandro Croce and co-advisors Prof. Carlo Emanuele Dionigi Riboldi and Filippo Trevisi for allowing me to write this work and discover AWE. I only became aware of this sector nine months ago, but my passion has grown and I hope this thesis is just the beginning of a new journey.
Thanks to all my friends, from the oldest, to those met in Pisa and in Milano. For all the moments of fun and reflection over the years and for teaching me so many things that I hope to always carry with me, thanks.
Thanks to my family that allowed me to live such an incredible experience and that supports my studies in Milan. Thanks, mom and dad. Thank you, brother and sisters. Thanks to all the other components.
Thanks to my girlfriend, Matilde, for understanding me in times of pressure, for trying to cheer me up in times of difficulty and for rejoicing with me in times of happiness. I hope to give you at least half of what you have given me so far.

## References

[1] Loyd, Miles L. Crosswind Kite Power. *Journal of energy*, 4(3):106–111, 1980.

[2] Filippo Trevisi, Mac Gaunaa, and Michael Mcwilliam. The Influence of Tether Sag on Airborne Wind Energy Generation. In *Journal of Physics: Conference Series*, volume 1618, page 032006. IOP Publishing, 2020.

[3] Paula Echeverri, Tobin Fricke, Geo Homsy, and Nicholas Tucker on behalf of the Makani team. *The energy kite: Selected Results from the Design, Development and Testing of Makani's Airborne Wind Turbines. Part I*, 2020.

POLITECNICO
MILANO 1863

SCUOLA DI INGEGNERIA INDUSTRIALE
E DELL'INFORMAZIONE

# An engineering model for power generation estimation of crosswind Airborne Wind Energy Systems

Tesi di Laurea Magistrale in
Energy Engineering - Ingegneria Energetica

Author: **Gregorio Pasquinelli**

Student ID: 944027
Advisor: Prof. Alessandro Croce
Co-advisors: Prof. Carlo Emanuele Dionigi Riboldi, Filippo Trevisi
Academic Year: 2021-22

# Abstract

This thesis aims to investigate the power generation of Airborne Wind Energy Systems (AWESs) through a generic quasi-analytical model.
The model considers centrifugal, elevation and gravity effects leaving the equations as a function of a generic flight path. The model can be helpful for Airborne Wind Energy (AWE) researchers to study the physical effects of the main design quantities on system performance and to study potential improvements of the trajectory.
The generic model is used to derive the equations relating to Fly Generation Airborne Wind Energy Systems (FG-AWESs) with circular flight path. Implementing the equations in a time-marching code, an analysis of power losses due to centrifugal, gravity and elevation effects is carried out. The results are shown as a function of two non-dimensional parameters, one of which, relating to gravitational effects, is defined for the first time in this thesis. The power losses related to the aforementioned phenomena are caused by the roll of the aircraft and its speed variation during motion. The effects of elevation and gravity are relevant and their coupling results to be very penalizing.
In the following part of the thesis, the analytical model proposed by Makani, a reference company in the sector, is presented. The model relates to FG-AWESs with circular flight path. A comparison between the latter and the quasi-analytical model proposed in the thesis is carried out. The Makani model turns out to be less general due to stronger hypotheses. These results show that a further progress is made in the physics modeling through a low-fidelity model such as the one proposed.
Finally, a methodology that exploits the semi-analytical model to investigate non-circular trajectories is presented for FG-AWESs. The elliptical orbit is proposed and investigated. The results show that the elliptical path has the potential to increase performance especially for conditions in which the power losses due to kite roll angle are relatively higher than those for kite speed variation. Besides the qualitative results obtained for the ellipse, this approach can be useful for AWE researchers to evaluate the impact of non-circular trajectories on system performance.

**Keywords: Airborne Wind Energy, Engineering modeling, Power generation, AWE physics, Makani, Optimal flight path**

# Abstract in lingua italiana

La tesi ha l'obbiettivo di studiare la generazione di energia dei sistemi che sfruttano i venti di alta quota attraverso un generico modello semi-analitico.
Il modello tiene conto degli effetti centrifughi, dell' elevazione e della forza di gravità lasciando le equazioni in funzione di una traiettoria generica. Il modello può essere utile per i ricercatori del settore per studiare gli effetti dei principali parametri di progetto sulle prestazioni del sistema e per studiare potenziali miglioramenti della traiettoria di volo.
Il modello generico è sfruttato per derivare le equazioni nel caso di sistemi con generazione a bordo aventi traiettoria circolare. Dopo aver implementato le equazioni in un codice time-marching, è svolta un'analisi delle perdite di potenza dovute agli effetti centrifughi, gravitazionali e dell'elevazione. I risultati sono mostrati in funzione di due parametri adimensionali di cui uno, relativo agli effetti gravitazionali, è definito per la prima volta in questa tesi. Le perdite di potenza relative a tali fenomeni sono causate dal rollio del velivolo e dalla variazione di velocità durante il moto. Sia gli effetti dell'elevazione che della gravità sono rilevanti e il loro accoppiamento risulta essere molto penalizzante.
Nella parte successiva della tesi viene presentato il modello analitico proposto da Makani, un'azienda di riferimento del settore. Il modello è relativo ai sistemi con generazione a bordo aventi traiettoria circolare. Viene quindi effettuato un confronto tra quest'ultimo e il modello semi-analitico proposto nella tesi. Il modello di Makani risulta essere meno generale a causa delle ipotesi più stringenti. Questo dimostra che sono state apportate migliorie nello sviluppo e nella generalizzazione di modelli a bassa fedeltà per sistemi che sfruttano i venti di alta quota.
Infine, è presentata una metodologia che utilizza il modello semi-analitico per studiare traiettorie diverse da quella circolare. Viene così analizzata l'orbita ellittica. I risultati mostrano che ha il potenziale per aumentare le prestazioni nelle condizioni in cui le perdite di potenza dovute al rollio del velivolo sono relativamente maggiori di quelle per variazione di velocità. Oltre ai risultati relativi all'ellisse, la metodologia presentata può essere utile ai ricercatori del settore per valutare l'impatto di nuove traiettorie sulle prestazioni.

**Parole chiave: Eolico di alta quota, Modellazione ingegneristica, Generazione di potenza, Fisica dei sistemi AWE, Makani, Traiettoria ottimale**

# Contents

# Introduction

From the energy of the animals to the energy of the fire, from the watermills and the windmills to the use of the coal. Since ancient times strict relationship intercourse between human beings and energy. In the same way, today, the advancement of society and increase in the global population are closely related to changes in the amount and type of energy available to satisfy human needs [1].

Nowadays, humanity has to face two incredible challenges: making access to energy affordable to the increasing population and making it in a clean and sustainable way to limit the climate change effects. The world has already heated up by more than a Celsius degree. The consequences start to be irreversible. There is no more time. People's lifestyle, industrial production processes, food supply and mobility need a drastic change. World electrification seems to be the key.
From the electricity production side, the switch from conventional fossil fuels to renewable energies must go hand in hand. In addition to the well-known environmental sustainability, there are many other advantages brought by the spread of renewables: security of supply, economic affordability and disaster risks [2]. In this scenario, Europe has set the goal to become climate neutral by 2050.

As mentioned in the 2021 IEA report 'Net Zero by 2050' [3], most of the reductions in CO2 emissions through 2030 will come from technologies already on the market today (solar and conventional wind firsts). From 2030 onwards, almost half the reductions will have to come from technologies that are currently at the demonstration or prototype phase. Major innovation efforts must take place this decade to bring these new technologies to market in time [3].

In this context, the importance of a completely new renewable energy sector, Airborne Wind Energy (AWE), is clear. AWE aims at capturing wind energy at significantly increased altitudes with tethered flying devices. Systems that harvest this kind of energy can be referred to as Airborne Wind Energy Systems (AWESs).
In the early 1800s, George Pocock (1774-1843) used high altitude winds for the first time to generate power [4]. His invention, the "Charvolant", was a kite-drawn carriage patented

in 1826. For the first scientific investigation, the 1980s must be expected when M. L. Loyd [5] described the physics of kites flying crosswind with a short paper.
Only from the 2000s, the electronics allow AWE to become a realistic way of extracting power from the wind. In the last decade, progress has been made and many start-ups have been born. One of the main, Makani, has developed a 600 $kW$ prototype and tested it both on-shore and off-shore. Makani shut down operations in September 2020, but its team published all the outcomes and learning of their 13-years research into three open-to-access reports [6–8]. Fortunately, other companies are close to launching the first commercial products and the scientific interest is increasing among the research community.

## Motivations and goals

The AWE sector is in turmoil. Many start-ups are providing many different solutions and coming up with new ideas but scientific certainties are few. Academic research must spread and set milestones on which industries can rely. For this purpose, IEA has created Task 48 this year to 'build a strong community that works together to identify and mitigate the barriers to the development and deployment of airborne wind energy systems' [9]. In its 2021 report on AWE [10], NREL identifies some key academic research goals needed for the AWE development. Among few others, academic research must increase the simulation environment through the use of low, medium and high-fidelity models. Citing NREL:

*'Low-fidelity models yield results in a very short amount of time, but the accuracy or applicability is dictated by the underlying assumptions of the model. These models can be used for design exploration, [...] are often analytical, steady-state, first-order approximations with a runtime for a single data point on the order of a fraction of a second. These types of models enable system developers to explore how the topology of a concept impacts performance and enable technology trade-offs.[10]'*

Since most of the models in the literature are numerical with little focus on analytical analysis, as explained in Chapter 2, the thesis aims to estimate the power generation of generic AWESs introducing a quasi-analytical model. Moreover, attention is focused on the analytical model proposed by Makani in its first report [6]. Both models belong to the above mentioned category of low-fidelity models and enrich the knowledge about the physics relating to the characteristic phenomena of AWESs and can be useful for design exploration. In particular, the goal of the thesis is to exploit them to qualitatively understand how centrifugal forces, elevation and gravity affect power generation. The final goal is to propose a methodology in which the proposed model is used to investigate performance enhancement through flying non-circular trajectories.

## Structure of the thesis

This thesis is divided into five chapters.

In Chapter 1, an overview of the AWE is provided. The novel ideal of AWE and the advantages of the technology with respect to conventional wind turbines are described. Then, the differences between Ground Generation Airborne Wind Energy Systems (GG-AWESs) and Fly Generation Airborne Wind Energy Systems (FG-AWESs) are shown. Finally, the major actors of the sector are presented.

Chapter 2 describes, starting from the known models from literature, the derivation of a quasi-analytical model for a generic AWES flying a generic trajectory. The new model is the so-called Generic Model for Tethered Kites (GeMo-KiTe).

In Chapter 3, a model for a FG-AWES flying a circular path is derived from the GeMo-KiTe. The derived model is the so-called Circular Model for Fly Generation Tethered Kites (CiMo-FG-KiTe). Then, the main physical phenomena and the related power losses are analyzed by steps before considering them all together.

In Chapter 4, the analytical model for FG-AWESs flying circular paths proposed by Makani is derived and discussed. Then, a comparison between the latter and the CiMo-FG-KiTe is performed and critically commented.

In Chapter 5, a methodology that exploits the GeMo-KiTe to analyze the effects of non-circular trajectories on system performance is presented. The potential of the elliptical trajectory is shown together with other promising paths.

In Chapter 6, some possible future works are proposed.

Finally, Chapter 7 gathers the main findings of this thesis.

# 1 | Overview of the Airborne Wind Energy Sector

In this first chapter, an overview of the AWE sector is given. In particular, an overview of AWESs flying crosswind is presented.

In the first section it is explained the novel idea related to the technology and why it is so promising with respect to conventional wind energy. Then, an overview of the technology is presented, followed by a third section showing the major players in the sector with their prototypes and products.

## 1.1. Motivations and concepts

As stated by Marvel et. al. in [11], there is enough power in Earth's winds to be a primary source of near-zero-emission electric power. Nowadays, the energy carried by the wind is transformed by Horizontal Axis Wind Turbines (HAWTs) placed on Earth's surface. Nevertheless, high-altitude winds are usually steadier and faster than near-surface winds, resulting in higher average power densities. Marvel et. al. show that the global maximum kinetic power extraction from high altitude winds is about 4 times the global energy demand and can be more than 4 times the maximum kinetic power extracted from the near-surface winds [11].

The comparison of wind resources at different altitudes is also performed by Archer et. al in [12, 13]. Since both wind speed and air density vary with height, the correct comparison parameter is power density. Figure 1.1 shows that few sites around the world are suitable for conventional wind turbines (left picture relating to 80 $m$ above the ground). Instead, looking at the central and right pictures, accessing wind at higher altitudes makes the interesting locations much more numerous. Similar conclusions are also obtained by the work of Bechtle et. al. in [14] concerning the European region.

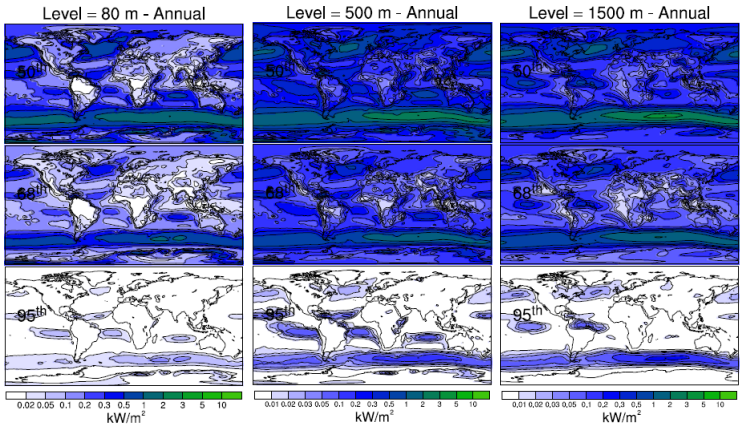


Figure 1.1: Wind resource comparison at different heights above the ground. The $50^{th}$, $68^{th}$ and $95^{th}$ percentiles of wind power density are shown. [12]

Differently from conventional HAWTs, AWESs are promising because can harvest power from these high altitude winds. Indeed, depending on the type of technology, AWES can reach hundred meters or even kilometers [2]. The novel concept of AWESs is to reach high altitude winds simulating the blade's tip of a conventional wind turbine (Figure 1.2). Indeed, it is well known that in HAWTs the generated aerodynamic power along the blade is approximately uniform. However, due to the high relative wind speed, the outer of the blades (the fastest part) have high performances in term of power production to chord length [15, 16]. The idea is to use tethered flying device to simulate the tip motion. Therefore, only the kite, the tether and a ground station are used avoiding the big nacelle and tower.

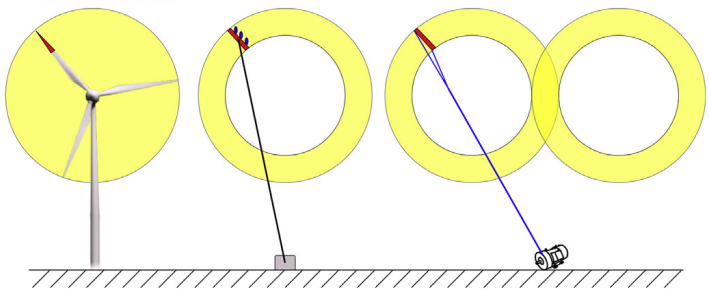

Figure 1.2: Novel concept of AWESs [16]

Several advantages are present thanks to the exploitation of high altitude winds with this concept. They have yet to be demonstrated, but the theoretical potential is great. A list of potential benefits is given below:

1. 90% less material could be used than conventional wind turbines. Indeed, the tower and its foundation are substituted by the tether and the ground station, which has smaller foundations [17]. Thanks to the crosswind motion (and so to the high relative wind speed), the airborne unit is potentially way lighter than the three blades of a HAWT of the same rated power [18].
2. Due to the potentially lower amount of material, the capital investment costs compared to a conventional HAWT could be reduced. Even the maintenance is potentially easier and cheaper because it can be done at ground level [16]. For these reasons, a lower LCOE than other energy sources is foreseen by 2030 [15, 18].
3. Due to the lower amount of material, AWESs could have a much lower environmental impact both in terms of $CO_2$ emissions and visual impact.
4. Probably higher capacity factor due to the more persistent winds [18].
5. Probably higher flexibility, easier logistic and quick set-up [15].
6. Additional interesting sites, not suitable for conventional wind machines.
7. Potential for a more constant and less intermittent production, better coupling with the grid [15, 19].
8. Suitable for remote and difficult-to-access area.
9. Very interesting for the re-powering of existing conventional off-shore and on-shore wind power plants [15].
10. New energy sources to reinforce the energy mix, creation of a new market with related new jobs and potential European leadership [10].
11. Potential for maritime transportation [15, 20].
12. Very promising in off-shore deep water configuration. The cost of the floating infrastructure in conventional wind turbines account for more than 2/3 of the total cost. AWESs appear to exert a lower oscillating force on the floating foundation and appear to be less affected by waves than conventional HAWTs. Therefore, AWESs might need a much smaller and cheaper floating infrastructure [18, 21]. In this case, about the 97% of materials could be saved [15].
13. The wind farms could be more dense compared to the conventional ones. Indeed, the problems related to the wake losses could be overcome by flying multiple kites at different altitudes [18].

Despite of the listed potentialities, AWE still have to face many challenges and open problems. Some of them are listed below:

1. Improvements from the standpoint of autonomous control must be made to increase security, reliability and operating hours of the systems.
2. Many features of AWESs have yet to be tested and demonstrated, both in an on-shore and, above all, in an off-shore environment.
3. Commercialization of AWE products and the related impact on the society still need to be understood.
4. Systems behaviour in case of extreme conditions (lightening, storm, etc...) have yet to be addressed.
5. The tether drag is another limitation for driving maximum power. Indeed, to reach high altitude winds, longer tether is needed and consequently higher power losses due to drag are present [22].

## 1.2. Technology overview

In this thesis the focus is on crosswind AWESs because many literature sources demonstrate that crosswind generation is more promising than non-crosswind [5, 18, 23].
The classification of crosswind AWESs is the way in which the power is harvested. Mainly two types of technology can be distinguished: Ground Generation Airborne Wind Energy Systems (GG-AWESs) and Fly Generation Airborne Wind Energy Systems (FG-AWESs).

GG-AWESs has the generator located in the ground station and two further subcategories exist. The first is characterized by the power production through a moving Ground Station (GS), pulled by multiple kites. Its main advantage is the ability to produce energy continuously or nearly continuously. Three main configurations are distinguished and presented in Figure 1.3: carousel [24–26], closed loop rail [27, 28] and open loop rail [17]. Since the thesis will not focus on them, for more details refer to the cited bibliography. The second type of GG-AWESs is characterized by a fixed ground station. The lift force acting on the flying kite makes the tether unwind. The tether reel-out is the cause of ground generator rotation and power production. The kinetic power of the wind is transformed into traction power which in turn becomes the kinetic power carried by the tether before finally being converted into electricity. When the tether reaches its maximum length, a reel-in (or recovery) phase starts. During this passive phase, the kite attitude is changed to minimize the energy consumption. A schematic representation of

the 'pumping cycle' is given in Figure 1.4 (a).

FG-AWESs have on-board wind turbines connected to on-board generators. The kinetic power of the wind is directly converted into electricity and then transported to the ground by the tether. In this system, the power production is generated continuously without the presence of a power cycle. A schematic representation of the functioning is given in Figure 1.4 (b).

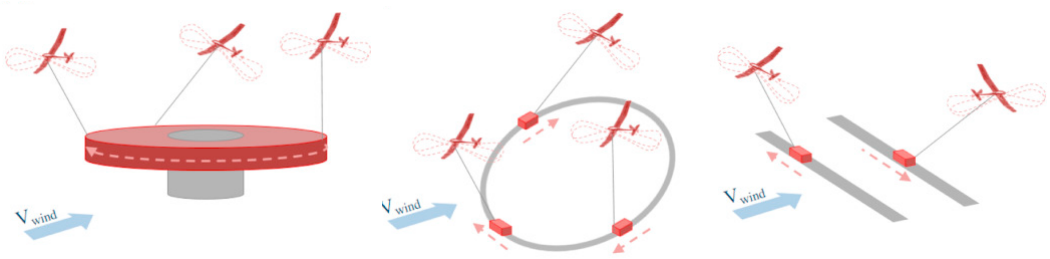


Figure 1.3: Typologies of GG-AWESs with moving ground station. From left to right: Carousel, closed loop rail, open loop rail [17]

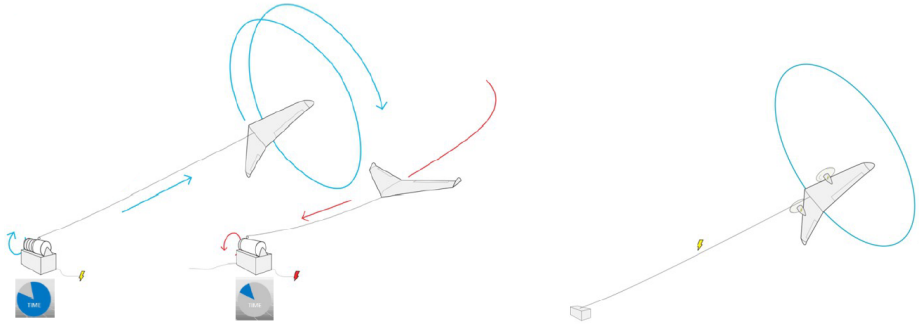

(a) *Active and passive phases of a GG-AWES*

(b) *Functioning of a FG-AWES*

Figure 1.4: Functioning of GG-AWESs (left) and FG-AWESs (right) [15]

A further classification is given by the type of flying devices. In Figure 1.5, the device typologies are present. The two categories are soft kites (a,b and c) and rigid, or hard, (d,e,g and h) kites. The firsts are cheaper and easy to repair, replace and so to test. They are lighter and the gravity has a lower influence. They are easier to take-off and land but they are harder to fly autonomously and have lower aerodynamic efficiency. On the other hand, the second are more expensive and can require sophisticated launching and landing mechanisms. They are heavier and the gravity influence is greater. However they are durable, have higher performance, and are much easier to model and control.

For the above mentioned reasons, most early-stage airborne wind developers have tested generation using soft kites. Nowadays, the industry is varied with companies that already have commercial projects using soft kites but, in the same way, the use of rigid kites also seems to be increasing [21].

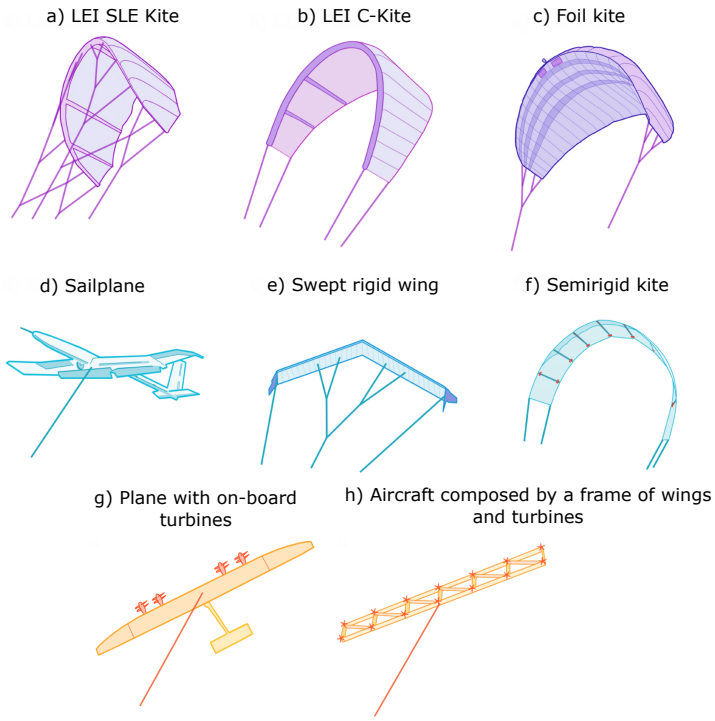


Figure 1.5: Typologies of flying devices [17]. LEI SLE stands for Leading Edge Inflatable, Supported Leading Edge

## 1.3. Current scenario and state of the art

The AWE sector is rapidly evolving and expanding. Nowadays, many institutions understand the potential of this new technology and have enhanced research activities. Figure 1.6 shows the AWE community, research and development activities across the globe in 2018.

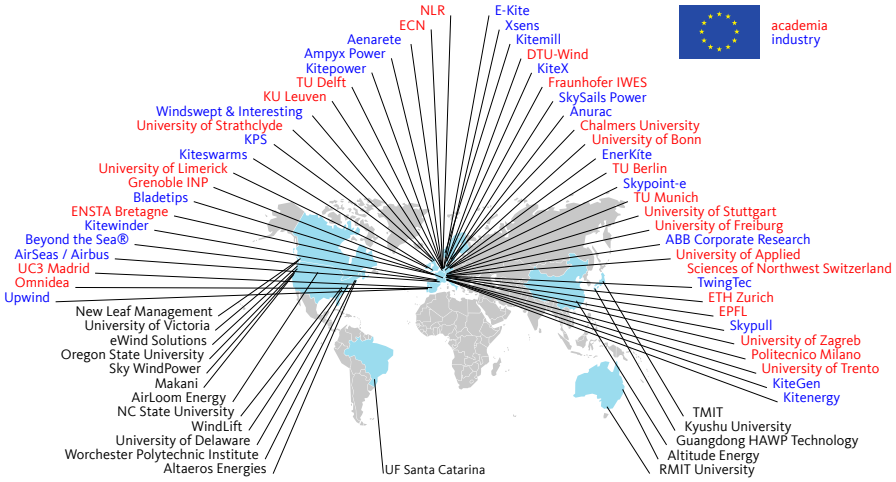


Figure 1.6: Research and development activities on AWESs across the globe in 2018 [29]

The main companies that want to enter the market with their crosswind devices are present in Figure 1.7.

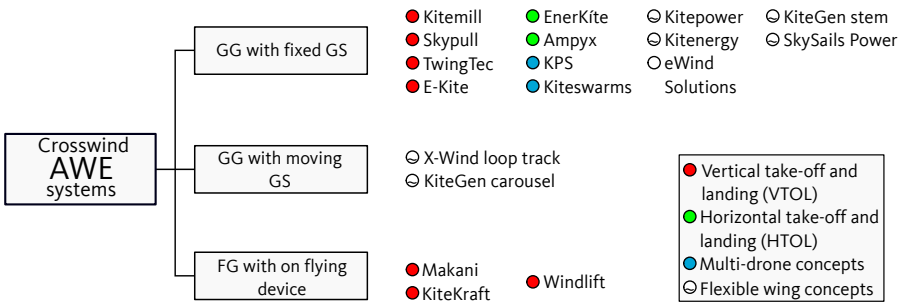


Figure 1.7: Main companies in the AWE sector that are developing crosswind AWESs

A description of the main companies divided by type of technology (Figure 1.7) is given in the following.

**GG with fixed GS** This technology is certainly the most spread among the market as visible from Figure 1.7.

The main actors flying soft kites are Kitepower and Skysails. They develope soft kites for pumping operations and successfully proved autonomous take-off, pumping cycles and landing [30, 31]. They both fly an eight-shaped path. Kitepower used a LEI kite while Skysails a foil kite. Skysails is already on the market with its 200 $kW$ kite, SKS PN-14, while Kitepower will enter the market with a 100 $kW$ kite, the Kitepower Falcon, in the fourth semester of 2022. For more information refer to [17, 20, 32].

Ampyx, Kitemill and TwingTec are the main promoters of hard kites.
Ampyx is the first company that developed a rigid kite (glider) for pumping generation. They successfully proved autonomous pumping cycles and Horizontal Take-Off and Landing (HTOL) maneuvers [33–36].AP-4 is their first commercial product with a nominal power of 2 $MW$.
Kitemill and TwingTec propose gliders with embedded propellers having rotational axis perpendicular to the wing plane used during the Vertical Take-Off and Landing (VTOL). While Ampyx flies eight-shaped paths, Kitemill and TwingTec fly circular trajectories. Kitemill is currently testing its prototypes in the range of $30 - 100$ $kW$ while Twingtec aims to develope a $MW$ scale system. For more information refer to [37–39].

Finally, Skypull developed a squared-shaped rigid drone made up of multi-element airfoils and four propellers needed for the VTOL. Skypull system flies eight-shaped paths and its SP130 reaches $1,3$ $kW$ of rated power. For further details refer to [40–42].

**GG with moving GS** The Italian company KiteGen is the first to proposed the concept of the moving-ground-station architecture with the carousel configuration. No prototypes exist yet, but studies in [26] demonstrate the potentialities of this technology. During operations, lift forces are transmitted from the kites to a rotating frame inducing a torque around the main vertical axis. This system can be seen as a vertical axis wind turbine driven by forces which come from tethered aircraft [17]. For more information refer to [43].

**FG** The main promoters of this technology are the American company Makani, the Dutch KiteKraft and the American Windlift.

Makani stopped activities in September 2020. However, the choice to insert the company in the list is driven by their cutting-edge technology representing the state of the art for crosswind FG-AWESs. Their story can be understood from the documentary on YouTube [44]. They first developed a completely autonomous glider of the $MW$ scale that generates power with eight on-board wind turbines used as motors during the transition phases. The glider flies a circular path and both the take-off and the landing are vertical (VTOL). Their last prototype, M600, had a rated power of 600 $kW$ and was tested in all conditions both on-shore and off-shore in the North Sea. Despite their efforts, M600 never reached the rated power due to design mistakes analyzed at the end of their report [6]. Makani started to design a new prototype, MX2, to meet the original intent of M600. However, it was never

completed. After the closure, Makani's team shares what they have learned on how to fly a kite during their thirteen years of activities. The material is open to access and it is summarized into three reports [6–8]. All the videos of the flight tests are present in [45] and [46]. Moreover, the code repositories is present in [47], the flight logs can be downloaded from [48] and the Makani simulation tool KiteFAST is present in [49]. For more information refer to the mentioned bibliography.

KiteKraft proposes a boxplane structure (type h in Figure 1.5) flying eight-shaped trajectories. The device is designed to maximizes rigidity while minimizing weight. As for the Makani's prototypes, eight rotors are present on the flying device used as generator during the flight and as motors during the VTOL [50]. For more information refer to the [51].

Windlift is developing a glider suitable for remote applications having four rotors and flying figure-of-eight paths. For more information refer to the [52].

**Deep Green Technology** The Swedish company Minesto is the first in the world to ever successfully developed its unique 'Deep Green Technology'. Actually, it is not part of the AWE sector because its technology exploits the marine energy. For this reason, it is not cited in Figure 1.7. However, the physics of the system is the same of a FG-AWESs. Minesto developed a tethered rigid kite that exploits underwater currents 'flying' an eight-shaped 'crosswind' path and generates power through onboard turbines. They already have two 100 $kW$ machines connected with the grid in the Faroe Islands since 2018 ([53, 54]). They are now launching the Dragon Class, a kite that can reaches 1.2 $MW$ of rated power. For more information refer to [55].

For more information about the other companies refer to the bibliography: EnerKite [19], Kiteswarms [56], Kitenergy [57], eWind Solutions [58]. Moreover, Windswept & Interesting Ltd is not present in Figure 1.7 because proposes a technology different from the others. The power is generated via a kite turbine: a ring that rotates thanks to the presence of aerodynamic profiles on it. The mechanical power is transferred to the ground generator via cables in tension and the whole system is sustained by a flying kite [59].

# 2 | Physical modelling of generic crosswind AWESs

Different models related to power generation have been proposed and used among the AWE community. There exist models for simulation purposes, which include detailed system dynamics with high complexity for simulation, optimization and control of AWESs. Examples are given in [60–63]. On the other hand, there are low-fidelity models suitable for basic fundamental knowledge, similar to the work presented in this thesis. Loyd in [5], Diehl et. al in [23] and Trevisi et. al in [64] estimate power production assuming a straight linear motion. Still in the low-fidelity model category, a better physical representation with simple analytical models is proposed by Trevisi et. al in [65] and Luchsinger in [66] which attempt to study the effects of centrifugal forces in a circular path. Then, the model proposed by Talmar in [67] introduces the effects of inertial and gravity forces to the quasi-steady model introduced by van der Vlugt in [68], making it suitable not only for soft kites. These last two models need an iterative process to obtain results but assumptions are shown to avoid the iterations and to derive analytical equations.

In this context, the chapter introduces a physical modelling of generic crosswind AWESs related to power generation. Starting from basics models introduced by Trevisi et. al. in [64, 65], the proposed model aims to improve the physical representation with particular attention to the analytical derivation of equations written in a quasi-closed form solution; all while remaining simple and fast in implementation. No iterative process will be needed.

To clarify, Figure 2.1 shows the chapter structure in a schematic way. To facilitate reading, during the chapter, reference is made to the numbers of the boxes shown in the figure.

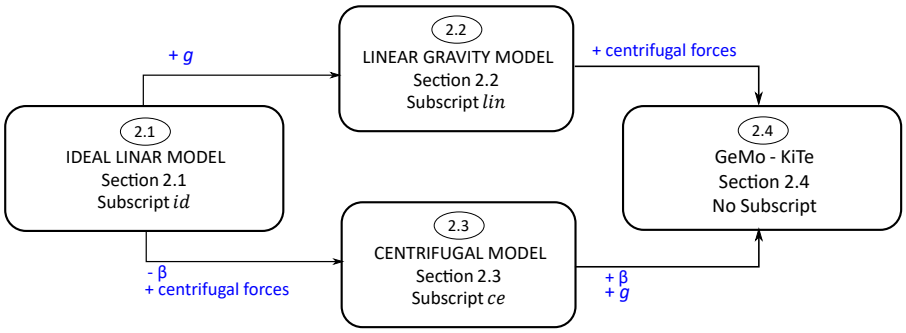


Figure 2.1: Structure of Chapter 2

Three refined models related to power production of generic AWESs from the literature are initially presented in a qualitative way.

The 'Ideal Linear Model' (box 2.1) for a generic AWES is presented in Section 2.1. This model represents both the FG-AWES and GG-AWES and it can be considered a refinement of the Loyd [5] formulation. It is based on the assumption of steady-state flight and negligible mass.

Secondly, as shown by Trevisi et al. in [64], a modelling comprehensive of the gravity force is introduced in Section 2.2. It is based on the assumption of steady-state flight and will be referred to as 'Linear Gravity Model' (box 2.2).

Then, in Section 2.3, a generic model discussing the effects of centrifugal forces is introduced from literature [65]. It is the so-called 'Centrifugal Model' (box 2.3).

Finally, in Section 2.4, a quasi-analytical model is proposed to represent the physical behaviour of a generic crosswind AWES (box 2.4). It considers together all the effects analyzed by the previous models: elevation, gravity force and centrifugal forces. The term 'generic' refers to the validity of the model for both FG-AWES and GG-AWES flying any type of trajectory. For all these reasons, it will be referred to as the Generic Model for Tethered Kites (GeMo-KiTe).

For readability, here are reported a list of subscripts used to refer to the various models cited:

- Subscript *id* refers to the 'Ideal Linear Model' with a linear motion and with no gravity.
- Subscript *lin* refers to the 'Linear gravity model' with linear motion and gravity.
- Subscript *ce* refers to the 'Centrifugal Model' with a circular motion without gravity and elevation.

- No subscript is present for the parameters related to the GeMo-KiTe involving both gravity and centrifugal forces as well as elevation.

## 2.1. Ideal Linear Model

The most elementary model is the linear flight with negligible mass presented by Trevisi et al. in [64]. This model represents a refinement of the equations presented by Loyd in [5] because it unifies equations for both fly and ground generation. This section of the chapter relates to box 2.1 in Figure 2.1. The main assumptions for the derivation are:

i. The forces acting on a wing are condensed into a single point which is a point mass representation of the kite.

ii. $E^2 >> 1$ where $E = \frac{C_L}{C_D}$ is the system glide ratio defined as the ratio between the lift coefficient $C_L$ and the drag coefficient $C_D$.

iii. The quadratic wind speed is much lower compared to the quadratic kite speed: $\frac{V_w^2}{V_k^2} << 1$, where $V_w$ is the wind velocity and $V_k$ the velocity of the kite. Actually, this hypothesis is a consequence of the previous one but it is preferred to leave them separate for greater clarity.

iv. Side forces $F_Y$ generated by the wind interaction with the tail, the pylons, the on-board wind turbines and all the other components are neglected.

v. To simplify the analysis the tether is considered inelastic without any sagging. However, a procedure to consider the latter lumped with the kite is proposed by Trevisi et al in [65].

vi. Constant wind speed during time (no turbulence) and uniform wind speed as a function of altitude.

vii. Steady-state: the external forces acting on the kite are in equilibrium, making the kite acceleration null.

viii. Gravity force neglected.

ix. Linear flight path.

Figure 2.2 represents the velocity triangles and the forces acting on the kite. The wind is blowing from left to right and the kite is flying out of the page toward the positive direction of the $y_t$-axes. In the figure, $\beta$ is the mean elevation angle, $L$ the lift force, $D$ the kite drag and $D_t$ the thrust due to the on-board turbines. The resultant aerodynamic force $R_a$ is counterbalanced by the tether traction force $T$. Moreover, $V_a$ is the relative

wind speed, $V_{out}$ is the reel-out speed and $V_\tau$ is the speed felt by the leading edge of the wing. In this case, $V_\tau$ coincides with the kite speed $V_k$.

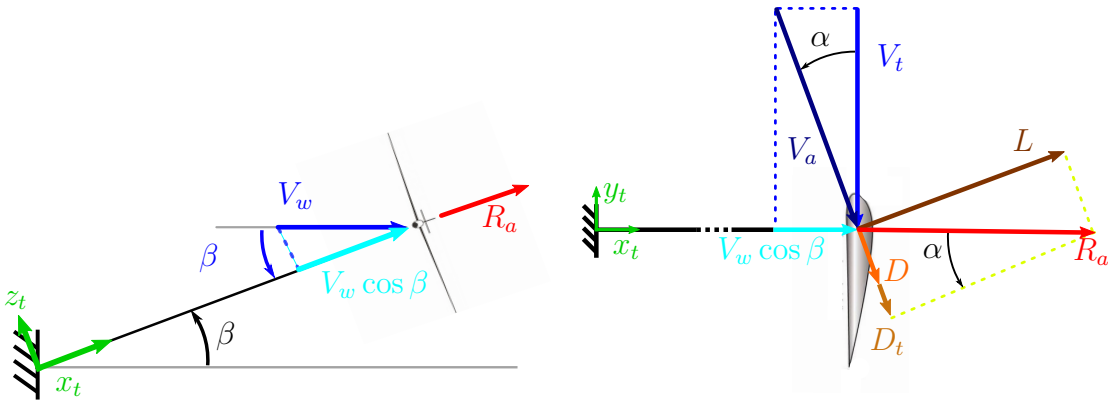


(a) *Frontal view of the system* (b) *Side view of the airfoil*

Figure 2.2: Velocity triangle and aerodynamic forces for an ideal linear path [64]

Performing the procedure, based on the velocity and force triangles in Figure 2.2, presented in [64] and reported in Appendix A.1 for completeness, it is possible to obtain the generic ideal power:

$$P_{id} = \frac{1}{2}\rho A C_D (1-\gamma_{out})^2 V_w^3 \cos\beta^3 E_t^3 \left[\gamma_t(1-\gamma_{out}) + \gamma_{out}(1+\gamma_t)\right] \tag{2.1}$$

where $\rho$ is the air density, $A$ is the area of the kite's wing, $\gamma_t = \frac{C_{D,t}}{C_D}$ is the ratio between the productive drag coefficient of the on-board turbines $C_{D,t}$ and the system drag coefficient, $E_t = \frac{E}{(1+\gamma_t)}$ and finally $\gamma_{out} = \frac{V_{out}}{V_w \cos\beta}$. Equation 2.1 is a generalization of the power equation for Ground-Gen and for Fly-Gen. In the case of FG-AWESs the power becomes $P_{id,FG} = \frac{1}{2}\rho A \gamma_t C_D V_w^3 \cos\beta^3 E_t^3$. In the following chapters, only FG-AWESs will be considered, therefore $V_w \cos\beta E_t$ will be refer to as the ideal kite speed.

## 2.2. Linear Gravity Model

The further step is to add the gravity force to the Ideal Linear Model removing assumption (viii). This section of the chapter relates to box 2.2 in Figure 2.1. With reference to Figure 2.3, the model derivation is performed by Trevisi et al. in [64] assuming small kite inclination angle $\Delta$, valid for good design. $F_g$ is the weight force.

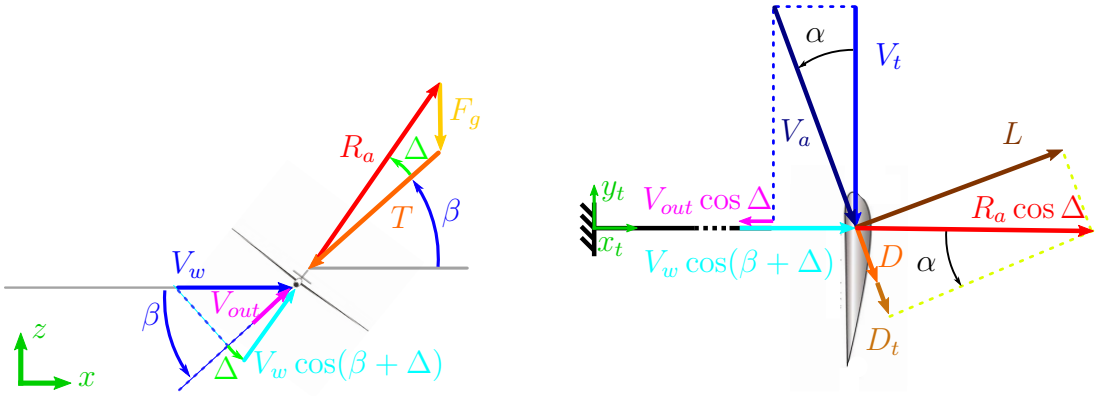


(a) *Frontal view of the system* (b) *Side view of the airfoil*

Figure 2.3: Velocity triangle and aerodynamic forces for a linear path with gravity [64]

Due to the presence of the weight force, the resultant aerodynamic force $R_a$ is inclined of an angle $\Delta$ with respect to the tether direction. In such a way, the force equilibrium is guaranteed. In this configuration, the aerodynamic effective wind speed is lower and becomes $V_w \cos(\beta + \Delta)$. Assuming the force balance along the $x$ and $z$ axes (Figure 2.3) and following the procedure in [64], for a pure FG system:

$$\Delta = \frac{mg\cos\beta}{Q^* \cos\beta^2} \qquad Q^* = \frac{1}{2}\rho A C_L V_w^2 E_t^2 \tag{2.2}$$

where $m$ is the flying mass. The methodology for the model derivation is the same used for the previous model and adopted by Trevisi et al. in [64]. For completeness, it is reported in Appendix A.2. Defining the term $\eta_\Delta = \cos\Delta - \sin\Delta\tan\beta$ ($\eta_\Delta = 1$ for $\Delta = 0°$), the generated power of a generic AWES considering the gravity force is:

$$\begin{aligned} P_{lin} = \frac{1}{2}\rho A C_D \Big[\cos(\beta+\Delta) - \gamma_{out}\cos\beta\cos\Delta\Big]^2 V_w^3 E_t^3 \cdot \\ \cdot \Big\{\gamma_t\Big[\cos(\beta+\Delta) - \gamma_{out}\cos\beta\cos\Delta\Big] + (1+\gamma_t)\gamma_{out}\eta_\Delta\cos\beta\Big\} \end{aligned} \tag{2.3}$$

The subscript *lin* refers to the linear flight considering the gravity force. The efficiency of the generic AWES accounting for the gravity presence is defined as the ratio between the power in Equation 2.3 and the ideal power in Equation 2.1:

$$\eta_{lin} = \frac{P_{lin}}{P_{id}} = \frac{\Big[\cos(\beta+\Delta) - \gamma_{out}\cos\beta\cos\Delta\Big]^2}{\cos\beta^3(1-\gamma_{out})^2} \cdot \\ \cdot \frac{\gamma_t\Big[\cos(\beta+\Delta) - \gamma_{out}\cos\beta\cos\Delta\Big] + (1+\gamma_t)\gamma_{out}\eta_\Delta\cos\beta}{\gamma_t(1-\gamma_{out}) + \gamma_{out}(1+\gamma_t)} \tag{2.4}$$

The efficiency is unitary when the kite mass is null and so is the angle $\Delta$. The power loss is present because the effective wind speed is reduced with respect to the ideal case due to the kite inclination.

## 2.3. Centrifugal Model

In this section, the step of adding centrifugal forces to the Ideal Linear Model (Section 2.1) is presented. The model has been developed by Trevisi et al. in [65] to investigate the effects of centrifugal forces on a circular trajectory. The latter is chosen because it allows for a closed-form solution, since Coriolis forces are not active [65]. The effect of centrifugal forces on a more generic trajectory will be described in Section 2.4. This section of the chapter relates to box 2.3 in Figure 2.1.

The main definitions, passages and results from [65] are here qualitatively introduced, as they will be used intensively throughout this work. Indeed, the model introduced in this thesis is built by modifying the formulation proposed by Trevisi et al [65]. For completeness, the full derivation is given in Appendix A.3. The assumptions for the modeling are those for the Ideal Linear Model without hypothesis (ix) (because of the circular path) and with the addition of:

x. Constant lift coefficient $C_L$ and drag coefficient $C_D$. Perfect and instantaneous control is assumed to maintain constant the angle of attack.

xi. Span-wise direction always perpendicular to the relative wind velocity: $\vec{s}\cdot\vec{V_a} = 0$, where $\vec{s}$ is a unit vector representing the span-wise direction towards the right wing tip.

A cylindrical reference system $(x, r, \alpha)$ is considered (Figure 2.4): the x-axis is along the direction defined by the mean elevation angle $\beta$ and the downwind direction, the radial coordinate r identifies the kite radial position in the plane perpendicular to the $x$ axis and the angular coordinate $\alpha$ is the loop angle. It starts at zero from the middle of the circular path and the kite motion is clockwise looking downwind from the ground station. The origin of the radial and axial axes is in the center of the circumference. Looking

at Figure 2.4, $x$, $r$ and $\alpha$ described the aforementioned coordinate system and $\Phi$ is the opening angle of the cone generated by the tether circular motion. Moreover, $R$ is the radius of the circular trajectory and it can be found as $R = l_t \sin\Phi$ where $l_t$ is the tether length. The plane on which the circular motion occurs is referred to as the rotor plane.

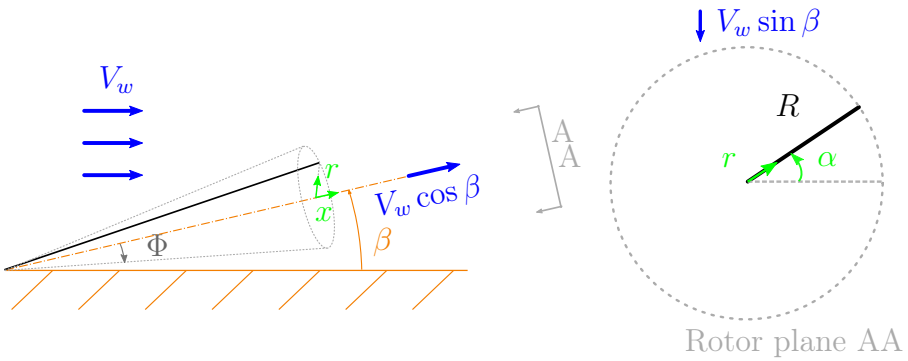


Figure 2.4: Reference system

In the aforementioned coordinate system, the kite attitude is described by the span-wise unit vector $\vec{s}$:

$$\vec{s} = \begin{pmatrix} s_x \\ s_r \\ s_\alpha \end{pmatrix} \tag{2.5}$$

where $s_x$ is the $x$-component, $s_r$ the radial component and $s_\alpha$ the tangential component. $\vec{s}$ is oriented along the wing direction with the sense always pointing the outer wing (i.e. towards the positive radial direction). In the following, $\vec{s}$ will be referred to as the span-wise vector. From $\vec{s}$, it is possible to derive two angles related to the kite attitude, important in the continuation of the thesis. The angle $\phi$ is defined as the tilt angle of the kite's wing with respect to the rotor plane. The angle $\psi$ is defined as the tilt angle of the kite's wing in the rotor plane with respect to the radial direction. To be rigorous, angles derived from a vector in space should be defined through rotation matrix. Such a methodology is discussed by Trevisi et al. in [69]. However, in this thesis, the two angles are sequentially defined starting from $\vec{s}$ as shown in Figure 2.5. The $\phi$ angle is defined as:

$$\phi = \arctan\left(\frac{s_x}{\sqrt{s_r^2 + s_\alpha^2}}\right) \tag{2.6}$$

In the following, the $\phi$ angle will be referred to as the roll angle. The angle $\psi$ is defined as:

$$\psi = \arctan\left(\frac{s_\alpha}{s_r}\right) \tag{2.7}$$

In the following, the $\psi$ angle will be referred to as the yaw angle. With such definitions, both $\phi$ and $\psi$ have the same sign of the respective components of $\vec{s}$, $s_x$ and $s_\alpha$. Moreover, both roll and yaw angles will also be called tilt angles in contexts where there is no equivocation between the them.

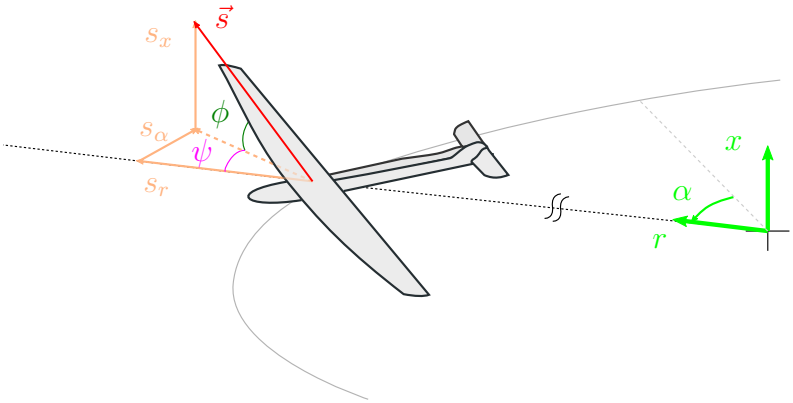


Figure 2.5: Definition of kite roll angle $\phi$ and yaw angle $\psi$

The steps for the derivation of the equations are qualitatively reported here. After having defined the relative wind speed, the lift and drag forces are found as a function of $\alpha$, $\dot{\alpha}$ and the three components of $\vec{s}$. At this point, five equations can be written: the force balances along the three axis, the unit vector definition $|\vec{s}|^2 = 1$ and, from assumption (xi), $\vec{V_a} \cdot \vec{s} = 0$. The five time dependent unknowns are $\alpha, T, s_x, s_r, s_\alpha$. By solving the system as in [65], it is possible to found the power equation of a generic AWES considering centrifugal forces:

$$P_{ce} = \frac{1}{2}\rho A C_D (\dot{\alpha} R)^3 \left[\gamma_t + (1+\gamma_t)\frac{\gamma_{out}}{1-\gamma_{out}}\right] \tag{2.8}$$

where $\gamma_{out} = \frac{V_{out}}{V_w \cos\beta}$. The efficiency $\eta_{ce}$ of a generic AWES flying a circular trajectory in case of no elevation is the ratio between $P_{ce}$ (Equation 2.8) and $P_{id}$ (Equation 2.1):

$$\eta_{ce} = \frac{P_{ce}}{P_{id}} = \cos\Phi^3 \left(M + \sqrt{1 - \frac{M^2}{\tan\Phi^2}}\right)^3 \tag{2.9}$$

where $M$ is a non-dimensional parameter defined as:

$$M = \frac{m}{\frac{1}{2}\rho A C_L l_t} \tag{2.10}$$

Except for the term $\sin\Phi$, $M$ physically represents the ratio between the centrifugal and the aerodynamic forces:

$$\frac{F_c}{L} = \frac{m\dot{\alpha}^2 R}{\frac{1}{2}\rho A C_L \dot{\alpha}^2 R^2} = \frac{m}{\frac{1}{2}\rho A C_L l_t \sin\Phi} = \frac{M}{\sin\Phi}$$

From Equation 2.9, the efficiency does not depend on the wind speed and it is function of only $\Phi$ and $M$. It is possible to analytically derive the optimal conditions by equating to zero the derivative of Equation 2.9 with respect to $\Phi$ or $M$:

$$M_{ce}^{opt} = \tan\Phi \sin\Phi \qquad \Phi_{ce}^{opt} = \arccos\left(\frac{M}{2} + \frac{\sqrt{M^2+4}}{2}\right) \tag{2.11}$$

As reported in [65], the kite is not able to fly when $\Phi < \arctan(M)$.

## 2.4. Generic Model for Tethered Kites (GeMo-KiTe)

In this section, a generic model for power generation estimation of AWESs is derived. It considers the effects of centrifugal forces in a generic trajectory together with the presence of both elevation and gravity force. This section of the chapter relates to box 2.4 in Figure 2.1.

This model is a generalization of the ones presented in Sections 2.1, 2.2 and 2.3. It is representative of both FG-AWES and GG-AWES, and, above all, it is suitable for any type of trajectory, as long as it is not too different from the circumference. This constraint will be clarified in the following.

The reference system is the same adopted in Figure 2.4, in which the kite position is individuated by the vector:

$$\vec{p} = \begin{pmatrix} x \\ r \\ \alpha \end{pmatrix} = \begin{pmatrix} \Delta x + \Delta x_{out} \\ r \\ \alpha \end{pmatrix} = \begin{pmatrix} \Delta x + V_w \cos\beta \int_0^t \gamma_{out} \cdot dt \\ r \\ \alpha \end{pmatrix} \tag{2.12}$$

where $\gamma_{out} = \frac{V_{out}}{V_w \cos\beta}$ again and $t$ is the time. The axial position has been divided into two

terms. Since a generic trajectory is three-dimensional, an axial displacement with respect to the rotor plane [1] will be present even if there is no reel-out. This axial displacement is identified by $\Delta x$. The other component of the axial position, $\Delta x_{out}$, is given by the contribution of the reel-out motion $\Delta x_{out} = V_w \cos\beta \int_0^t \gamma_{out} \cdot dt$. Figure 2.6 explains this concept for a generic trajectory. The black line is the generic trajectory for a given reel-out velocity, the orange line is the generic trajectory if the reel-out speed is null and the dashed grey line represents the rotor plane.

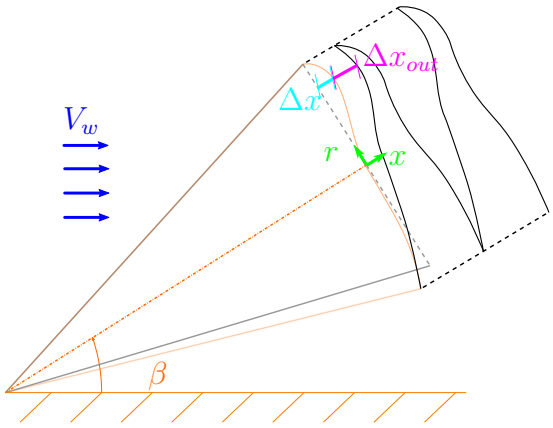


Figure 2.6: Visual explanation of how the axial position is decoupled

The kite velocity is individuated by the vector:

$$\vec{\dot{p}} = \begin{pmatrix} \dot{x} \\ \dot{r} \\ \dot{\alpha} \end{pmatrix} = \begin{pmatrix} \Delta\dot{x} + V_w \cos\beta\gamma_{out} \\ \dot{r} \\ \dot{\alpha} \end{pmatrix} \tag{2.13}$$

where $\dot{x}$, $\dot{r}$ and $\dot{\alpha}$ are the axial, radial and angular velocities of the kite. The kite acceleration is individuated by the vector:

$$\vec{\ddot{p}} = \begin{pmatrix} \ddot{x} \\ \ddot{r} \\ \ddot{\alpha} \end{pmatrix} = \begin{pmatrix} \Delta\ddot{x} + V_w \cos\beta\dot{\gamma}_{out} \\ \ddot{r} \\ \ddot{\alpha} \end{pmatrix} \tag{2.14}$$

where $\ddot{x}$, $\ddot{r}$ and $\ddot{\alpha}$ are the axial, radial and angular acceleration of the kite. The instantaneous opening angle can be found as a function of $r$:

[1] In the case of non-circular paths and so three-dimensional trajectories, rotor plane refers in any case to the plane, perpendicular to the direction identified by $\beta$, in which the circular motion would occur.

$$\Phi = \arcsin\left(\frac{r}{l_t}\right) \tag{2.15}$$

In these equations, the trajectory is left generic as a function of $r = r(\alpha)$ and $x = x(\alpha)$. Explicating these two functions a specific path can be defined. The assumptions needed for the derivation are:

i. The forces acting on a wing are condensed into a single point which is a point mass representation of the kite.

ii. Span-wise direction always perpendicular to the relative wind velocity: $\vec{s} \cdot \vec{V_a} = 0$.

iii. Side forces $F_Y$ generated by the wind interaction with the tail, the pylons, the on-board wind turbines and all the other components are neglected.

iv. Constant lift coefficient $C_L$ and drag coefficient $C_D$. Perfect and instantaneous control is assumed to maintain constant the angle of attack.

v. To simplify the analysis the tether is considered inelastic without any sagging. However, a procedure to consider the latter lumped with the kite is proposed by Trevisi et al in [65].

vi. Constant wind speed during time and uniform wind speed as a function of altitude.

vii. $E^2 >> 1$.

viii. The quadratic axial wind speed is much lower compared to the quadratic kite tangential speed: $\frac{V_w^2 \cos\beta^2}{(\dot{\alpha}r)^2} << 1$. Actually, this hypothesis is a consequence of the previous one but it is preferred to leave them separate for greater clarity.

ix. The radial kite speed is much lower compared to the kite tangential speed: $\frac{\dot{r}^2}{(\dot{\alpha}r)^2} << 1$ and $\frac{\dot{r}V_w \sin\beta}{(\dot{\alpha}r)^2} << 1$.

x. The axial kite speed is much lower compared to the kite tangential speed: $\frac{\dot{x}^2}{(\dot{\alpha}r)^2} << 1$ and $\frac{\dot{x}V_w \cos\beta}{(\dot{\alpha}r)^2} << 1$.

xi. Moreover, $\frac{\dot{x}\dot{r}}{(\dot{\alpha}r)^2} << 1$.

Hypotheses (ix), (x) and (ix) are necessary because they allow for a 'quasi-closed-form' solution. These hypotheses result in the kite's speed being mainly tangential. Consequently, the prescribed trajectory must not be too far from a circular path, otherwise a mismatch with the aforementioned assumptions is present.

The methodology and the procedure for the model derivation are similar to the one discussed in the previous model. The starting point for the derivation is the definition of

the relative wind speed, $\vec{V_a}$, in the aforementioned coordinate system:

$$\vec{V_a} = \begin{pmatrix} V_x \\ V_r \\ V_\alpha \end{pmatrix} = \begin{pmatrix} V_w \cos\beta - \dot{x} \\ -V_w \sin\beta \sin\alpha - \dot{r} \\ -V_w \sin\beta \cos\alpha - \dot{\alpha} r \end{pmatrix} \tag{2.16}$$

where $V_x$, $V_r$ and $V_\alpha$ are the relative wind speed components along the $x$, $r$ and tangential axes respectively. Defining $K_1 = 1 + \frac{V_w}{\dot{\alpha} R} sin\beta cos\alpha$, the relative wind velocity can be rewritten as:

$$\vec{V_a} = \begin{pmatrix} V_w \cos\beta - \dot{x} \\ -V_w \sin\beta \sin\alpha - \dot{r} \\ -\dot{\alpha} r K_1 \end{pmatrix} \qquad K_1 = 1 + \frac{V_w}{\dot{\alpha} R} sin\beta cos\alpha \tag{2.17}$$

With assumptions (viii), (ix), (x) and (xi), the magnitude of the relative wind speed becomes:

$$|\vec{V_a}| \approx \dot{\alpha} R K_2 \qquad K_2 = \sqrt{1 + 2\frac{V_w}{\dot{\alpha} R} \sin\beta \cos\alpha} \tag{2.18}$$

The lift force is defined as:

$$\vec{L} = \begin{pmatrix} L_x \\ L_r \\ L_\alpha \end{pmatrix} = \frac{1}{2} \rho A C_L |\vec{V_a}| \vec{V_a} \times \vec{s} = \frac{1}{2} \rho A C_L (\dot{\alpha} R) K_2 \begin{pmatrix} V_r s_\alpha - V_\alpha s_r \\ V_\alpha s_x - V_x s_\alpha \\ V_x s_r - V_r s_x \end{pmatrix} \tag{2.19}$$

where $L_x$, $L_r$ and $L_\alpha$ are the components along the axial, radial and tangential directions respectively. The drag force is defined as:

$$\vec{D} = \begin{pmatrix} D_x \\ D_r \\ D_\alpha \end{pmatrix} = \frac{1}{2} \rho A C_D (1 + \gamma_t) |\vec{V_a}| \vec{V_a} = \frac{1}{2} \rho A C_D (1 + \gamma_t) (\dot{\alpha} R) K_2 \begin{pmatrix} V_x \\ V_r \\ V_\alpha \end{pmatrix} \tag{2.20}$$

where $D_x$, $D_r$ and $D_\alpha$ are the components along the axial, radial and tangential directions respectively. With reference to Figure 2.7, the gravity force $\vec{F_g}$ is decomposed in the three following components:

$$\vec{F}_g = mg \begin{pmatrix} -\sin\beta \\ -\cos\beta\sin\alpha \\ -\cos\beta\cos\alpha \end{pmatrix} \tag{2.21}$$

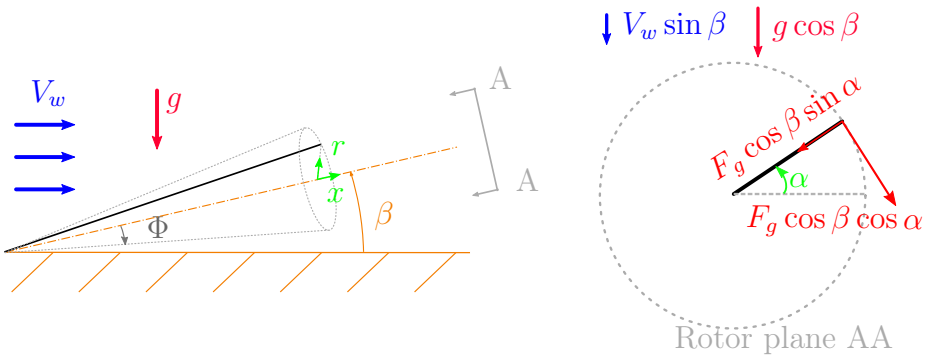


Figure 2.7: Gravitational force decomposition

With these premises, the equations underlying the model, comprehensive of the Coriolis force and the kite inertia along the three axes, are:

$$\begin{cases} r = r(\alpha) & \text{(2.22a)} \\ x = x(\alpha) & \text{(2.22b)} \\ \vec{s}\cdot\vec{V}_a = s_x V_x + s_r V_r + s_\alpha V_\alpha = 0 & \text{(2.22c)} \\ |\vec{s}|^2 = s_x^2 + s_r^2 + s_\alpha^2 = 1 & \text{(2.22d)} \\ L_x + D_x - T\cos\Phi - mg\sin\beta = m\ddot{x} & \text{(2.22e)} \\ L_r + D_r - T\sin\Phi - mg\cos\beta\sin\alpha + mr\dot{\alpha}^2 = m\ddot{r} & \text{(2.22f)} \\ L_\alpha + D_\alpha - mg\cos\beta\cos\alpha - 2m\dot{\alpha}\dot{r} = m\ddot{\alpha}r & \text{(2.22g)} \end{cases}$$

where Equations 2.22a and 2.22b represent the flight path prescription, Equation 2.22c comes from the assumption (xi), Equation 2.22d is the unit vector definition and Equations 2.22e, 2.22f and 2.22g represent the axial, radial and tangential equilibrium respectively. The problem is characterized by 7 equations in 7 time-dependent unknowns: $s_x$, $s_r$, $s_\alpha$, $\alpha$, $T$ and the two functions describing the flight path.

At this point, substituting Equation 2.17 into Equation 2.22c, the tangential component of the span-wise vector is:

$$s_\alpha = \frac{(V_w\cos\beta - \dot{x})\cdot s_x - (V_w\sin\beta\sin\alpha + \dot{r})\cdot s_r}{(\dot{\alpha}r)K_1} \tag{2.23}$$

Substituting the latter into Equation 2.22d, the axial component of the span-wise vector is:

$$s_{x_{1,2}} = \frac{(V_w \cos\beta - \dot{x})(V_w \sin\beta \sin\alpha + \dot{r})}{(\dot{\alpha}r)^2 K_1^2} s_r \pm \sqrt{1 - s_r^2} \tag{2.24}$$

Substituting Equations 2.17, 2.23, 2.24 into Equation 2.19, then, collecting $(\dot{\alpha}r)K_1$ and exploiting assumptions (viii), (ix), (x) and (xi), the lift force can be expressed as:

$$\vec{L} = \frac{1}{2}\rho A C_L (\dot{\alpha}r)^2 K_1 K_2 \begin{pmatrix} -s_x \frac{(V_w \cos\beta - \dot{x})(V_w \sin\beta \sin\alpha + \dot{r})}{(\dot{\alpha}r)^2 K_1^2} + s_r \\ -s_x + \frac{(V_w \cos\beta - \dot{x})(V_w \sin\beta \sin\alpha + \dot{r})}{(\dot{\alpha}r)^2 K_1^2} s_r \\ \frac{V_w \sin\beta \sin\alpha + \dot{r}}{(\dot{\alpha}r)K_1} s_x + \frac{V_w \cos\beta - \dot{x}}{(\dot{\alpha}r)K_1} s_r \end{pmatrix} \tag{2.25}$$

With the same procedure the drag force becomes:

$$\vec{D} = \frac{1}{2}\rho A C_D (1 + \gamma_t)(\dot{\alpha}r)^2 K_1 K_2 \begin{pmatrix} \frac{V_w \cos\beta - \dot{x}}{(\dot{\alpha}r)K_1} \\ -\frac{V_w \sin\beta \sin\alpha + \dot{r}}{(\dot{\alpha}r)K_1} \\ -1 \end{pmatrix} \tag{2.26}$$

From Equations 2.25, 2.26 and the axial equilibrium of Equation 2.22e, the tether traction force can be found:

$$\begin{aligned} T = \frac{\frac{1}{2}\rho A C_L (\dot{\alpha}r)^2 K_1 K_2}{\cos\Phi} \Bigg[ -s_x \frac{(V_w \cos\beta - \dot{x})(V_w \sin\beta \sin\alpha + \dot{r})}{(\dot{\alpha}r)^2 K_1^2} + \\ + s_r + \frac{V_w \cos\beta - \dot{x}}{E_t (\dot{\alpha}r) K_1} \Bigg] - m\ddot{x} - \frac{mg \sin\beta}{\cos\Phi} \end{aligned} \tag{2.27}$$

The radial component of $\vec{s}$, $s_r$, is derived considering the last equation, Equations 2.22f, 2.25, 2.26, exploiting assumptions (viii), (x), (ix) and (xi):

$$s_r = W \cos\Phi \sin\Phi + \cos\Phi \sqrt{1 - \cos\Phi^2 W^2} \tag{2.28}$$

where

$$W = -\frac{V_w \sin\beta \sin\alpha + (V_w \cos\beta - \dot{x}) \tan\Phi + \dot{r}}{E_t(\dot{\alpha}r)K_1} + \\ + \frac{M}{\sin\Phi K_1 K_2}\left[1 - \frac{g(\cos\beta\sin\alpha - \sin\beta\tan\Phi) + \ddot{r} - \ddot{x}\tan\Phi}{\dot{\alpha}^2 r}\right] \tag{2.29}$$

Finally, the kite tangential acceleration is found substituting Equations 2.25 and 2.26 into 2.22g. After few algebraic passages needed to explicit the dependency on $M$, it can be expressed as:

$$\ddot{\alpha} = \frac{\dot{\alpha}^2 \sin\Phi K_1 K_2}{M}\left[\frac{(V_w\cos\beta - \dot{x})s_r + (V_w \sin\beta\sin\alpha + \dot{r})s_x}{(\dot{\alpha}r)K_1} + \right. \\ \left. - \frac{1}{E_t} - M\frac{gl_t}{(\dot{\alpha}r)^2}\frac{\cos\beta\cos\alpha}{K_1K_2} - 2M\frac{\dot{\alpha}\dot{r}l_t}{(\dot{\alpha}r)^2K_1K_2}\right] \tag{2.30}$$

The instantaneous generated power of a generic crosswind AWES is the sum between the power produced by the on-board turbines, $P_{on}$, and the ground generated power $P_{gr}$:

$$P = P_{on} + P_{gr} = \vec{D}_t \cdot \vec{V}_a + \vec{T}\cos\Phi \cdot \vec{V}_{out} \tag{2.31}$$

Since it makes no physical sense to define an instantaneous efficiency, the latter is defined as averaged in time over the loop:

$$\eta = \frac{1}{T_{loop}}\int_0^{T_{loop}} \frac{\vec{D}_t \cdot \vec{V}_a + \vec{T}\cos\Phi \cdot \vec{V}_{out}}{P_{id}} \cdot dt \tag{2.32}$$

where $P_{id}$ is the ideal power of Equation 2.1. Knowing that $D_t = \frac{1}{2}\rho A \gamma_t C_D V_a^2$, for a FG-AWES $V_{out} = \gamma_{out} = 0$ and the generated instantaneous power is:

$$P_{FG} = \frac{1}{2}\rho A \gamma_t C_D (\dot{\alpha} r K_2)^3 \tag{2.33}$$

and the related efficiency is:

$$\eta_{FG} = \overline{\left(\frac{\dot{\alpha} r K_2}{V_w \cos\beta E_t}\right)^3} \tag{2.34}$$

For a GG-AWES, $\gamma_t = 0$ and the efficiency is:

$$\eta_{GG} = \frac{1}{T_{loop}} \int_0^{T_{loop}} \frac{\vec{T} \cos \Phi \cdot \vec{V}_{out}}{P_{id}} \cdot dt \tag{2.35}$$

The advantage of such a derivation is that the parameterization of the trajectory and its prescription are independent on the closure of the equations of motion. Indeed, the latter are left as a function of a generic kite position (Equation 2.12), a generic kite speed (Equation 2.13) and a generic kite acceleration (Equation 2.14). With the continuation of the thesis this concept will be clearer.

## 2.5. Model limitation

The main limitations of the physical model presented in Section 2.4 are due to the necessity of being simple and quite immediate.

Modeling the kite as a concentrated mass is very far from reality. The interaction between the fluid and the kite's body, with the tail and the other components, is not taken into account.

The assumption of no side forces leads to neglect the wind interaction with all the kite components making the model approximate if compared to reality.

Even considering $C_L$ and $C_D$ constant is a strong approximation. Indeed, perfect and instantaneous control is needed to maintain the values constant. Moreover, their values also vary with the Reynolds number which depends on the kite speed and varies during the loop.

Even the variability of the wind speed both in altitude and in time is not considered.

Furthermore, the assumptions related to the kite axial and radial speed make the model valid only for trajectories close to the circular one. If very different trajectories from the circular one (for instance the eight-shaped path) are considered, the validity of hypotheses relating the velocities ((ix), (x) and (xi)) must be verified.

Finally, many other peculiarities of the system are not taken into account. For example, no constraints are imposed on both the radius of the trajectory and the tether tension.

Despite all these simplifications, the main physics of centrifugal, elevation and gravity effects on the kite flight is considered, which is the aim of the model.

## 2.6. Summary and contributions

In this chapter, a physical model of a generic crosswind AWES which takes into account centrifugal, elevation and gravity effects is presented by steps.

Initially, in Section 2.1, a refined ideal model from the literature for the power production of a generic AWES is shown.

Then, two refined models are introduced from the literature. The first models the effect of gravity in a linear trajectory (Section 2.2). The second models the effect of centrifugal forces on a circular path (Section 2.3). In both cases, a general equation related to the power generation is presented and the related efficiency too.

Then, in Section 2.4, a model (the GeMo-KiTe) which considered all phenomena together is presented. In particular, it combines the effects of a generic trajectory with the ones of gravity and elevation.

Finally, a section dedicated to the main model limitations is presented.

The physical model proposed in this chapter can be useful to the AWES research community. Indeed, to the author's best knowledge, no model in the literature concerning centrifugal, elevation and gravity phenomena presents such a complete approach to the analytical derivation and closure of equations. A further innovation is provided by the generalization in terms of both system typology (GG-AWES or FG-AWES) and flight path. The GeMo-KiTe can be helpful for AWE researchers to study, during design exploration, the main physical effects of design parameters on system performance. Moreover, the effects of different flight paths on system performance can be investigated.

# 3 | Power generation of FG-AWESs flying circular path

In this chapter, the GeMo-KiTe is used to estimate the power generation of a FG-AWES flying circular paths. The derived model is no longer generic, indeed, it is actually a subcategory of the GeMo-KiTe. For readability, it will be referred to as the Circular Model for Fly Generation Tethered Kites (CiMo-FG-KiTe). The focus will be on the comprehension of power losses related to the main phenomena characteristic of AWESs.

To clarify, the chapter is divided into seven sections. Figure 3.1 shows the chapter's structure in a schematic way (the last two sections are not represented). To facilitate reading, during the thesis reference is made to the numbers of the boxes shown in the figure.

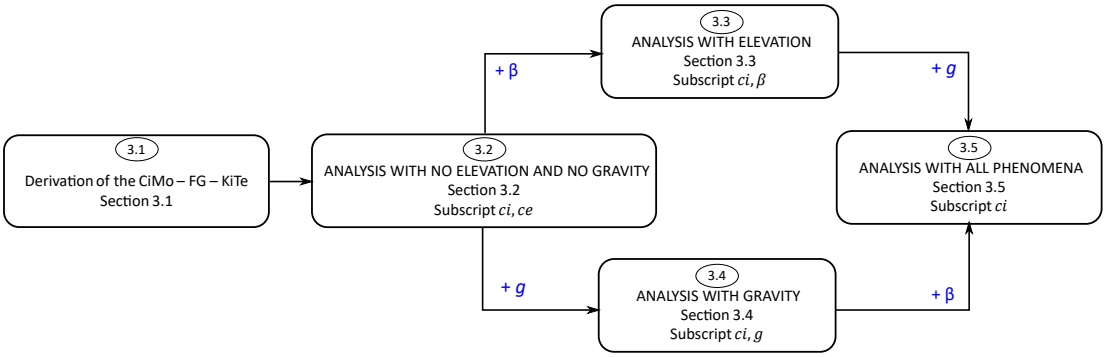


Figure 3.1: Structure of Chapter 3

Section 3.1 is dedicated to the CiMo-FG-KiTe derivation (box 3.1). Starting from the equations characteristics of the GeMo-KiTe, the circular trajectory is prescribed and the pure FG is imposed.

As for the power losses analysis, the chosen approach is to show the results of the CiMo-FG-KiTe adding each fundamental physical phenomenon one at a time. Therefore, the explanation will be made by steps. This approach is crucial to deeply understand the physical effects of each phenomenon before considering all of them together.

Therefore, in Section 3.2, only the effects of the centrifugal forces are considered. In this case, both the elevation and the gravity are not taken into account (box 3.2).

In Section 3.3, the addition of a general elevation is provided (box 3.3). Therefore, the latter together with centrifugal forces is considered.

In Section 3.4, the presence of gravity force is considered (box 3.4). Therefore, the latter is considered together with centrifugal forces.

In Section 3.5, centrifugal force, elevation and gravity are considered together (box 3.5).

In Section 3.6, numerical examples are shown to highlight the differences between the case considering centrifugal and gravity forces and the case considering all phenomena (thus, also elevation).

Finally, Section 3.7 summarizes the main findings of the chapter.

For readability, here is reported a list of additional subscripts used to refer to the various steps cited:

- Subscript $ci, ce$ refers to the results in the case of only centrifugal forces. In other words, without gravity and elevation.
- Subscript $ci, \beta$ refers to the results in the case of also elevation is taken into account without considering gravity.
- Subscript $ci, g$ refers to the results considering gravitational and centrifugal forces but no elevation.
- subscript $ci$ is present for the results that consider all phenomena together. $ci$ symbolizes the circular path.

## 3.1. Derivation of the CiMo-FG-KiTe

In this first section, the model representing a FG-AWES flying a crosswind circular trajectory is derived. This section of the chapter relates to box 3.1 in Figure 3.1.

To derive the CiMo-FG-KiTe from the GeMo-KiTe, the circular trajectory without reel-out must be prescribed:

1. Circular trajectory prescription through explicating $x(\alpha)$ and $r(\alpha)$.
2. Setting $\gamma_{out} = 0$ because in pure FG-AWES the reel-out velocity is null.

The circular path lies on the rotor plane. Therefore, no axial displacements are present at

null reel-out speed. This translates in $\Delta x = \Delta\dot{x} = \Delta\ddot{x} = 0$. Since reel-out is not present, $\Delta x_{out} = \Delta\dot{x}_{out} = \Delta\ddot{x}_{out} = 0$. Moreover, the path radius is constant as a function of $\alpha$ and can be found as: $r(\alpha) = R = l_t \sin\Phi$. Therefore, $\dot{r} = \ddot{r} = 0$.

By imposing these values in the generic equations introduced in the previous chapter (Section 2.4), it is possible to easily derive the equations in the case of FG-AWES flying circular path. In particular, only the equations related to the components of $\vec{s}$ and $\ddot{\alpha}$ are reported here because useful in the continuation of the chapter. From Equation 2.23, the tangential component of the span-wise vector becomes:

$$s_\alpha = \frac{V_w \cos\beta \cdot s_x - V_w \sin\beta \sin\alpha \cdot s_r}{(\dot{\alpha}R)K_1} \tag{3.1}$$

Then, from Equation 2.24, the axial component of the span-wise vector is:

$$s_{x_{1,2}} = \frac{V_w^2}{(\dot{\alpha}R)^2 K_1^2} \cos\beta \sin\beta \sin\alpha \cdot s_r \pm \sqrt{1 - s_r^2} \tag{3.2}$$

The radial span-wise vector component of Equation 2.28 becomes:

$$s_r = W \cos\Phi \sin\Phi + \cos\Phi\sqrt{1 - \cos\Phi^2 W^2} \tag{3.3}$$

where

$$\begin{aligned} W = &-\frac{V_w}{E_t(\dot{\alpha}R)K_1}(\sin\beta\sin\alpha + \cos\beta\tan\Phi) + \\ &+ \frac{M}{K_1K_2}\left[\frac{1}{\sin\Phi} - \frac{gl_t}{(\dot{\alpha}R)^2}(\cos\beta\sin\alpha - \sin\beta\tan\Phi)\right] \end{aligned} \tag{3.4}$$

From Equation 2.30, the kite tangential acceleration becomes:

$$\begin{aligned} \ddot{\alpha} = &\frac{\dot{\alpha}^2 \sin\Phi K_1 K_2}{M}\Big[\frac{V_w}{(\dot{\alpha}R)K_1}(s_r\cos\beta + s_x\sin\beta\sin\alpha) + \\ &- \frac{1}{E_t} - M\frac{gl_t}{(\dot{\alpha}R)^2}\frac{\cos\beta\cos\alpha}{K_1K_2}\Big] \end{aligned} \tag{3.5}$$

Moreover, the power of a FG-AWES flying a circular path is $\vec{D_{turb}} \cdot \vec{V_a}$:

$$P_{ci} = \frac{1}{2}\rho A \gamma_t C_D (\dot{\alpha}RK_2)^3 \tag{3.6}$$

and, finally, the related efficiency is:

$$\eta_{ci} = \frac{1}{T_{loop}} \int_0^{T_{loop}} \left( \frac{\dot{\alpha} R K_2}{V_w E_t \cos\beta} \right)^3 \cdot dt = \overline{\left( \frac{\dot{\alpha} R K_2}{V_w E_t \cos\beta} \right)^3} \tag{3.7}$$

In the following, the results of the model are obtained through the implementation of the equations in a time-marching code in *MATLAB*. A time step is set together with the input aerodynamic values and the initial conditions (angular position, kite speed, kite acceleration). Equations 3.4, 3.3, 3.2, 3.1 and 3.5 are implemented in this order. Then, once obtained the acceleration, time integration is simulated and the kite speed and position are derived. The obtained results are the new initial conditions for the next instant of time.

The results are extrapolated once the system reaches the quasi-steady state and the transient is over. The trends of the meaningful parameters are expressed as function of a non-dimensional time. Reminding that $R = l_t \sin\Phi$, the reference time is called $\tau$ and it is defined as:

$$\tau = \frac{2\pi l_t \sin\Phi}{V_w \cos\beta E_t} \tag{3.8}$$

The reference time physically stands for the time needed for the kite to fly a complete loop in ideal conditions (i.e. with the ideal speed $V_w E_t \cos\beta$). Therefore, $\frac{t}{\tau} > 1$ means that the average kite motion is slower than the ideal one and some power losses are present. In the following, for readability, time will be written to refer to the non-dimensional time. Moreover, to understand in which position of the loop the kite is, four vertical lines are drawn to witness the transition from the angular positions $\frac{\pi}{2}$, $\pi$, $\frac{3}{2}\pi$ and $2\pi$. An example of the results is given in Figure 3.2.

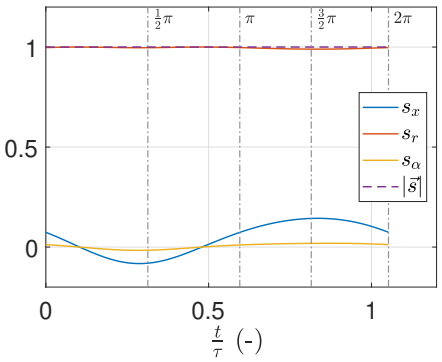


Figure 3.2: Example of results relating to the span-wise vector as a function of time

The consistency and reliability of the time-marching code is proved for various time steps: $\Delta t = 10^{-1}\ s$, $\Delta t = 10^{-2}\ s$, $\Delta t = 10^{-3}\ s$ and $\Delta t = 10^{-4}\ s$. The results converge from $\Delta t = 10^{-2}\ s$ onwards. Therefore, the latter time step is implemented for all the simulations performed. Finally, downstream the simulation, a final check on the hypothesis (viii) is done. This check informs if the model results are consistent with the initial hypothesis. If the final check shows that the assumption is not satisfied, the results are inconsistent and the hypothesis is not valid. In all the simulations carried out, the assumption has always remained valid.

## 3.2. Analysis with no Gravity and no Elevation

In this section, the physics of a FG-AWES flying a circular trajectory is presented without considering both the elevation and the gravity force. In this way the effects of centrifugal forces are isolated. This section of the chapter relates to box 3.2 in Figure 3.1.

The equations for this specific case can be easily obtained by substituting, in addition to the assumptions for the CiMo-FG-KiTe, $\beta = 0°$ and $g = 0\ m^2/s$ in the equations presented in Section 2.4.

A first subsection is devoted to the presentation of the results. Then, a second subsection is entirely devoted to the explanation of the physical phenomena associated with power losses. Finally, a numerical example is presented in the third subsection.

### 3.2.1. Results

In this section, the model results in the case of no elevation and no gravity are presented. To be as general as possible, they are shown as function of non-dimensional parameters.

Figure 3.3 shows the efficiency $\eta_{ci,ce}$ of a pure crosswind FG-AWES considering the circular trajectory varying both $M$ and $\Phi$. These results are the same obtained by Trevisi et al. in [65] with the model presented in Section 2.3 where the tangential acceleration was imposed null. Therefore, efficiency does not vary with time and can be analytically calculated as in Equation 2.9. The red-dashed line represents the optimal opening angle trend for which the efficiency is unitary. Again, this trend is the same found analytically by Trevisi et al. and reported in Equation 2.11. In the following, reference will be made to these optimal values which from now on will be identified with subscript $ci, ce$: $\Phi^{opt}_{ci,ce}$ and $M^{opt}_{ci,ce}$.
On the contrary, the blue region of the diagram represents the condition for which the kite is not able to fly. It analytically occurs when $\Phi < \arctan(M)$. In the following, it will be referred to as the no-fly zone.

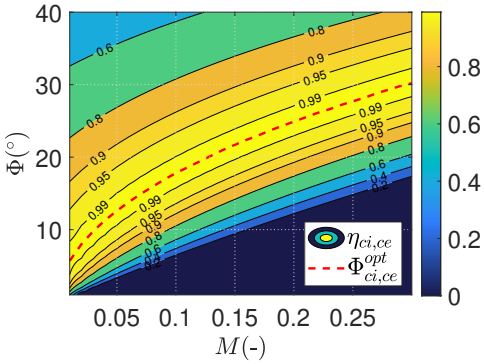


Figure 3.3: Efficiency $\eta_{ci,ce}$ as a function of M and $\Phi$

### 3.2.2. Power losses explanation

The aim of this section is to explain why for each value of $M$, it is possible to have an optimal configuration with the best performance and what are the causes of power losses.

The efficiency $\eta_{ci,ce}$ is lower than the unit when the radial component of the tether traction does not balance the centrifugal force. Indeed, the kite tilts in order to provide a radial component of the resultant aerodynamic force which ensures the radial equilibrium.

The concept is explained for a fixed $M$ through Figures 3.4, 3.5 and 3.6. $T_r$ and $T_x$ are the tether traction components, $F_c$ is the centrifugal force, $R_{a,x}$ and $R_{a,r}$ are the axial and radial components of the aerodynamic resultant force. The representations in semi-transparent colours are related to the optimal kite attitude. Again, the symbol $\phi$ stands for the roll angle, i.e. the kite tilt (or inclination) angle with respect to the rotor plane.

Figure 3.4 shows the optimal case. The optimal opening angle is the value that guarantees radial equilibrium without involving the aerodynamic force. The kite is perfectly cross-wind and the effective wind speed is the highest possible. This numerically translates in $\eta_{ci,ce} = 1$, $s_x = s_\alpha = 0$ and $s_r = 1$. Such a condition is represented by the red-dashed line in Figure 3.3 and by Equation 2.11.

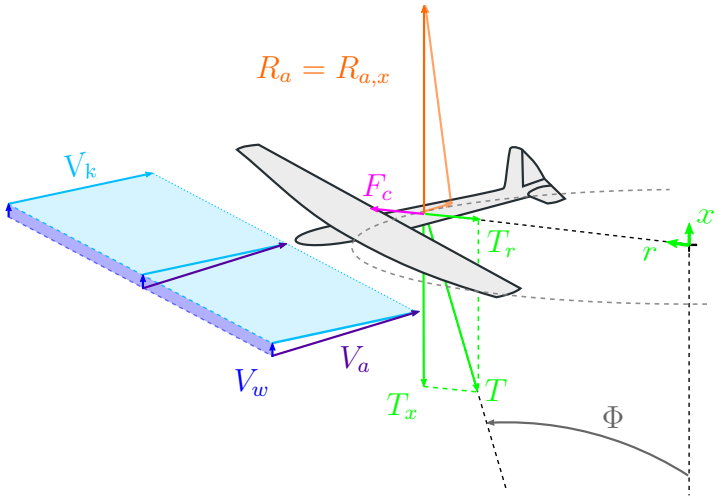


Figure 3.4: Velocity triangle, forces and kite attitude for $\Phi_{ci,ce} = \Phi_{ci,ce}^{opt}$

If the path radius (i.e. the $\Phi$ angle for a given tether length; $R = l_t \sin\Phi$) is lower than the optimum, the kite attitude is described by Figure 3.5. The lower the opening angle, the greater the centrifugal force and the lower the radial tether traction. As a result, the kite tilts towards the inside of the loop to ensure equilibrium. Thus, the aerodynamic resultant has a negative radial component that, together with the radial tether traction, balances the centrifugal force. Due to the roll angle, the effective wind speed is lower than the one in the optimal case of a factor $\cos\phi$. Consequently, the kite motion is slower and the power generation reduces.

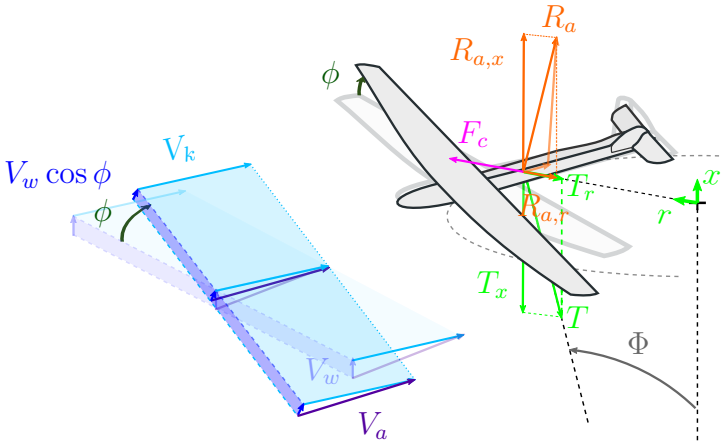


Figure 3.5: Velocity triangle, forces and kite attitude for $\Phi_{ci,ce} < \Phi_{ci,ce}^{opt}$

On the contrary, Figure 3.6 shows the opposite case with the same consequences. If the path radius is too high, the centrifugal force is lower and the radial tether traction becomes higher. The two mentioned forces do not to balance each other. Therefore, the

kite tilts outwards to provide a radial aerodynamic component $R_{a,r}$ that ensures the radial equilibrium.

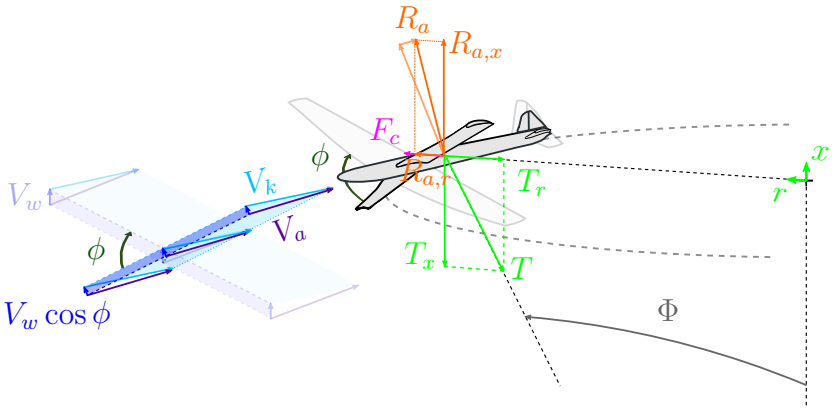


Figure 3.6: Velocity triangle, forces and kite attitude for $\Phi_{ci,ce} > \Phi^{opt}_{ci,ce}$

### 3.2.3. Numerical example

In this section, a numerical example is presented to understand the influence of the opening angle on both power losses and kite attitude. The input parameters for the example are present in Table 3.1 and they are taken from the OktoberKite Makani prototype [6].

| Variable | Value | Units | Variable | Value | Units |
|---|---|---|---|---|---|
| $E$ | 10 | - | $C_L$ | 1.5 | - |
| $A$ | 50 | $m^2$ | $l_t$ | 300 | $m$ |
| $\gamma_t$ | 0.5 | - | $\beta$ | 0 | $^\circ$ |
| $V_w$ | 10 | $m/s$ | $m$ | 1850 | $kg$ |

Table 3.1: Input parameters for the CiMo-FG-KiTe considering only centrifugal forces

With these input parameters, from Equation 2.10, $M = 0.13$ and, from Equation 2.11 $\Phi^{opt}_{ci,ce} = 20.8°$. Table 3.2 shows the results of the model for the span-wise vector $\vec{s}$ and the efficiency in case of $\Phi < \Phi^{opt}_{ci,ce}$, $\Phi = \Phi^{opt}_{ci,ce}$ and $\Phi > \Phi^{opt}_{ci,ce}$. In case of $\Phi < \Phi^{opt}_{ci,ce}$, the $x$-component of the span-wise vector is positive, meaning that the kite is tilted as in Figure 3.5. In case of $\Phi > \Phi^{opt}_{ci,ce}$, the $x$-component of the span-wise is negative, meaning that the kite is tilted as in Figure 3.6. On the contrary, in case of optimal opening angle the $x$-component of the span-wise vector is null because the kite is not tilted and it is perfectly crosswind as in figures 3.4.

| Parameters | $\Phi = 0.8 \cdot \Phi_{ci,ce}^{opt}$ | $\Phi = \Phi_{ci,ce}^{opt}$ | $\Phi = 1.2 \cdot \Phi_{ci,ce}^{opt}$ |
|---|---|---|---|
| $s_x$ (-) | 0.17 | 0 | $-0.15$ |
| $s_r$ (-) | 0.98 | 1 | 0.99 |
| $s_\alpha$ (-) | 0.02 | 0 | $-0.02$ |
| $\eta_{ci,ce}$ (%) | 95.7 | 100 | 96.6 |

Table 3.2: Results of the CiMo-FG-KiTe considering only centrifugal forces in case of $\Phi < \Phi_{ci,ce}^{opt}$, $\Phi = \Phi_{ci,ce}^{opt}$ and $\Phi > \Phi_{ci,ce}^{opt}$

## 3.3. Analysis with Elevation and no Gravity

In this section, the effects of the elevation angle $\beta$ are added to the ones of centrifugal forces. Therefore, a generalization of the previous analyses for an elevation angle $\beta \neq 0$ is described. This section of the chapter relates to box 3.3 in Figure 3.1.

The equations for this specific case can be easily obtained by substituting, in addition to the assumptions for the CiMo-FG-KiTe, $g = 0\ m^2/s$ in the equations presented in Section 2.4.

A first subsection is devoted to the presentation of the results. Then, a second subsection is entirely devoted to the explanation of the physical phenomena associated with power losses. Finally, in the third subsection, a numerical example with a high elevation angle is provided to highlight its effects.

Given the definition of efficiency in Equation 3.7, the power losses by elevation do not take into account the typical cosine losses $\cos\beta^3$ because they are already incorporated in the denominator. Therefore, in this thesis, the power losses due to elevation will only refer to the effects of the elevation angle on the kite motion.

As presented in the following, this kind of loss alone is definitely negligible in numerical terms. However, its explanation is essential to better comprehend the physics of the system when all the phenomena will be considered together. Indeed, it will be demonstrated that, once gravity is added, the contribution of power losses due to elevation becomes high and not negligible anymore.

### 3.3.1. Results

The input values for the simulations are chosen from the state of the art OktoberKite Makani prototype [6] and are present in Table 3.3. The elevation angle is made vary up to 40°; higher values are meaningless in real applications.

| Variable | Value | Units | Variable | Value | Units |
|---|---|---|---|---|---|
| $E$ | 10 | - | $C_L$ | 1.5 | - |
| $A$ | 50 | $m^2$ | $l_t$ | 300 | $m$ |
| $\gamma_t$ | 0.5 | - | $\Phi$ | $\Phi^{opt}_{ci,\beta}$ | $\circ$ |
| $V_w$ | 10 | $m/s$ | $m$ | 1850 | $kg$ |

Table 3.3: Input parameters for the generic results if centrifugal forces and elevation are considered

Figure 3.7 shows the efficiency $\eta_{ci,\beta}$ as a function of the mean elevation angle $\beta$. Higher is $\beta$, higher is its influence on the kite motion and the system performance. However, as previously anticipated, power losses remain always quite limited, in terms of $1 \div 2$ % at max. In engineering terms, it does not seem to be worth mentioning, but understanding the reason behind such power losses is critically important for the subsequent results.

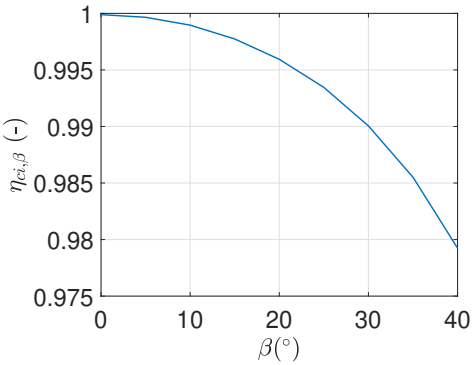


Figure 3.7: Efficiency $\eta_{ci,\beta}$ as a function of the mean elevation angle $\beta$

### 3.3.2. Power losses explanation

In this section, the causes of the power losses due to elevation are explained. For the explanation of the power losses, reference is made to the optimal trajectory in the case only centrifugal force is considered (unitary efficiency). Consequently, all comparatives present in the text refer to this case with $\Phi^{opt}_{ci,ce}$.

A subsection is devoted to each of the phenomena that affect efficiency. Then, a final summary subsection is presented. To help the comprehension, Figure 3.8 shows the phenomena associated to the power losses in a schematic way. During the description, references will be made to the numbers of the boxes shown in Figure 3.8.

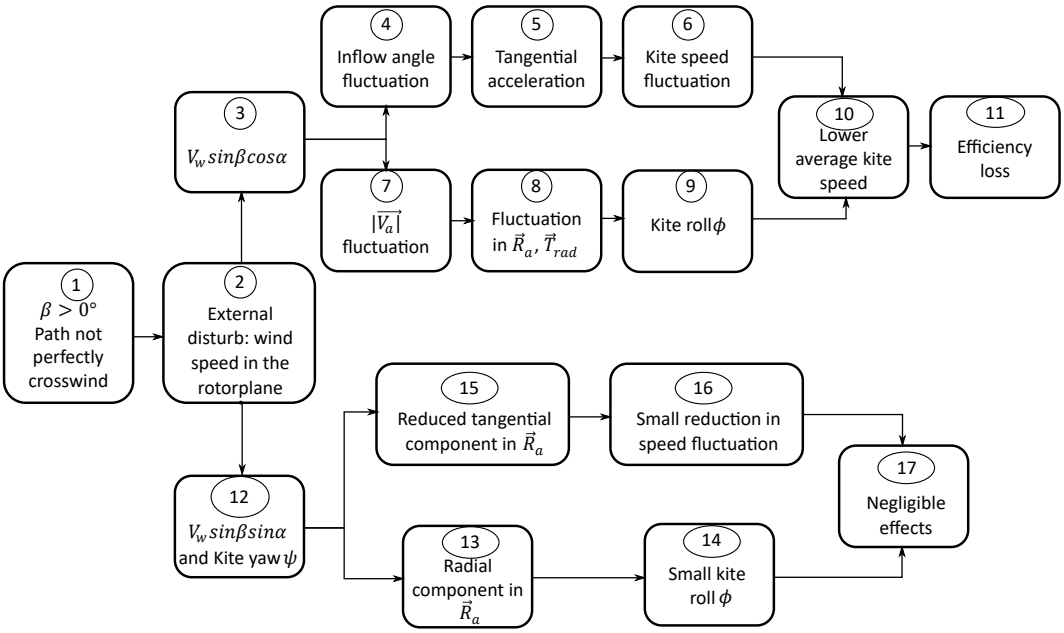


Figure 3.8: Conceptual diagram representing the physical phenomenon related to power losses due to elevation

The decrease in efficiency is due to three factors: the roll angle $\phi$, the yaw angle $\psi$ and the kite speed fluctuation during the loop. They have all the same consequence (decrease in efficiency) and the same physical cause which consist of a path not perfectly crosswind anymore (box 1). Indeed, the presence of the wind velocity in the rotor plane influence the system (box 2). When the kite is going up, the motion is slightly upwind, while when the aircraft is flying downward the motion is slightly downwind.

## Power losses due to kite speed variation

Starting from the velocity fluctuation in the loop, Figures 3.9 and 3.10 schematically explain the phenomenon through the velocity and force triangles. The figures are a sketch of the forces on the profile at $\alpha = 0°$ (Figure 3.9) and $\alpha = 180°$ (Figure 3.10). $R_{a,tan}$ represents the tangential component of the resultant aerodynamic force. In these angular positions, the kite has approximately the same velocity which is about the ideal value $V_w E_t \cos\beta$. What affects the kite speed is the tangential component of the wind speed in the rotor plane $V_w \sin\beta \cos\alpha$ (box 3).

Figure 3.9 shows the phenomenon during the ascending part of the loop for $\alpha = 0°$. $V_w \sin\beta \cos\alpha$ is added to the kite speed because the kite is flying slightly upwind. The relative wind speed becomes higher and the inflow angle lower (box 4). As a result, the resultant aerodynamic force is more rotated towards the rear of the airfoil. The

acceleration is in the opposite direction with respect to the motion (box 5). Such behaviour of the kite remains true for all the ascending phase because the kite is flying upwind.

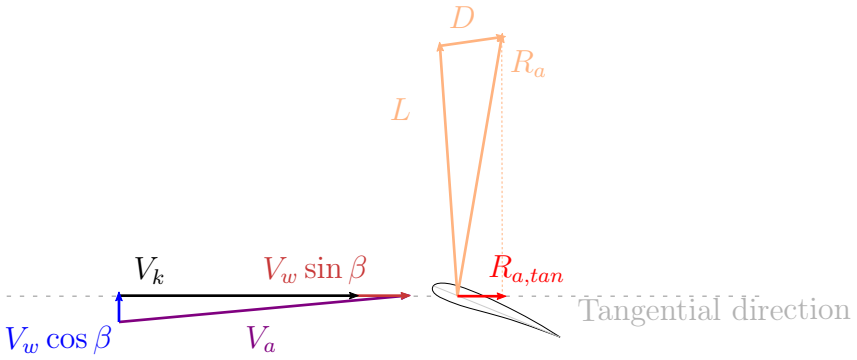


Figure 3.9: Velocity triangle and forces when the kite is flying upwind during the ascending phase. Sketch for $\alpha = 0°$

On the contrary, Figure 3.10 shows the physical phenomenon during the descending phase for $\alpha = 180°$. The wind speed component $V_w \sin\beta \cos\alpha$ subtracts from the kite velocity because the kite is flying slightly downwind. Therefore, the inflow angle is higher (box 4) and the $\vec{R_a}$ is more rotated towards the front of the airfoil providing a positive tangential acceleration (box 5). Moreover, due to the lower $|\vec{V_a}|$, the magnitude of the resultant aerodynamic force $R_a$ is lower with respect to the ascending phase. Such behaviour of the kite remains true during all the descending phase because the kite is flying downwind.

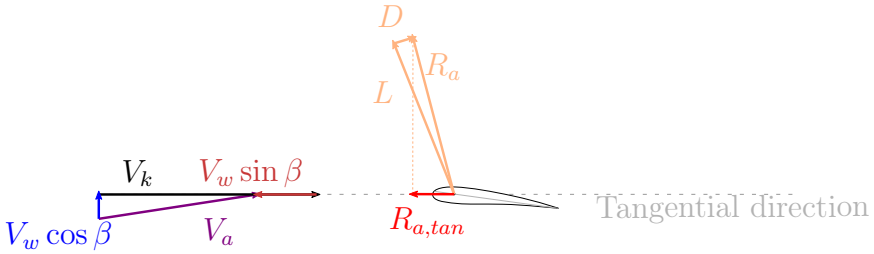


Figure 3.10: Velocity triangle and forces when the kite is flying downwind during the descending phase. Sketch for $\alpha = 180°$ [1]

The kite velocity reaches its minimum after the ascending phase at the top of the loop and its maximum at the bottom of the loop after the descending part (box 6). The related speed fluctuation makes the slower portion of the loop (upper half) more influential, once integrated in time. Therefore, the average kite velocity is lower than the ideal $V_w E_t \cos\beta$ (box 10).

[1]The pitch angle of the profile is changed from Figure 3.9 to Figure 3.10. Since the inflow angle becomes higher, the pitch angle must decrease to maintain the angle of attack constant in accordance to assumption (x).

If the mean elevation is negative, the opposite happens: the glider accelerates during the ascending motion and decelerate during the descending one. As a result, the upper part of the loop is the fastest while the bottom is the slowest. Actually, a negative mean elevation is not feasible in real system, however it will be important to understand the physics explained in the next chapters.

## Power losses due to kite roll angle $\phi$

As already mentioned, the second factor affecting power losses is the kite roll angle $\phi$. What affects, in turn, the roll angle is again the tangential component of the wind speed in the rotor plane $V_w \sin\beta \cos\alpha$ (box 3). The kite attitude and roll angle during the loop in the case of $\Phi_{ci,ce}^{opt}$ are shown in Figure 3.11. The symbol $R_{a,x\text{-}r}$ describes the projection of the aerodynamic force in the $x$-$r$ plane.

Figure 3.11 (a) shows the kite attitude in the top ($\alpha = 90°$) and bottom ($\alpha = 270°$) parts of the loop in the case of $\Phi_{ci,ce}^{opt}$. The kite on top is flying towards the observer exiting the page while the bottom kite is entering the page. For such positions in the loop, the kite is not tilted because the disturbance due to the wind speed component $V_w \sin\beta \cos\alpha$ is not present. Due to the slower motion in the top part of the loop, the forces acting on the kite are lower compared with the bottom.

The kite attitude during the ascending and descending phases are shown in Figure 3.11 (b) in the case of $\Phi_{ci,ce}^{opt}$. The kite on left is flying towards the observer exiting the page while the kite on the right is entering the page. The value of the loop angle in these positions is 0° and 180°, respectively. As already mentioned, the kite velocity is approximately the same in these parts of the loop and so is the centrifugal force. However, the wind velocity component $V_w \sin\beta \cos\alpha$ makes the kite attitude opposite in the two flying phases.
During the ascending motion, the term $V_w \sin\beta \cos\alpha$ makes the magnitude of the relative velocity higher (see Figure 3.9) (box 7). The resultant aerodynamic force is higher and, to make the $x$-balance null, the tether traction too (box 8). The higher radial component of the tether traction makes the kite tilting outwards. In this way, the resultant aerodynamic force has a radial component that, together with the centrifugal force and the radial tether traction, guarantees the radial balance (box 9).
During the descending motion, the kite attitude is the opposite, being tilted towards the inside of the loop. $V_w \sin\beta \cos\alpha$ makes the magnitude of the relative wind speed lower and so are the aerodynamic forces. The tether traction is lower too (box 8) and the kite needs to tilt to counterbalance the centrifugal force (box 9).

Again, the kite roll angle translates in a lower effective wind speed. Therefore, the kite flies

slower (box 10) and the harvested power is lower (i.e. efficiency loss - box 11). Moreover, as shown in Figure 3.11 (b), the descending part of the loop is more impactful than the ascending part in terms of power losses due to the roll angle $\phi$.

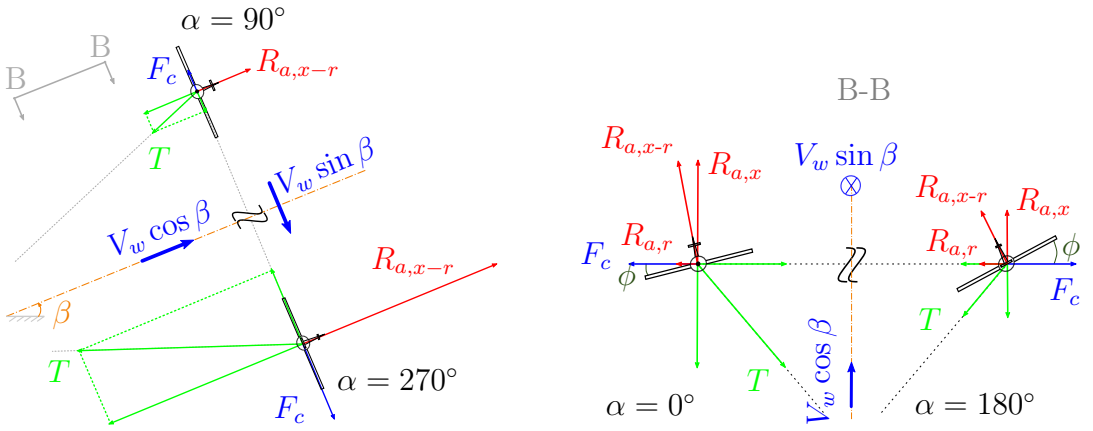


(a) *Side view of the system: kite attitude in the top ($\alpha = 90°$) and bottom ($\alpha = 270°$) parts of the loop*

(b) *Top view of the system: kite attitude in the lateral parts of the loop during the ascending (left kite, $\alpha = 0°$) and descending (right kite, $\alpha = 180°$) phases*

Figure 3.11: Kite attitude during the loop considering centrifugal forces and a generic elevation angle $\beta$ in the case of $\Phi_{ci,ce}^{opt}$

If the mean elevation is negative, the opposite happens: the kite is tilted outwards during the descending motion and towards the inner during the ascending one. Moreover, the ascending motion is more influential due to the higher roll angle. Actually, a negative mean elevation is not feasible in real system, however it will be important to understand the physics explained in the next chapters.

## Power losses due to yaw angle $\psi$

The third factor affecting power losses is the yaw angle $\psi$. Its oscillation during the loop is provided by the presence of the wind speed component $V_w \sin\beta \sin\alpha$ (box 12). However, the latter is much smaller than the kite speed and so $\psi$ is small too.
$\psi$ makes the relative wind speed and the resultant aerodynamic force no longer lie on the tangential plane. The radial component of $R_a$ affects the radial balance and makes the kite roll (boxes 13 and 14). However, depending on the sine of $\psi$ and being $\psi$ small, its influence on power losses due to roll angle can be neglected (box 17). On the other hand, the tangential component of $R_a$ is reduced by the presence of $\psi$ and so also the related speed fluctuation is lower (boxes 15 and 16). However, this reduction depends on the

cosine of $\psi$ and, being $\psi$ small, its influence on power losses due to speed variation can be neglected (boxes 17).

### Conclusions

Despite sharing the same origin (upwind and downwind motion - box 1 and 2) and having the same consequence (slower kite motion - box 10), three effects can be distinguished:

1. The kite roll angle different from zero provides a lower effective wind speed (box 9).
2. The kite yaw angle different from zero affects both the kite roll (box 14) and the speed fluctuation (box 16). However, these effects can be neglected (box 17).
3. The kite acceleration provides a velocity fluctuation which makes the slower part of the loop more influential (box 6).

The optimal opening angle will be the result of a trade-off. Higher is the opening angle, lower are both the centrifugal force and the roll angle in the descending phase (see Figure 3.11 (b)). Therefore, the more impactful descending motion is less influential in terms of power losses due to the roll angle. On the contrary, higher is the opening angle, longer is the flight path and greater is the speed variation. Consequently, the slower top part of the loop is even more influential in terms of power losses due to speed variation.
If only elevation is considered, these two effects balance each other and the optimal opening angle $\Phi_{ci,\beta}^{opt}$ remains extremely similar to $\Phi_{ci,ce}^{opt}$ (Equation 2.11).

## 3.3.3. Numerical example

In this section, the effects of the elevation angle are described numerically. Firstly, the efficiency as a function of $M$ and $\Phi$ is shown. Secondly, the results as a function of time, keeping the optimal opening angle $\Phi_{ci,\beta}^{opt}$ for the calculated $M$, are shown. The input values for the simulation are taken from the Makani's OktoberKite prototype [6] and are listed in Table 3.4. The elevation angle is set at a high value ($\beta = 40°$) to highlight the effects.

| Variable | Value | Units | Variable | Value | Units |
|---|---|---|---|---|---|
| $E$ | 10 | - | $C_L$ | 1.5 | - |
| $V_w$ | 10 | $m/s$ | $l_t$ | 300 | $m$ |
| $\gamma_t$ | 0.5 | - | $\beta$ | 40 | $°$ |
| $A$ | 50 | $m^2$ | $m$ | 1850 | $kg$ |

Table 3.4: Input parameters for the example considering centrifugal forces and elevation

With the input of Table 3.4 and from Equation 2.10, $M = 0.13$.
Figure 3.12 shows the efficiency $\eta_{ci,\beta}$ as a function of both $M$ and $\Phi$. The red-dashed line represents the trend of the optimal opening angle $\Phi^{opt}_{ci,\beta}$ for which the unitary efficiency is never reached. $\Phi^{opt}_{ci,\beta}$ is not derived analytically from equation 2.11 but it is obtained numerically by varying $\Phi$ in the time-marching code. Comparing Figure 3.12 with Figure 3.3, the differences are very limited demonstrating again that the power losses are definitely limited, if elevation is considered alone.

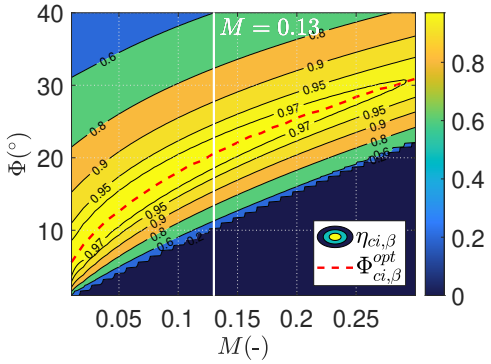


Figure 3.12: Efficiency $\eta_{ci,\beta}$ as a function of $\Phi$ and $M$ with $\beta = 40°$

With these input values, the maximum efficiency is $\eta^{max}_{ci,\beta} = 98\%$.
Figure 3.13 shows the outcome of the simulation for the kite attitude as a function of time with $\Phi = \Phi^{opt}_{ci,\beta}$. $s_x$ and $s_\alpha$ oscillate during the loop because of the presence of $V_w \sin\beta\cos\alpha$ and $V_w \sin\beta\sin\alpha$ respectively. The trend of the roll angle is the same of $s_x$, in particular its maximum value is 6.5° at $\alpha = 178°$ and its minimum is $-4.9°$ for $\alpha = 4°$. The power losses due to the roll angle are more affected by the descending motion.

Figure 3.14 shows the kite speed as function of time with $\Phi = \Phi^{opt}_{ci,\beta}$. The portion in time in which the kite velocity (blue line) is lower than the ideal speed $V_w E_t \cos\beta$ (black-dashed line) is larger causing an average kite speed (red-dashed line) lower than the ideal one.

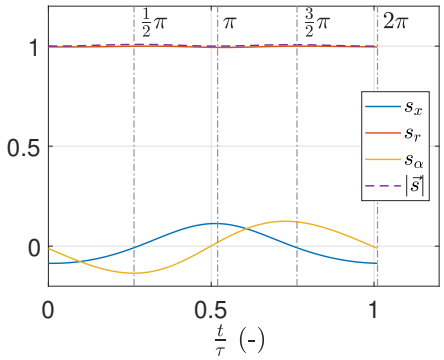


Figure 3.13: Components of $\vec{s}$ as a function of time during the loop in the case of $\Phi = \Phi^{opt}_{ci,\beta}$

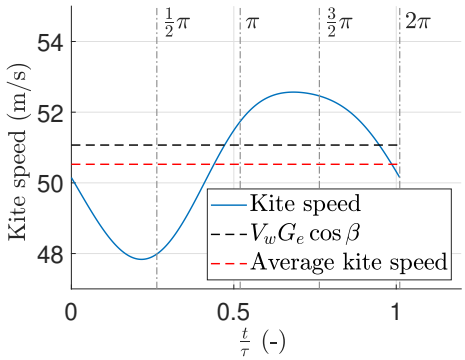


Figure 3.14: Kite speed as a function of time during the loop in the case of $\Phi = \Phi^{opt}_{ci,\beta}$

## 3.4. Analysis with Gravity and no Elevation

In this section, the physics of a FG-AWES flying a circular trajectory is presented considering gravity and with a null elevation. In this way, the effects of the gravitational acceleration is isolated. This section of the chapter relates to box 3.4 in Figure 3.1.

The equations for this specific case can be easily obtained by substituting, in addition to the assumptions for the CiMo-FG-KiTe, $\beta = 0°$ in the equations presented in Section 2.4.

In the first subsection, the results are shown after having defined a new non-dimensional parameter related to gravity. Then, a second subsection is entirely devoted to the explanation of the physical phenomena associated with power losses.

### 3.4.1. Results

To generalize the problem, the results are shown as a function of non-dimensional parameters. For this purpose, since the centrifugal effects are already represented by the non-dimensional parameter $M$, it is of fundamental importance to obtain another parameter that represents the gravitational effects. Therefore, before introducing the results of the model, a new non-dimensional parameter related to gravity is defined.

Equations 3.4 and 3.5 are derived from the radial and tangential force balances respectively. In both cases, the only term affected by gravity is the last and it includes the non-dimensional ratio $\frac{gl_t}{(\dot{\alpha}R)^2}$. Referring to the highlighted ratio, the so-called Gravity Ratio, $Gr$, is defined:

$$G_r = \frac{gl_t}{(V_w \cos\beta \; E_t)^2} \tag{3.9}$$

The denominator is an ideal estimation of the quadratic real kite speed $(\dot{\alpha}R)^2$. The choice of the ideal speed $V_w E_t \cos\alpha$ permits to evaluate $G_r$ in a conceptual design phase without performing any simulation. The physical meaning can be interpreted in two ways:

1. The ratio between the potential energy variation in the loop and the ideal kinetic energy of the kite:

$$\frac{\Delta E_p}{E_{k,id}} = \frac{2mgl_t \sin\Phi}{\frac{m(V_w \cos\beta E_t)^2}{2}} = 4\frac{gl_t}{(V_w \cos\beta E_t)^2}\sin\Phi = 4G_r \sin\Phi \tag{3.10}$$

2. The ratio between the gravity force and the ideal centrifugal force:

$$\frac{F_g}{F_{c,id}} = \frac{mg}{m\frac{(V_w \cos\beta E_t)^2}{l_t \sin\Phi}} = \frac{gl_t}{(V_w \cos\beta E_t)^2}\sin\Phi = G_r \sin\Phi \tag{3.11}$$

In both the physical interpretation, the term $\sin\Phi$ appears. In the definition 3.9, its omission is due to the desire to make $G_r$ independent of $\Phi$.

Together with $M$, $G_r$ provides an estimation of how much the presence of gravity affects the performance of the system. Indeed, the product between them physically represents the ratio between the gravity and the ideal aerodynamic force:

$$M \cdot G_r = \frac{m}{\frac{1}{2}\rho A C_L l_t} \cdot \frac{gl_t}{(V_w \cos\beta \; E_t)^2} = \frac{mg}{\frac{1}{2}\rho A C_L (V_w \cos\beta \; E_t)^2} = \frac{F_g}{L_{id}} \tag{3.12}$$

Except for the idealization of the kite speed, this product is present in the last term of the Equation 3.5. Consequently, it affects the tangential acceleration and the kite performance.

Having defined $G_r$, the results can be shown. The input parameters for the analysis are listed in Table 3.5. The aerodynamic values are taken from [6] and are related to the OktoberKite Makani prototype.

| Variable | Value | Units | Variable | Value | Units |
|---|---|---|---|---|---|
| $E$ | 10 | - | $l_t$ | 300 | $m$ |
| $\gamma_t$ | 0.5 | - | $\beta$ | 0 | $^\circ$ |
| $g$ | 9.81 | $m/s^2$ | $\Phi$ | $\Phi_{ci,g}^{opt}$ | |

Table 3.5: Input parameters for the generic results if centrifugal forces and gravity are considered

The efficiency, keeping the optimal opening angle $\Phi_{ci,g}^{opt}$, as function of $M$ and $G_r$ is present in Figure 3.15. As before, the blue zone represents the no fly-zone: for certain pairs of $M$ and $G_r$ the kite is not able to fly. The optimal opening angle $\Phi_{ci,g}^{opt}$ is obtained numerically downstream the simulation and it differs from $\Phi_{ci,ce}^{opt}$ (Equation 2.11) due to the presence of gravity. In the code, for each pair of $M$ and $G_r$, the opening angle is varied to find the optimal. From Figure 3.15, the higher $M$ and $Gr$, the greater the influence of gravity and the associated decrease in the maximum efficiency. The power losses are rather limited when $G_r < 0.5$ regardless of the value of $M$. On the contrary, for higher gravity ratio, $M$ must be quite low to allow the flight. In general, the maximum efficiency turns out to be more sensitive to $G_r$ than to $M$. A sudden decrease in performance is appreciable at the boundary of the no fly-zone. For this reason the lines are not smooth near the no-fly zone. A demanding simulation would have been necessary to have smooth lines without adding any useful consideration to the discussion.

Figure 3.16 shows the optimal opening angle $\Phi_{ci,g}^{opt}$ as a function of $G_r$ and $M$. Given a value of $G_r$, $\Phi_{ci,g}^{opt}$, and so the optimal path radius, increases as $M$ becomes higher to limit the centrifugal effects. On the contrary, given a value of $M$, the optimal path radius decreases as $G_r$ increases to limit the gravity effects. This concept will be explain in the following section. Moreover, $\Phi_{ci,g}^{opt}$ turns out to be lower than $\Phi_{ci,ce}^{opt}$ (it will be shown in the examples of Section 3.6).

The key rule of the non-dimensional parameters is evident. Given a system and its aerodynamic performances at a given wind speed, $M$ and $Gr$ can be determined. Their values finally inform about the efficiency of the system and the optimal flight path determined by $\Phi_{ci,g}^{opt}$.

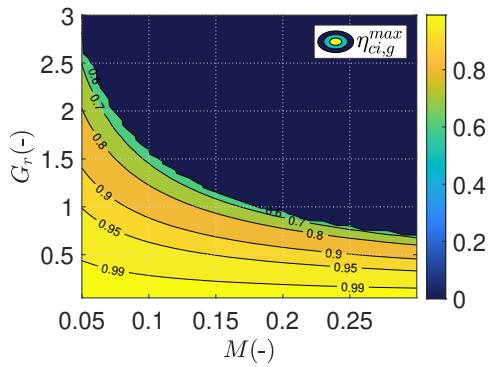


Figure 3.15: Efficiency $\eta_{ci,g}^{max}$ at $\Phi_{ci,g}^{opt}$ as a function of $M$ and $G_r$

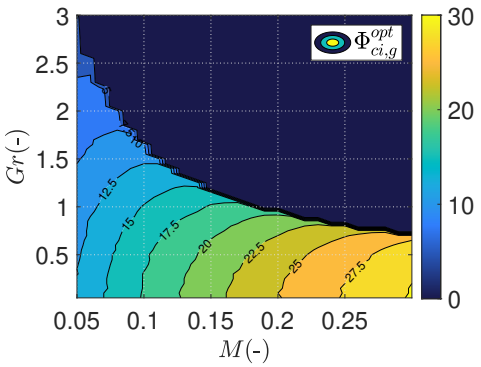


Figure 3.16: Optimal opening angle $\Phi_{ci,g}^{opt}$ as a function of $M$ and $G_r$

### 3.4.2. Power losses explanation

In this section, the causes of the power losses due to gravity are explained. The reference case is the optimal trajectory in the case only centrifugal force is considered (unitary efficiency). Consequently, all comparatives present in the text refer to this case with $\Phi = \Phi_{ci,ce}^{opt}$.

A subsection is devoted to each of the phenomena that affect efficiency. Then, a final summary subsection is presented. To help the comprehension, Figure 3.17 shows the phenomena associated to power losses in a schematic way. As before, during the description, references will be made to the numbers of the boxes shown in Figure 3.17.

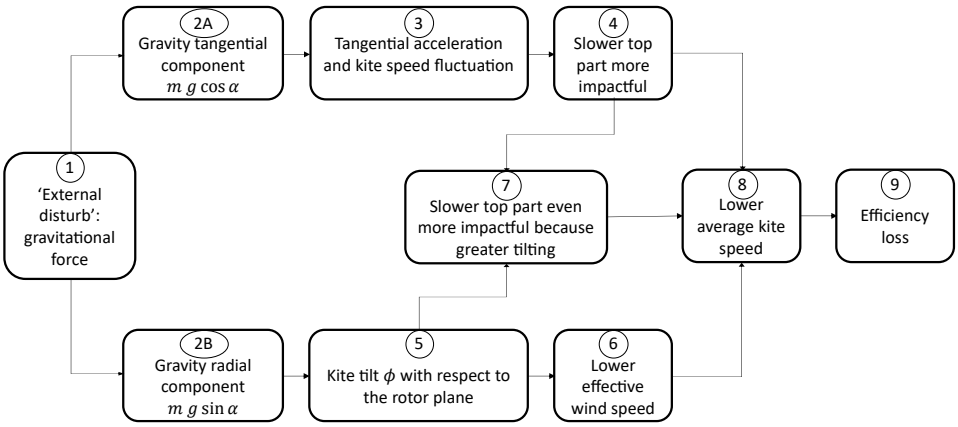


Figure 3.17: Conceptual diagram representing the physical phenomenon related to power losses due to gravity

As Figure 3.15 shows, even considering the optimal opening angle, $\Phi_{ci,g}^{opt}$, power losses are present. In this case, the 'external disturb' is the gravity force (box 1) which determines

power losses due to speed fluctuation and roll angle.

### Power losses due to kite speed variation

The tangential component $mg\cos\alpha$ (box 2A) makes the kite accelerates or decelerates in the tangential direction depending in which part of the loop it is flying. Indeed, $mg\cos\alpha$ implicitly appears in the last term of Equation 3.5 which is derived starting from the tangential balance. The consequence is a velocity fluctuation during the flight (box 3). As before, the speed variation makes the slower portion of the loop more influential once integrated in time (box 4), leading to an average kite velocity lower than $V_w E_t \cos\beta$ (box 8). Therefore, as happened for the introduction of elevation, the kite reaches its minimum velocity at the top of the loop and its maximum at the bottom.

### Power losses due to roll angle $\phi$

The radial components $mg\sin\alpha$ (box 2B) makes the kite roll to ensure radial balance. Indeed, $mg\sin\alpha$ implicitly appears in the last term of Equation 3.4 which is derived starting from the radial balance. The kite roll angle oscillates during the loop because the radial gravity component does the same (box 5). As before, the roll angle is the cause of a lower effective wind speed (box 6) and, therefore, a slower kite motion (box 8).

In addition, Figure 3.18 (a) shows the kite attitude in the top and bottom parts of the loop ($\alpha = 90°$ and $\alpha = 270°$) in the case of $\Phi^{opt}_{ci,ce}$. The top kite is flying towards the observer while the bottom one is further away from the observer entering the page. A greater tilting is needed at the top compared with the bottom because the aerodynamic forces are lower due to the minimum kite speed. Therefore, power losses due to $\phi$ are higher in the upper half of the loop.

Figure 3.18(b) shows the kite attitude in the side parts of the loop ($\alpha = 0°$ and $\alpha = 180°$) in the case of $\Phi^{opt}_{ci,ce}$. $\phi$ is null because in such positions the radial component of the gravity force is not present.

As it will be shown in the next chapters of the thesis, it is possible to limit this contribution to power losses using the tether in an active way.

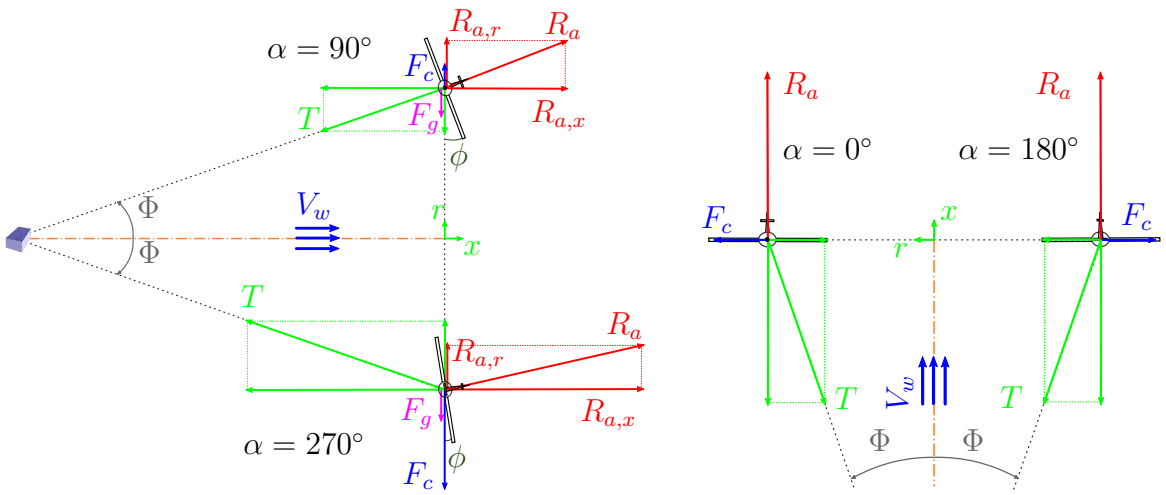


(a) *Side view of the system: kite attitude in the top ($\alpha = 90°$) and bottom ($\alpha = 270°$) parts of the loop*

(b) *Top view of the system: kite attitude in the lateral parts of the loop during the ascending (left kite, $\alpha = 0°$) and descending (right kite, $\alpha = 180°$) phases*

Figure 3.18: Kite attitude during the loop considering centrifugal and gravity forces in the case of $\Phi_{ci,ce}^{opt}$

### Conclusions

The top part doubly penalizes the efficiency because the roll angle is higher (Figure 3.18) and the kite motion is slower with respect to the bottom part (box 7).

To reduce the effects of the upper half of the loop, $\Phi_{ci,g}^{opt} < \Phi_{ci,ce}^{opt}$. A lower opening angle provides advantages in terms of both velocity fluctuation and roll angle. Regarding the first, the opening angle reduction makes the potential energy exchange in the loop lower and consequently also the speed variation. As for the second advantage, it makes the centrifugal force higher reducing the roll angle necessary in the more impactful top part of the loop (see Figure 3.18).

In the same way, given a certain $M$, higher $G_r$ translates in greater speed fluctuation and higher roll angle at same $\Phi_{ci,ce}^{opt}$. Therefore, $\Phi_{ci,g}^{opt}$ decreases as $G_r$ increases to reduce these effects.

## 3.5. Analysis with all phenomena

In this section, the physics of a FG-AWES flying a circular trajectory is presented considering gravity and a general mean elevation angle. In this way, all the analyzed phenomena

are considered together. This section of the chapter relates to box 3.5 in Figure 3.1.

A first subsection is devoted to the presentation of the results. Then, a subsecond section is entirely devoted to the explanation of the physical phenomena associated with power losses. In particular, it will be demonstrated how the combination of gravity and elevation is not linear.

### 3.5.1. Results

In this section, the results of the model are shown in non-dimensional terms.

The input parameters for the analysis are listed in Table 3.5. The aerodynamic values are taken from [6] and are related to the OktoberKite Makani prototype. Moreover, the chosen value of the mean elevation angle is $\beta = 30°$ because it is representative of the state of the art of the current AWESs [6].

| Variable | Value | Units | Variable | Value | Units |
|---|---|---|---|---|---|
| $E$ | 10 | - | $l_t$ | 300 | $m$ |
| $\gamma_t$ | 0.5 | - | $\beta$ | 30 | $\circ$ |
| $g$ | 9.81 | $m/s^2$ | $\Phi$ | $\Phi_{ci}^{opt}$ | $\circ$ |

Table 3.6: Input parameters for the generic results if centrifugal forces, gravity and elevation are considered

Figure 3.19 shows the model results varying both $M$ and $G_r$, keeping the opening angle at its optimal value $\Phi_{ci}^{opt}$ (which is obtained numerically). Obviously, higher are both $G_r$ and $M$, lower is the efficiency. Comparing Figure 3.19 with Figure 3.15 the degrading effects due to the additions of elevation are evident. Higher are $G_r$ and $M$, higher are the differences. Even the no-fly zone is larger.

Figure 3.20 shows the optimal opening angle $\Phi_{ci}^{opt}$ as a function of $G_r$ and $M$. The trend is similar to that of Figure 3.16 but in this case the optimal opening angle is a little higher due to the presence of elevation. Indeed, a too small opening angle with respect to $\Phi_{ci,ce}^{opt}$ would cause a high roll angle in the descending phase and related power losses (see Section 3.3.2).

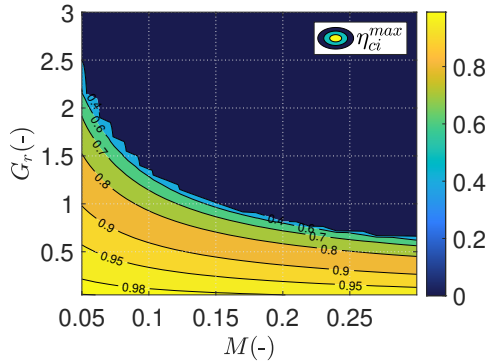


Figure 3.19: Efficiency $\eta_{ci}^{max}$ at $\Phi_{ci}^{opt}$ and with $\beta = 30°$ as a function of $M$ and $G_r$

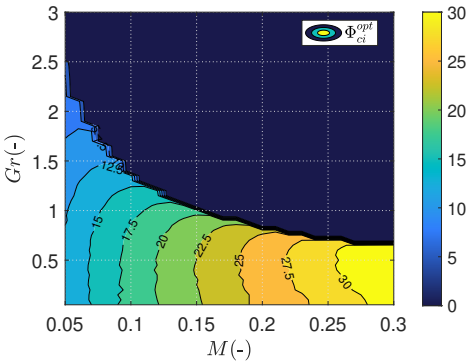


Figure 3.20: Optimal opening angle $\Phi_{ci}^{opt}$ with $\beta = 30°$ as a function of $M$ and $G_r$

### 3.5.2. Power losses explanation

Looking at figures 3.15 and 3.19, it is clear how the additional power loss provided by the addition of elevation is not negligible. This seems to be in disagreement with Figure 3.7 which shows how power losses due to elevation alone are negligible. In fact, the effects of gravity and elevation sums together in a non linear way.
Both effects contributes to slower the kite in the top and accelerate it in the bottom part of the loop. This effect is non linear because the aerodynamic forces depend on the square of the relative speed. Moreover, while the gravity tends to tilt the kite in the top and bottom parts of the loop, the elevation affected the roll angle on the side parts of the circular trajectory. As a result, the average kite roll angle is much higher leading, together with a higher velocity fluctuation, to a significant decrease in efficiency with respect to the previous case.
As a conclusion, it is possible to state that the superposition principle is not applicable.

## 3.6. Numerical examples

In this section of the chapter, numerical examples are proposed to show the theoretical knowledge learned in the previous sections. In particular, four cases with different elevation and different influence of gravity are analyzed and compared in the same time. Two cases have null elevation while the others have $\beta = 30°$. In turn, to assess the different influence of gravitational force, only one parameter is modified: the wind speed is changed from 10 $m/s$ to 7.5 $m/s$. However, with equal values of $G_r$ and $M$, same results can be obtained by varying other parameters, even in more than one at the same time. Table 3.7 summarizes the conditions for the four cases.

| Case | $V_w$ $[m/s]$ | $\beta$ [°] |
|---|---|---|
| A | 10 | 0 |
| B | 7.5 | 0 |
| C | 10 | 30 |
| D | 7.5 | 30 |

Table 3.7: Input values of wind speed and elevation for the four (A, B, C and D) cases

The input parameters, valid for all the cases, refer to Makani's OktoberKite prototype [6] and are shown in Table 3.8.

| Variable | Value | Units | Variable | Value | Units |
|---|---|---|---|---|---|
| $E$ | 10 | - | $C_L$ | 1.5 | - |
| $A$ | 50 | $m^2$ | $l_t$ | 300 | $m$ |
| $\gamma_t$ | 0.5 | - | $m$ | 1850 | $kg$ |

Table 3.8: Input parameters for numerical examples related to the CiMo-FG-KiTe

With the inputs in Table 3.8 and referring to Equation 2.10, $M = 0.13$ while, referring to Equation 3.9, the values of $G_r$ varies for each cases and it is reported in Table 3.9.

| Case | $V_w$ $[m/s]$ | $\beta$ [°] | $M$ [-] | $G_r$ [-] |
|---|---|---|---|---|
| A | 10 | 0 | 0.13 | 0.66 |
| B | 7.5 | 0 | 0.13 | 1.18 |
| C | 10 | 30 | 0.13 | 0.88 |
| D | 7.5 | 30 | 0.13 | 1.57 |

Table 3.9: Values of $M$ and $G_r$ obtained with the inputs present in Table 3.8

Figure 3.21 shows the efficiency for the four cases as a function of $M$ and $\Phi$. The dark blue region represents the no-fly zone. Comparing the figures with Figure 3.3, the minor differences are present for the lowest value of $G_r$, thus for the case A. Even for such a small $G_r$, higher is $M$, higher are the differences because the gravity influence becomes greater. In general, from the four figures, the higher the $G_r$, the lower the efficiency values and the larger the no-fly zone. Indeed, high $G_r$ indicates a great gravitational impact and only very small $M$ values allow the kite to fly. As for the addition of elevation, cases C and D are heavily penalized compared to the others. In particular, adding elevation from case B to case D makes the kite no longer able to fly fro $M = 0.13$.

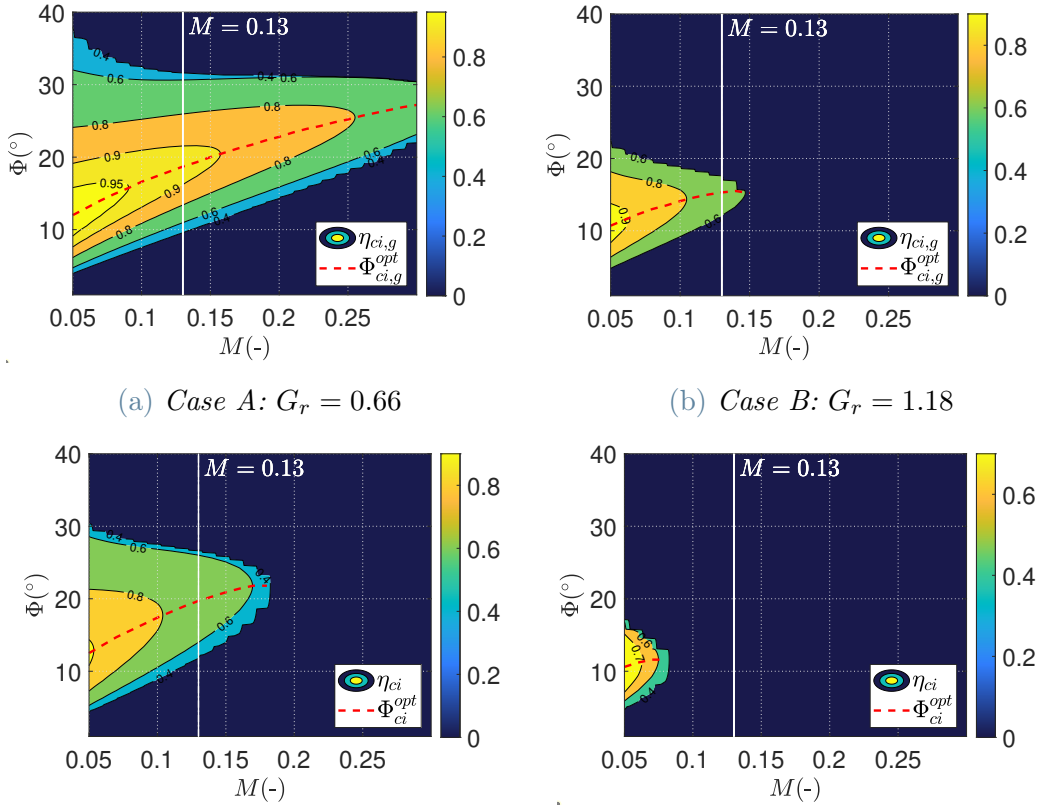


(a) *Case A:* $G_r = 0.66$

(b) *Case B:* $G_r = 1.18$

(c) *Case C:* $G_r = 0.88$

(d) *Case D:* $G_r = 1.57$

Figure 3.21: Efficiency as a function of $M$ and $\Phi$ in the four cases of Table 3.7

Figure 3.22 shows the optimal opening angle for the four cases compared with $\Phi^{opt}_{ci,ce}$ as a function of $M$ and $\Phi$. In all the cases, the optimal opening angle is lower than $\Phi^{opt}_{ci,ce}$ for the effects of gravity explained in Section 3.4.2. Moreover, for each case, the higher the $M$, the higher the gravity influence and the greater the difference.

Comparing case A and case B, the difference in the first is lower because lower is $G_r$ and so is gravity impact. Same consideration can be done between case C and D. As for the addition of elevation, comparing case A with case C, it makes the difference lower. A too small opening angle with respect to $\Phi^{opt}_{ci,ce}$ would cause a high roll angle in the descending phase and related power losses.

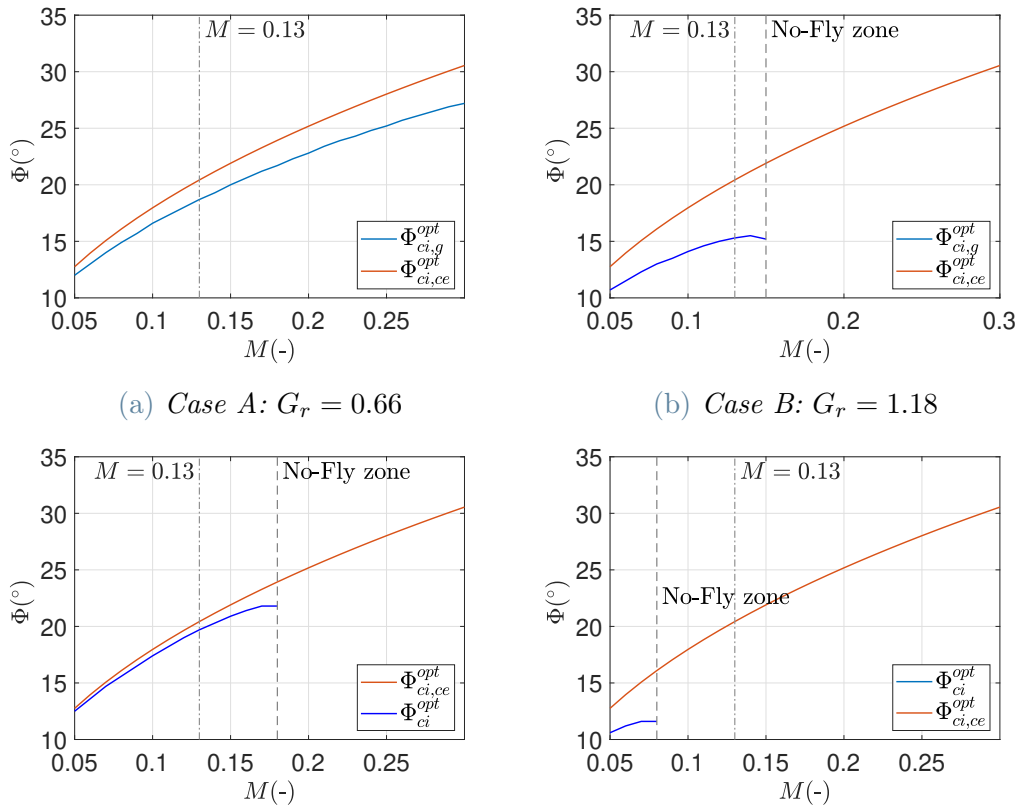


(a) *Case A:* $G_r = 0.66$

(b) *Case B:* $G_r = 1.18$

(c) *Case C:* $G_r = 0.88$

(d) *Case D:* $G_r = 1.57$

Figure 3.22: Comparison between the optimal opening angle in the four cases of Table 3.7 and $\Phi^{opt}_{ci,ce}$ as a function of $M$

In Table 3.10, the results for the optimal conditions are reported. Here is visible what is previously stated in Section 3.5.2: elevation cannot be neglected because its coupling with gravity causes strong non-linear effects. Indeed, from case A to case C the maximum efficiency drops of almost a 20% while from case B to case D elevation prevents the system from flying.

| Case | $V_w$ $[m/s]$ | $\beta$ [°] | $M$ [-] | $G_r$ [-] | $\Phi^{opt}$ ° | $\eta^{max}$ [%] |
|---|---|---|---|---|---|---|
| A | 10 | 0 | 0.13 | 0.66 | 18.9 | 92.0 |
| B | 7.5 | 0 | 0.13 | 1.18 | 15.5 | 69.7 |
| C | 10 | 30 | 0.13 | 0.88 | 20.0 | 73.3 |
| D | 7.5 | 30 | 0.13 | 1.57 | - | - |

Table 3.10: Results for the four cases in the optimal conditions

Figure 3.23 shows the kite attitude during the loop in case of the optimal conditions

reported in Table 3.10. Until elevation is added, $s_x$ oscillates during the loop because of the presence of $F_g \sin\alpha$ while $s_\alpha$ is almost not affected by gravity. Instead, in case C, $s_\alpha$ significantly oscillates during the loop because of the presence of $V_w \sin\beta \sin\alpha$ (due to elevation). Moreover, higher is $G_r$, higher is the variation of $s_x$ and, for Equation 2.6, higher is the roll angle variation. In case A $\overline{|\phi|} = 4.4°$ while in case C $\overline{|\phi|} = 6.3°$: the elevation makes increase the roll angle of about 1.5 times. Then, for the highest $G_r$ (case B), $\overline{|\phi|} = 13.9°$ and highest are the related power losses.

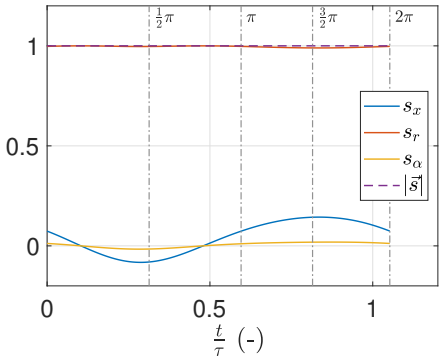


(a) *Case A:* $G_r = 0.66$ *and* $\Phi = \Phi^{opt}_{ci,g}$

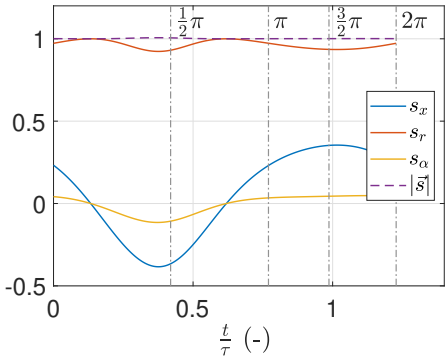


(b) *Case B:* $G_r = 1.18$ *and* $\Phi = \Phi^{opt}_{ci,g}$

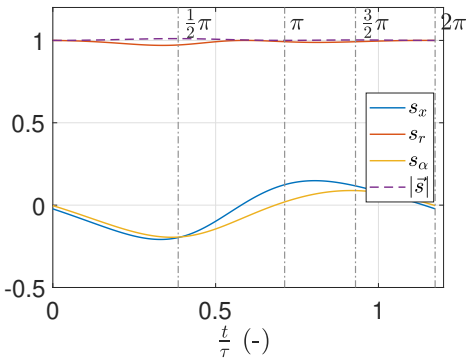


(c) *Case C:* $G_r = 0.88$ *and* $\Phi = \Phi^{opt}_{ci}$

Figure 3.23: Kite attitude during the loop as a function of time for the four cases in the optimal conditions of Table 3.10

Figure 3.24 shows the kite velocity (blue lines) during the loop in case of the above mentioned optimal conditions (Table 3.10). The dashed-red line represents the average kite speed while the dashed-black line the ideal kite speed. Comparing case A with case B, higher is $G_r$, higher is the difference between $\overline{V}_k$ and $V_w E_t \cos\beta$ and so lower is the efficiency. Moreover, higher is $G_r$, larger is the part in which the kite speed is lower than the ideal one informing about how influential is the slower top part of the loop compared to the bottom. Finally, adding elevation makes case C comparable to case B which has a

significantly lower wind speed as input.

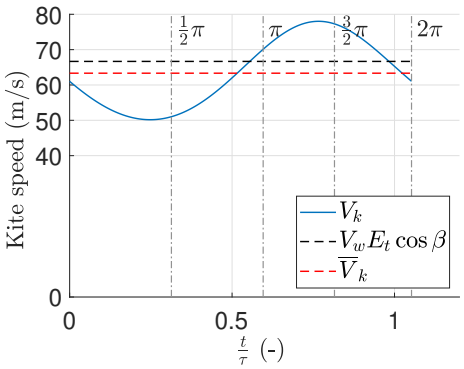


(a) *Case A:* $G_r = 0.66$ *and* $\Phi = \Phi_{ci,g}^{opt}$

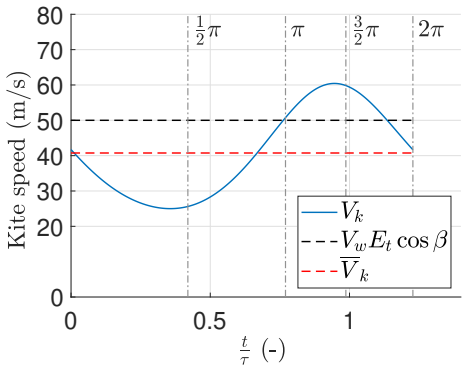


(b) *Case B:* $G_r = 1.18$ *and* $\Phi = \Phi_{ci,g}^{opt}$

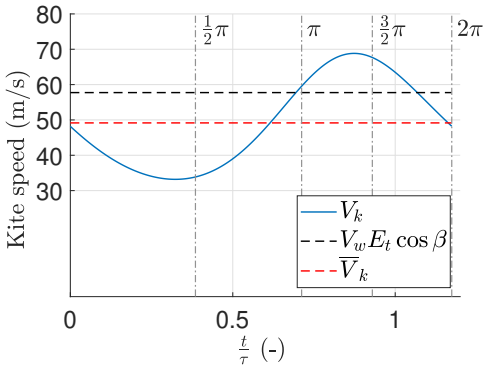


(c) *Case C:* $G_r = 0.88$ *and* $\Phi = \Phi_{ci}^{opt}$

Figure 3.24: Kite speed during the loop as a function of time for the four cases in the optimal conditions of Table 3.10

## 3.7. Summary and contributions

In this chapter, a physical model for a FG-AWES flying a circular crosswind path is presented. The centrifugal, elevation and gravity effects are considered.

Initially, in Section 3.1 the Circular Model for Fly Generation Tethered Kites (CiMo-FG-KiTe) is qualitatively derived starting from the Generic Model for Tethered Kites (GeMo-KiTe) introduced in the previous section. In the procedure, the reel-out velocity is null and a circular path is prescribed.

Then, the results of the model are shown adding each phenomena one at time to understand the associated physics.

Therefore, the results considering only centrifugal forces are presented in Section 3.2. It is shown that if the path radius (or the opening angle) has the right value, the centrifugal

force is balanced by the radial tether traction. The kite does not have to tilt and the efficiency is unitary.

Then, the results adding the elevation are shown in Section 3.3. The elevation makes the path partially downwind and upwind. Consequently, the kite is decelerated by going upwind and accelerating by flying downwind and tilts in the lateral parts of the loop to ensure radial equilibrium. The speed variation and the roll angle due to the kite tilting affect the efficiency. However, the related power losses turn out to be very small if only elevation is considered.

In Section 3.4, the results adding the gravity force in the case of null elevation are shown. The gravity makes both the kite roll angle and the kite velocity fluctuate during the loop. The influence of the related power losses depends on the product between two non-dimensional parameters. The first, $M$, represent the ratio between the centrifugal and aerodynamic forces. The second, $G_r$, represents the ratio between the gravity and centrifugal forces or, alternatively, the ratio between the potential energy exchange in the loop and the kite kinetic energy. $G_r$ is defined in this thesis for the first time. Higher are $M$ and $G_r$, higher is the gravity influence on system performance. Moreover, to reduce the gravitational effects, the optimal opening angle is smaller than the case if only centrifugal forces are considered.

Finally, in Section 3.5, all the effects are considered together. In particular, it shown how the elevation effects are not negligible anymore when considered together with gravity. Indeed, the superposition principle is not valid because gravity and elevation sums together in a non linear way.

The physical considerations present in this chapter can be useful to the AWES research community because they allow a detail comprehension of centrifugal, elevation and gravity effects by generalizing them as a function of non-dimensional parameters. Moreover, a new non-dimensional parameter, $G_r$, relating to gravity has been defined. All the mentioned considerations can be useful to crosswind AWES developers during design exploration.

# 4 | Derivation of Makani Model and comparison

This Chapter of the thesis is devoted to the discussion of the analytical model proposed by Makani related to the power production of crosswind AWESs. The model investigates the effects of the circular trajectory together with that of elevation and gravity.

Makani's team developed the following model with the same purpose for which the GeMo-KiTe and CiMo-FG-KiTe has been previously presented. The aim is well stated by the sentence present in the first Makani report [6]:

*'All models are wrong, but some are useful by making extensive simplifying assumptions. Our goal is a relatively simple model that can be coded in an afternoon and teaches the big lessons on how to get power from a kite — the end result only needs to broadly capture the sensitivities to be useful.'*

Makani Model is discussed in [6] by Echeverri et al and, in this chapter, a critical overview after its derivation is provided.

Section 4.1 is devoted to the derivation of the model and the related assumptions. The three subsections describe the modelling of each different phenomenon. In Section 4.2 the results of the Makani Model are presented and compared to the ones obtained with the CiMo-FG-KiTe. A subsection is dedicated to the comparison without the elevation and another is devoted to the comparison considering elevation. In both cases, numerical examples are provided. Finally, in Section 4.3, the main differences and similarities between the models are highlighted. Moreover, it is stated under which conditions it is better to use one model or the other.

## 4.1. Makani Model

The aim of this section is to present the analytical model derived by Makani during its 13-years of study, practice and testing. The model is explained in depth in Makani's first

report [6].

Since not all the equations are derived in [6], this chapter gives a complete derivation with all the assumptions to be as clear as possible. For the same reason, some equations are derived as a function of non-dimensional parameters to make the model more complete and general. Moreover, some unnecessary steps are omitted for the understanding of the discussion. Finally, some parameters are assigned to different letters with respect to the ones used in [6] to be coherent with the nomenclature of this thesis.

The model results are not shown in this section but directly illustrated in the comparison section so as not to be repeated twice.

Makani's team aims to decouple power losses to derive an analytical expression for each contribution. In this way, the power equation becomes:

$$P = C_1 C_2 \dots C_n P_L \tag{4.1}$$

where $C_1, C_2, \dots, C_n$ are power coefficients related to each power losses and $P_L$ is the ideal power derived from Loyd [5]:

$$P_L = \frac{1}{2}\rho A C_D \gamma_t E_t^3 V_w^3 \tag{4.2}$$

where, again, $E_t = \frac{C_L}{C_D(1+\gamma_t)}$.
In this chapter, the focus is on the centrifugal, elevation and gravity power losses. Therefore, the power equation becomes:

$$P = C_{ce} C_\beta C_{grav} P_L \tag{4.3}$$

As done for the Horizontal Axis Wind Turbine (HAWT), Makani's team try to reference the power of an AWES to the power available in the wind, and to bundle power losses into a performance metric. For the HAWT case, $P_{HAWT} = \frac{1}{2}\rho S c_p V_w^3$ where $S$ is the swept area by the blades. Translating this to AWES, it is useful to define a performance metric, $\zeta$, in terms of the kite's wing area, rather than the swept area, such that:

$$P_{AWE} = \frac{1}{2}\rho A \zeta V_w^3 \tag{4.4}$$

In the 'Loyd conditions' (Equation 4.2), the performance metric becomes [1]:

$$\zeta_L = C_D \gamma_t E_t^3 \tag{4.5}$$

Both $P_L$ and $\zeta_L$ are the foundations on which the model is based on. As presented in [6], the power factors are treated separately and then unified to evaluate the overall efficiency which can be defined as:

$$C = C_{ce} C_\beta C_{grav} \tag{4.6}$$

Therefore, a first subsection is dedicated to the analytical derivation of $C_{ce}$. Then, a second subsection describes how the elevation losses are modeled and finally a third subsection introduces the power factor for the gravity force.

The main assumptions of the model are:

i. The forces acting on a wing are condensed into a single point K which is a point mass representation of the kite.

ii. The wind speed can be neglected with respect to the kite speed $V_k$ and so the relative wind velocity is $V_a \approx V_k$.

iii. Pure fly generation system.

iv. Span-wise direction always perpendicular to the relative wind velocity.

v. Side forces $F_Y$ generated by the wind interaction with the tail, the pylons, the on-board wind turbines and all the other components are neglected.

vi. Constant lift coefficient $C_L$ and drag coefficient $C_D$. Perfect and instantaneous control is assumed to maintain constant the angle of attack.

vii. To simplify the analysis the tether is considered inelastic without any sagging.

viii. Constant wind speed during time (no turbulence) and uniform wind speed as a function of altitude.

[1] If the drag of the tether is considered, the reference performance metric is $\zeta_0$. The definition is the same of Equation 4.5, but the drag coefficient does not include the drag of the tether.

### 4.1.1. Centrifugal power coefficient

In this section, Makani modeling for the centrifugal forces is presented. Not all the equations shown in this section are present in [6]. In any case, they are all attributable to those present in [6].

The kite is able to fly in a circular trajectory thanks to radial forces that counterbalance the centrifugal one. These active forces are the traction of the tether and the lift force provided by the tilted kite. Makani makes two further assumptions in addition to those already reported:

ix. Small opening angle $\Phi$.

x. Small roll angle $\phi$, meaning that the kite is flying close to its optimal path.

Knowing that the centrifugal force is:

$$F_c = m\frac{V_k^2}{R} \tag{4.7}$$

with the same reference system of Figure 2.4 and looking at Figure 3.5 (or Figure 3.6), the tether traction can be found from equilibrium along the $x$-axis:

$$T = \frac{L\cos\phi}{\cos\Phi} \tag{4.8}$$

The side-force $F_Y$ should be present but it is set to zero for the assumption number (v). The force balance along the radial direction is:

$$F_c = L\sin\phi + T\sin\Phi \tag{4.9}$$

The kite roll angle $\phi$, makes the effective wind speed lower and equal to $V_w\cos\phi$. The associated power factor is:

$$C_{ce} = \cos(\phi)^3 \tag{4.10}$$

Therefore, being $L = \frac{1}{2}\rho A C_L V_a^2$, from Equations 4.7, 4.8, 4.9 and assumption (ii), it is possible to derive the roll angle:

$$\phi = \sin^{-1}\left(\frac{m}{\frac{1}{2}\rho A C_L l_t \sin\Phi} - \frac{\cos\phi}{\cos\Phi}\sin\Phi\right) \tag{4.11}$$

Applying both the further assumptions (ix) and (x), the roll angle due to centrifugal force becomes:

$$\phi = \sin^{-1}\left(\frac{m}{\frac{1}{2}\rho A C_L l_t \sin\Phi} - \sin\Phi\right) \tag{4.12}$$

Introducing in the last equation the $M$ parameter (Equation 2.10):

$$\phi = \sin^{-1}\left(\frac{M}{\sin\Phi} - \sin\Phi\right) \tag{4.13}$$

By utilizing the identity $\cos(\sin^{-1}\phi) = \sqrt{1-\phi^2}$, it is possible to find the power coefficient for the centrifugal effect:

$$C_{ce} = \left(1 - \left(\frac{M}{\sin\Phi} - \sin\Phi\right)^2\right)^{3/2} \tag{4.14}$$

Imposing null the derivative of Equation 4.14 with respect to $\Phi$, it is possible to find the optimal opening angle for which $C_{ce} = 1$:

$$\Phi^{opt} = \arcsin\left(\sqrt{M}\right) \tag{4.15}$$

This is the value of $\Phi$ for which $\phi = 0°$ and the effective wind speed is the maximum. Figure 4.1 shows the centrifugal power coefficient $C_{ce}$ as a function of $M$ and $\Phi$. As before, the dark blue zone is the no fly-zone and the red-dashed line indicates the optimal conditions of Equation 4.15 for which $C_{ce} = 1$. Comparing Figure 4.1 with Figure 3.3 the similarities are strong. The main differences occur for high values of $\Phi$ in which assumption (ix) starts to be less valid.

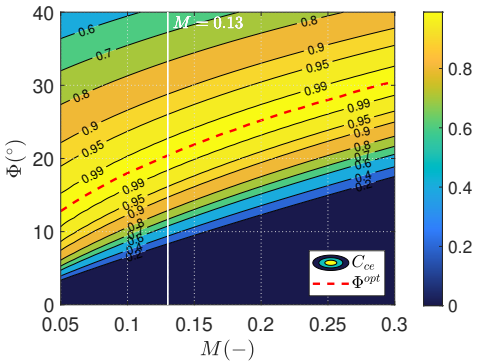


Figure 4.1: Centrifugal power coefficient $C_{ce}$ as a function of $M$ and $\Phi$

Figure 4.2 shows the trend of $C_{ce}$ and $\eta_{ci,ce}$ (Equation 2.9) for $M = 0.13$ (value taken from the numerical examples present in the previous chapter). The $C_{ce}$ is higher than $\eta_{ci,ce}$. Far from the optimal conditions the difference increases because the kite roll angle is more relevant and hypothesis (x) starts to be stronger. Moreover for high $\Phi$ the difference are higher because assumption (ix) on the small opening angle starts to be stronger.

Figure 4.3 compares the trend of the optimal opening angle calculated with Equations 4.15 and 2.11. In the optimal conditions, the kite roll angle is null and the differences between the trends are only due to the assumption (ix). For such a reason, for high values of $\Phi^{opt}$ (ans so $M$) the trends start to diverge. In particular, for $\Phi < 20°$ the difference is not so marked, while it becomes more evident for $\Phi > 20°$.

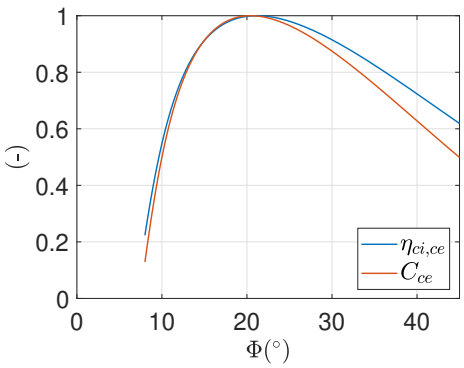


Figure 4.2: Comparison between $C_{ce}$ and $\eta_{ci,ce}$ as a function of $\Phi$ for $M = 0.13$

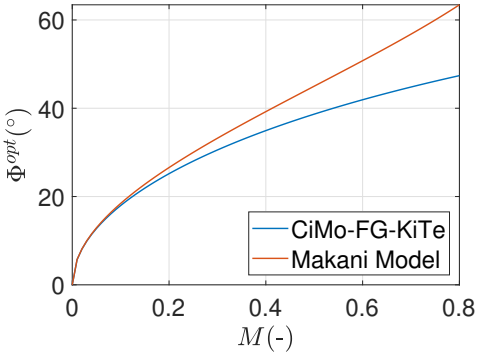


Figure 4.3: $\Phi^{opt}$ obtained with Makani Model and CiMo-FG-KiTe as a function of $M$

In conclusion, the similarities between $\eta_{ci,ce}$ (Equation 2.9) and $C_{ce}$ (Equation 4.14) are strong. In particular, the differences are due to assumptions (ix) and (x) during the

derivation of $C_{ce}$. Consequently, the analytical formulation of $\eta_{ci,ce}$ has a more general validity.

### 4.1.2. Elevation power coefficient

This section describes how Makani Models the losses for the mean elevation angle $\beta$. According to Makani, the elevation simply attenuates the effective wind speed. Since power scales with $V^3_{w,eff}$, it is possible to define a power coefficient to represent the elevation losses:

$$C_\beta = \cos(\beta)^3 \tag{4.16}$$

### 4.1.3. Gravity power coefficient

This section introduces Makani modeling for the gravitational force. Before going straight to the model derivation, the following premise is necessary. Makani identifies three main flight strategies on which gravity losses depend:

1. Constant kite speed. 'This strategy causes large swings in power as the potential energy is effectively pushed into the grid on the down stroke, and pulled back out on the upstroke' [6].
   If this power oscillation is higher than the power produced by the on-board turbines, the grid is effectively used as a battery. In the 'grid battery mode', the system pays the difference between the energy fed into the grid and the energy returned back to the kite, exactly as the round trip efficiency in standard batteries.

   As the kite power production increases, it utilizes the grid battery less and less. When the power from the wind is larger than the power fluctuations due to the potential energy, the grid is not used anymore.

2. The opposite strategy is to completely convert the potential energy of the kite into kinetic energy providing the highest change in the kite speed.

3. An intermediate strategy that converts part of the potential energy in the kite's kinetic energy and the remain part into electricity.

Makani's team uses two different power coefficients to consider the effects of gravity. $C^V_{grav}$ considers the kite speed deviation from the optimal value, while $C^{grid}_{grav}$ takes into account the efficiency of the grid used as a battery. Therefore, the comprehensive power coefficient accounting for gravity losses is $C_{grav} = C^V_{grav} C^{grid}_{grav}$.

Both $C^V_{grav}$ and $C^{grid}_{grav}$ change according to the chosen strategy. Since in the previous model the 'grid-battery' is not involved, strategy number 2 is considered to be consistent for the comparison. Only the effects of speed variation are taken into account and so $C_{grav} = C^V_{grav}$ since $C^{grid}_{grav} = 1$. [2]

The further assumptions needed to model the effects of gravity are:

iv. The average kite speed, $\overline{V_k}$, is the average with respect to loop angle $\alpha$ rather than to time. With this assumption, it is not considered that more time is spent in the slower portion of the loop than the faster one. Therefore, the average kite speed is a overestimated.

v. Instant by instant, the weight force is the only cause of the kite acceleration as it is assumed that the other forces balance each other.

The starting point to derived the analytical expression for $C^V_{grav}$ is the force balance along the tangential axis. For assumption (v), the tangential forces (excluding the weight force) compensate each other. Therefore, with reference to Figure 4.4:

$$D_t + D = L \cdot \frac{V_w \cos\beta}{V_k} \tag{4.17}$$

Making explicit the forces:

$$\frac{P}{V_a} + \frac{1}{2}\rho C_D A V_a^2 = \frac{1}{2}\rho C_L A V_a^2 \left(\frac{V_w \cos\beta}{V_a}\right) \tag{4.18}$$

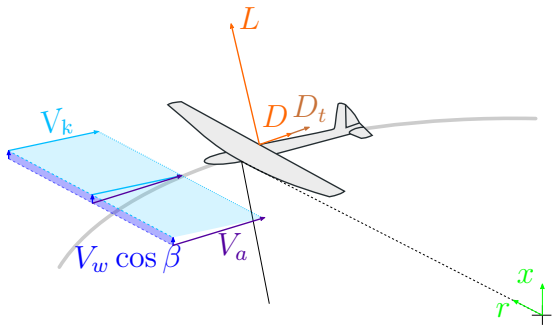


Figure 4.4: Velocity triangle and forces on the rigid kite

[2] Makani defines a coefficient that represents the chosen flight strategy: $K_{grav} = \frac{\Delta E_k}{\Delta E_p} = \frac{V^2_{k,max} - V^2_{k,min}}{4Rg\cos\beta}$. Since in this section only strategy 2 is considered, $K_{grav} = 1$ always. Consequently, this coefficient is not present in the following Equations for readability and clarity. For a more complete and general analysis depending on the flight strategy, refer to [6].

Exploiting assumption (ii) of $V_k \approx V_a$:

$$P = \frac{1}{2}\rho A V_k^3 \left( C_L \frac{V_w \cos\beta}{V_k} - C_D \right) \tag{4.19}$$

From Equation 4.19, the general performance metric $\zeta_v$ (where the subscript $v$ highlights the dependency on $V_k$) can be derived:

$$\zeta_v = C_L \left( \frac{V_k}{V_w \cos\beta} \right)^2 - C_D \left( \frac{V_k}{V_w \cos\beta} \right)^3 \tag{4.20}$$

The aim is to explicit the kite speed as a function of the loop angle. Applying assumption (iv), the average kite speed is:

$$\overline{V_k} = \frac{1}{2}(V_{k,max} + V_{k,min}) \tag{4.21}$$

Moreover, with this flight strategy, the potential energy variation in the loop is completely transformed into kinetic energy of the kite:

$$\Delta E_p = 2Rmg\cos\beta = \Delta E_k = m\frac{(V_{k,max}^2 - V_{k,min}^2)}{2} \tag{4.22}$$

From Equations 4.21 and 4.22, the variation of the kite velocity in the loop $\Delta V_k$ is obtained:

$$\Delta V_k = \frac{2Rg\cos\beta}{\overline{V_k}} \tag{4.23}$$

It is possible to find the kite speed as a function of $\alpha$ applying assumption (v) to the Newton's dynamic law. With reference to Figure 2.7, the cardinal Equation is:

$$-g\cos\beta \ \cos\alpha = \ddot{\alpha}R = \frac{dV_k}{dt} \tag{4.24}$$

After a few steps and noting that the velocity at $\alpha = 0$ is equal to the $\overline{V_k}$:

$$-g\cos\beta \int_0^{\alpha} \cos\tilde{\alpha}\frac{d\tilde{\alpha}}{\dot{\alpha}} = \int_{\overline{V_k}}^{V_k} d\tilde{V_k} \tag{4.25}$$

With the previous assumption of all loop angles weighted evenly ((iv)):

$$-\frac{g\cos\beta}{\overline{\dot{\alpha}}}\int_0^{\alpha}\cos\tilde{\alpha}d\tilde{\alpha}=\int_{\overline{V_k}}^{V_k}d\tilde{V_k} \tag{4.26}$$

by solving the integral:

$$V_k=\overline{V_k}-\frac{gR\cos\beta\ \sin\alpha}{\overline{V_k}} \tag{4.27}$$

Finally, using Equation 4.23, the kite velocity as function of the loop angle is:

$$V_k=\overline{V_k}-\frac{\Delta V_k}{2}\ \sin\alpha \tag{4.28}$$

Since $\zeta_v$ is function of the kite speed, it is function of the loop angle $\alpha$ as well. Thus, combining Equations 4.20 and 4.28, it is possible to find an average loop value of the performance metric:

$$\begin{aligned}\overline{\zeta_v}&=\frac{1}{2\pi}\int_0^{2\pi}\zeta_v d\alpha=\\&=C_L\left(\frac{\overline{V_k}}{V_w\cos\beta}\right)^2\left(1+\frac{\Delta V_k^2}{8\overline{V_k}^2}\right)-C_D\left(\frac{\overline{V_k}}{V_w\cos\beta}\right)^3\left(1+\frac{3\Delta V_k^2}{8\overline{V_k}^2}\right)\end{aligned} \tag{4.29}$$

The power coefficient for the power losses due to non optimal kite speed is defined by the ratio between $\overline{\zeta_v}$ and $\zeta_L$ [3]:

$$C_{grav}=C_{grav}^V=\frac{\overline{\zeta_v}}{\zeta_L} \tag{4.30}$$

## 4.2. Comparison with the CiMo-FG-KiTe

In this section, a comparison between the CiMo-FG-KiTe (Chapter 3) and the Makani proposal (Section 4.1) is performed. The aim of the comparison is to highlight whether the modelings provide the same result or not and to critically explain the differences.

A first subsection is dedicated to the comparison without considering the elevation. The aim is to isolate and understand the effects of the two additional hypotheses ((iv) and

[3]The related equation present in Makani's first report [6] is $C_{grav}=\frac{\overline{\zeta_v}}{\zeta_0 C_{TD}}$ where $C_{TD}$ is a power coefficient representative of the tether's drag. The presence is dictated by the Makani's purpose of having all separate power coefficients; for a more detailed explanation refer to [6]. However, since the tether drag and sag are not considered in this section, $C_{TD}=1$, so it is omitted.

(v)) made by Makani during the gravity power coefficient analytical derivation. A second subsection is dedicated to the comparison between the two models considering also elevation. In both cases, numerical examples are reported to highlight the differences in case of small and strong gravity influence.

To make a fair comparison a premise is needed. The extracted power modeled by the CiMo-FG-KiTe is:

$$P = \eta_{ci} \cdot P_{id} = \eta_{ci} \cdot \frac{1}{2} \rho A C_D \gamma_t E_t^3 V_w^3 \cos\beta^3 \tag{4.31}$$

The extracted power modeled by Makani is:

$$P = C_{ce} C_{grav} C_\beta \cdot P_L = C_{ce} C_{grav} C_\beta \cdot \frac{1}{2} \rho A C_D \gamma_t E_t^3 V_w^3 \tag{4.32}$$

To make a fair comparison, both models have to refer to the same power. Observing from the last two equations that $P_{id} = P_L \cos\beta^3$ and remembering that $C_\beta = \cos\beta^3$ (Equation 4.16), $P_{id} = P_L C_\beta$. Moreover, at the end of Section 4.1.1, the more general validity of $\eta_{ci,ce}$ with respect to $C_{ce}$ is explained. Consequently, to make the comparison more meaningful, $C_{ce}$ is made equal to $\eta_{ci,ce}$ and the two assumptions (ix) and (x) are not taken into account.

In conclusion, the right power coefficient to compare with $\eta_{ci}$ is:

$$C = C_{ce} C_{grav} \tag{4.33}$$

where $C_{grav}$ is expressed in Equation 4.30 and, with reference to Equation 2.9:

$$C_{ce} = \eta_{ci,ce} = \cos\Phi^3 \left( M + \sqrt{1 - \frac{M^2}{\tan\Phi^2}} \right)^3$$

### 4.2.1. Comparison without elevation

In this subsection, the CiMo-FG-KiTe is compared to the model proposed by Makani, in case the elevation is not considered. In this way, the differences between the two models are only due to the assumptions (iv) and (v).
The input values for the comparison are given in Table 4.1. For both the models, the optimal opening angle is obtained downstream the simulation varying $\Phi$ in the code.

| Variable | Value | Units | Variable | Value | Units |
|---|---|---|---|---|---|
| $E$ | 10 | - | $C_L$ | 1.5 | - |
| $\rho$ | 1.225 | $kg/m^2$ | $l_t$ | 300 | $m$ |
| $\Phi$ | $\Phi^{opt}$ | $^\circ$ | $\beta$ | 0 | $^\circ$ |
| $g$ | 9.81 | $m/s^2$ | $\gamma_t$ | 0.5 | - |

Table 4.1: Input parameters for the comparison between the CiMo-FG-KiTe and the Makani Model with null elevation

Figure 4.5 compares the maximum power coefficient $C^{max}$ and the maximum efficiency $\eta_{ci,g}^{max}$ as a function of $M$ and $G_r$. In particular, Figure 4.5 (a) shows the results of Makani Model while in Figure 4.5 (b) are reported again the results of CiMo-FG-KiTe (the same as in Figure 3.15). For low values of $G_r$ and $M$, the results of the two models are very similar. This happens because gravity has a small influence and the related assumptions (iv) and (v) too. On the contrary, the highest deviations are present for high values of $M$ and $G_r$, i.e. in the zone in which the gravity has a strong impact. In such conditions, $\eta_{ci,g}^{max}$ drops earlier than $C^{max}$, providing a no-fly zone much larger and consequently worst performance. This difference is due to both the simplifying assumptions (iv) and (v) made by Makani's team to model the gravity effects.

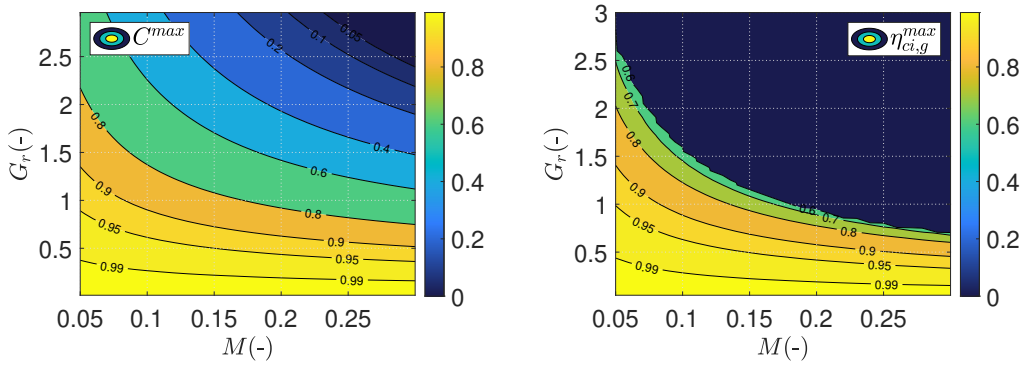


(a) *Makani Model:* $C^{max}$ *as a function of* $G_r$ *and* $M$ *for* $\beta = 0^\circ$

(b) *CiMo-FG-KiTe:* $\eta_{ci,g}^{max}$ *as a function of* $G_r$ *and* $M$ *for* $\beta = 0^\circ$

Figure 4.5: Comparison between $C^{max}$ (Makani Model) and $\eta_{ci,g}^{max}$ (CiMo-FG-KiTe) as a function of $M$ and $G_r$ for $\beta = 0^\circ$

To understand which of the hypotheses is the most impactful, assumption (iv) is added to the CiMo-FG-KiTe. The derivation of the model is the same as that in Section 3.1 but

the efficiency, called $\eta\prime$, is calculated integrating on the loop angle instead of over time[4]:

$$\eta\prime_{ci} = \frac{\frac{1}{2\pi}\int_0^{2\pi}(\dot{\alpha}RK_2)^3 d\alpha}{(V_w E_t \cos\beta)^3} \tag{4.34}$$

Figure 4.6 shows the difference $\eta\prime_{ci,g}^{max} - \eta_{ci,g}^{max}$ as a function of $M$ and $G_r$. It demonstrates that assumption (iv) is a non-conservative hypothesis because it overestimates the average kite speed as well as the efficiency. Indeed, this hypothesis nullifies the power losses due to the kite speed fluctuation in the loop because time integration is not considered anymore. Nevertheless, both 'the shape' and the no-fly zone are not affected by the hypothesis.

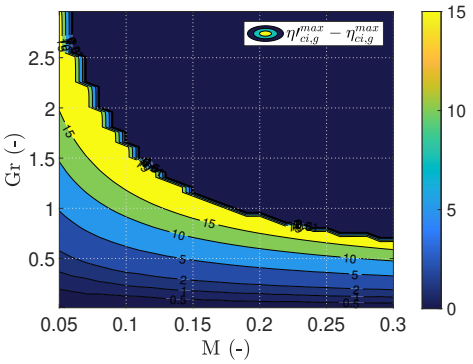


Figure 4.6: Difference between $\eta\prime_{ci,g}^{max}$ and $\eta_{ci,g}^{max}$ as a function of $M$ and $G_r$

Figure 4.7 compares $C^{max}$ (a) with $\eta\prime_{ci,g}^{max}$ (b) as a function of $M$ and $G_r$. In this case, the only difference is due to the assumption (v), related to the resolution of the equations of motion considering the weight force. In particular, in the conditions in which the kite is able to fly, their resolution leads to higher efficiency with respect to the Makani results. Consequently, given the presence of gravity, the kite autonomously tends to an attitude which increases performance. On the contrary, the resolution of the motion is the cause of the no-fly zone while in the Makani results the kite is still flying with a smoothly efficiency decrease.

[4]To be rigorous, this assumption should be used throughout the derivation of the model, as done by Makani, and not just in the final definition of efficiency. However, an even comparison is difficult in the case of such different derivations. Consequently, the methodology illustrated seemed to be the most sensible in terms of qualitative considerations.

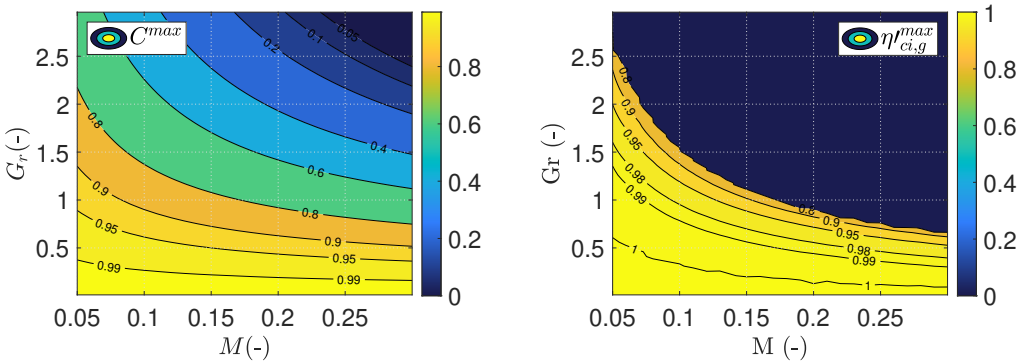


(a) *Makani Model: $C^{max}$ as a function of $G_r$ and $M$ for $\beta = 0°$*

(b) *CiMo-FG-KiTe: $\eta I_{ci,g}^{max}$ as a function of $G_r$ and $M$ for $\beta = 0°$*

Figure 4.7: Comparison between $C^{max}$ (Makani Model) and $\eta I_{ci,g}^{max}$ (CiMo-FG-KiTe with assumption (iv)) as a function of $M$ and $G_r$ for $\beta = 0°$

Figure 4.8 compares the trends of the optimal opening angle obtained with the two models as a function of $M$ and $G_r$. Again, for low values of both $G_r$ and $M$, the optimal opening angle does not differ significantly if calculated with one model or the other. For high values of $M$ and $G_r$, the gravity impact is strong leading to big differences due to the aforementioned assumptions.

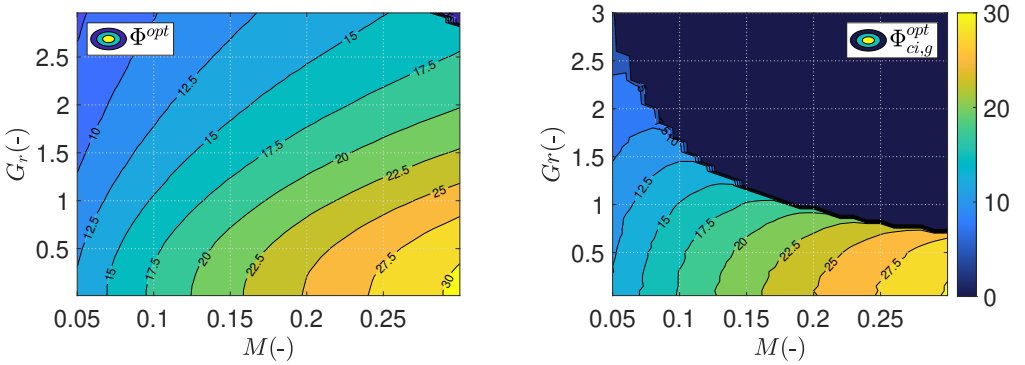


(a) *Makani Model: optimal opening angle as a function of $G_r$ and $M$ for $\beta = 0°$*

(b) *CiMo-FG-KiTe: optimal opening angle as a function of $G_r$ and $M$ for $\beta = 0°$*

Figure 4.8: Comparison between the optimal opening angle trends in the case of Makani Model and CiMo-FG-KiTe as a function of $M$ and $G_r$ for $\beta = 0°$

Summarizing, the results of the model are similar only for low values of $M$ and $G_r$ for two reasons:

1. The two simplifying hypotheses made by Makani have a low effect because gravity has small influence too.

2. The two simplifying hypotheses have opposite effects for such values of $M$ and $G_r$. Firstly, the non-resolution of the equations of motion considering the gravity force (assumption (v)) leads to lower efficiency (as the kite attitude does not adapt). Secondly, the omission of the power losses due to the kite speed fluctuation (assumption (iv)) leads to higher performance.

Moreover, in the other parts of the diagram, the differences are mainly attributable to the assumption (v), related to the equations of motion. The latter hypothesis makes the efficiency drops suddenly determining the no-fly zone.

## Numerical examples

In this part of the work, a numerical example shows the different results obtained using the two models. Two cases at $\beta = 0°$ with different influence of gravity are analyzed and compared in the same time. Only one parameter is modified: the wind speed is changed from 10 $m/s$ (case A) to 7.5 $m/s$ (case B). The values of $M$ and $G_r$ for these two cases are those reported in Table 3.9: $G_r = 0.66$ and $G_r = 1.18$ for case A and case B respectively and $M = 0.13$.

Figure 4.9 compares the system performance obtained with the two models as a function of $M$ and $\Phi$. For case A ($G_r = 0.66$), the main difference occurs for high values of $M$ and $\Phi$ for which the no-fly zone of the CiMo-FG-KiTe is larger. On the other hand, for case B ($G_r = 1.18$), the differences are greater. In particular, the results obtained with the CiMo-FG-KiTe present a no-fly zone much larger. As a result, higher is $G_r$, higher are the differences between the model results' for a given $M$.

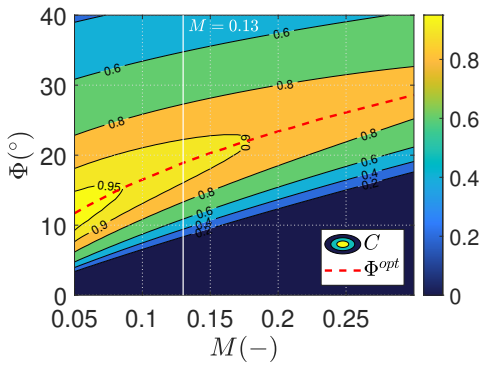


(a) *Case A - Makani Model: $C$ as a function of $\Phi$ and $M$*

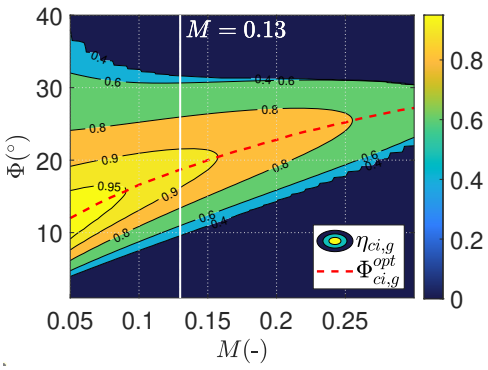


(b) Case A - *CiMo-FG-KiTe: $\eta_{ci,g}$ as a function of $\Phi$ and $M$*

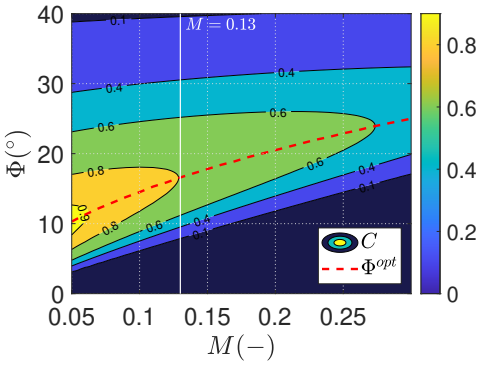


(c) *Case B - Makani Model: $C$ as a function of $\Phi$ and $M$*

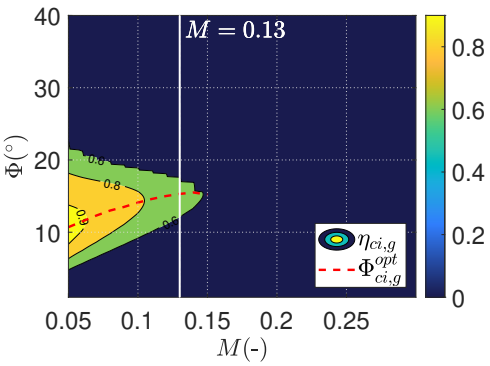


(d) Case B - *CiMo-FG-KiTe: $\eta_{ci,g}$ as a function of $\Phi$ and $M$*

Figure 4.9: Comparison of system performance for cases A and B as a function of $M$ and $\Phi$ obtained with Makani Model and CiMo-FG-KiTe

Focusing on the optimal conditions, Figure 4.10 compares the trends of the optimal opening angles obtained with the two models as a function of $M$. For case A, the trends start to diverge for high values of $M$, but they remain always similar due to the small $G_r$. On the other hand, significant differences can be appreciated in case B. Due to the high $G_r$, already starting from rather low values of $M$, the product between them (i.e. the influence of gravity) becomes relevant. As a result, the assumptions of Makani also become relevant causing the difference. In both cases, the CiMo-FG-KiTe provides a lower optimal opening angle because, as explained in the Section 3.4.2, it considers the kite attitude and the kite speed variation.

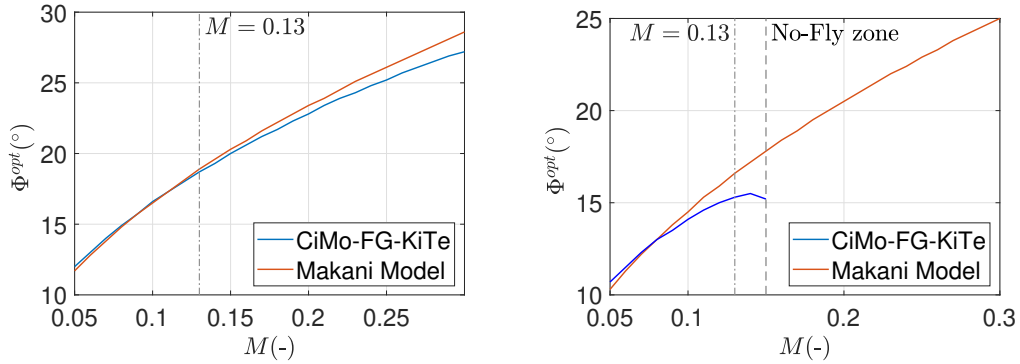


(a) *Case A* (b) *Case B*

Figure 4.10: Comparison between the trends of optimal opening angles provided by the two models for cases A and B as a function of $M$

The numerical results for the calculated values of $M$ and $G_r$ are present in Table 4.2. The numbers confirm what was previously presented. For low values of $G_r$, the results do not differ significantly. On the other hand, in case B (high $G_r$) the power generation estimation of the two models differs of approximately 10%.

| Case | $V_w$ $[m/s]$ | $\beta$ [°] | $M$ [-] | $G_r$ [-] | CiMo-FG-KiTe | | Makani Model | |
|---|---|---|---|---|---|---|---|---|
| | | | | | $\Phi^{opt}_{ci,g}$ [°] | $\eta^{max}_{ci,g}$ [%] | $\Phi^{opt}$ [°] | $C^{max}$ [%] |
| A | 10 | 0 | 0.13 | 0.66 | 18.9 | 92.0 | 19.2 | 92.4 |
| B | 7.5 | 0 | 0.13 | 1.18 | 15.5 | 69.7 | 16.8 | 79.2 |

Table 4.2: Results for case A and case B in the optimal conditions

### 4.2.2. Comparison considering elevation

In this subsection, the CiMo-FG-KiTe is compared to that proposed by Makani in case the elevation is considered. The input values for the comparison are given in Table 4.3.

| Variable | Value | Units | Variable | Value | Units |
|---|---|---|---|---|---|
| $E$ | 10 | - | $C_L$ | 1.5 | - |
| $\rho$ | 1.225 | $kg/m^2$ | $l_t$ | 300 | $m$ |
| $\Phi$ | $\Phi^{opt}$ | ° | $\beta$ | 30 | ° |
| $g$ | 9.81 | $m/s^2$ | $\gamma_t$ | 0.5 | - |

Table 4.3: Input parameters for the comparison between the CiMo-FG-KiTe and the Makani Model considering elevation

For both the models, the optimal opening angle is obtained downstream the simulation.

Figure 4.11 compares the maximum efficiency $\eta_{ci}^{max}$ and the maximum power coefficient $C^{max}$ as a function of $M$ and $G_r$ obtained with the input of Table 4.3. In particular, Figure 4.11 (a) shows the result obtained with the Makani Model while Figure 4.11(b) shows the results obtained with the CiMo-FG-KiTe. Considering elevation, the differences are even more evident. In the power factor definition of Equation 4.33, the addition of elevation affects only $C_{grav}$. The latter becomes higher because the potential energy exchange (Equation 4.22) and the consequent kite speed variation during the loop (Equation 4.23) are lower. As a result, $C^{max}$ increases when elevation is considered. On the contrary, the elevation makes the performance predicted by the CiMo-FG-KiTe worst because of the slightly downwind and upwind motion discussed in Section 3.3.2. As a result, the differences are even more accentuated.

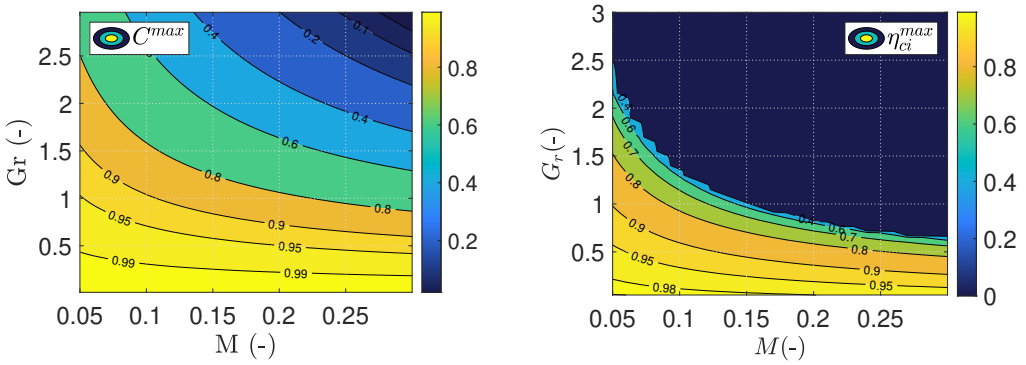


(a) *Makani Model:* $C^{max}$ *as a function of* $G_r$ *and* $M$ *for* $\beta = 30°$

(b) *CiMo-FG-KiTe:* $\eta_{ci}^{max}$ *as a function of* $G_r$ *and* $M$ *for* $\beta = 30°$

Figure 4.11: Comparison between $C^{max}$ (Makani Model) and $\eta_{ci}^{max}$ (CiMo-FG-KiTe) as a function of $M$ and $G_r$ for $\beta = 30°$

Figure 4.12 compares the trends of the optimal opening angle obtained with the two models as a function of $M$ and $G_r$, in case of $\beta = 30°$. Figure 4.12 (a) shows the Makani results while Figure 4.12 (b) the CiMo-FG-KiTe results. The same considerations can also be made for the optimal opening angle: adding elevation slightly affects Makani's results, while the trend of the other model is changed and the no-fly zone is larger.

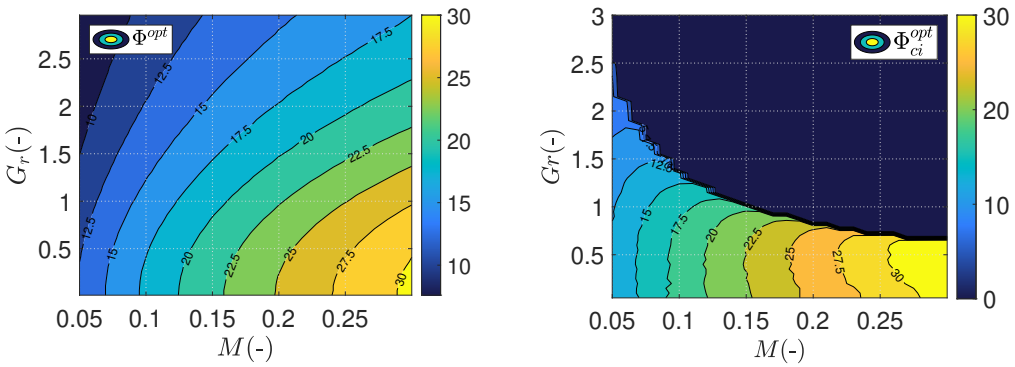


(a) *Makani Model: optimal opening angle as a function of $G_r$ and $M$ for $\beta = 30°$*

(b) *CiMo-FG-KiTe: optimal opening angle as a function of $G_r$ and $M$ for $\beta = 30°$*

Figure 4.12: Comparison between the optimal opening angle trends in the case of Makani Model and CiMo-FG-KiTe as a function of $M$ and $G_r$ for $\beta = 30°$

Summarizing, adding elevation makes the results of the two models even more different for two reasons:

1. As far as the Makani Model is concerned, the elevation increases performance because power losses due to gravity are reduced.
2. As for the CiMo-FG-KiTe, elevation reduces performance because power losses due to a non-perfectly crosswind trajectory are introduced (see Section 3.3.2).

## Numerical examples

In this part of the work, a numerical example shows the different results obtained using the two models. Two cases at $\beta = 30°$ with different influence of gravity are analyzed and compared in the same time. Only one parameter is modified: the wind speed is changed from 10 $m/s$ (case C) to 7.5 $m/s$ (case D). The values of $M$ and $G_r$ for these two cases are those reported in Table 3.9: $G_r = 0.88$ and $G_r = 1.57$ for case C and case D respectively and $M = 0.13$.

Figure 4.13 compares system performance obtained with the two models as a function of $M$ and $\Phi$. With the addition of elevation, even in the case of a slight influence of gravitational acceleration (case C), the trends start to be quite different. In particular, the no-fly zone predicted with the CiMo-FG-KiTe is much larger. In case B, the models provide even more different results. The CiMo-FG-KiTe estimates that no power can be generated for almost all conditions while the efficiency trend obtained with the Makani

Model is much smoother.

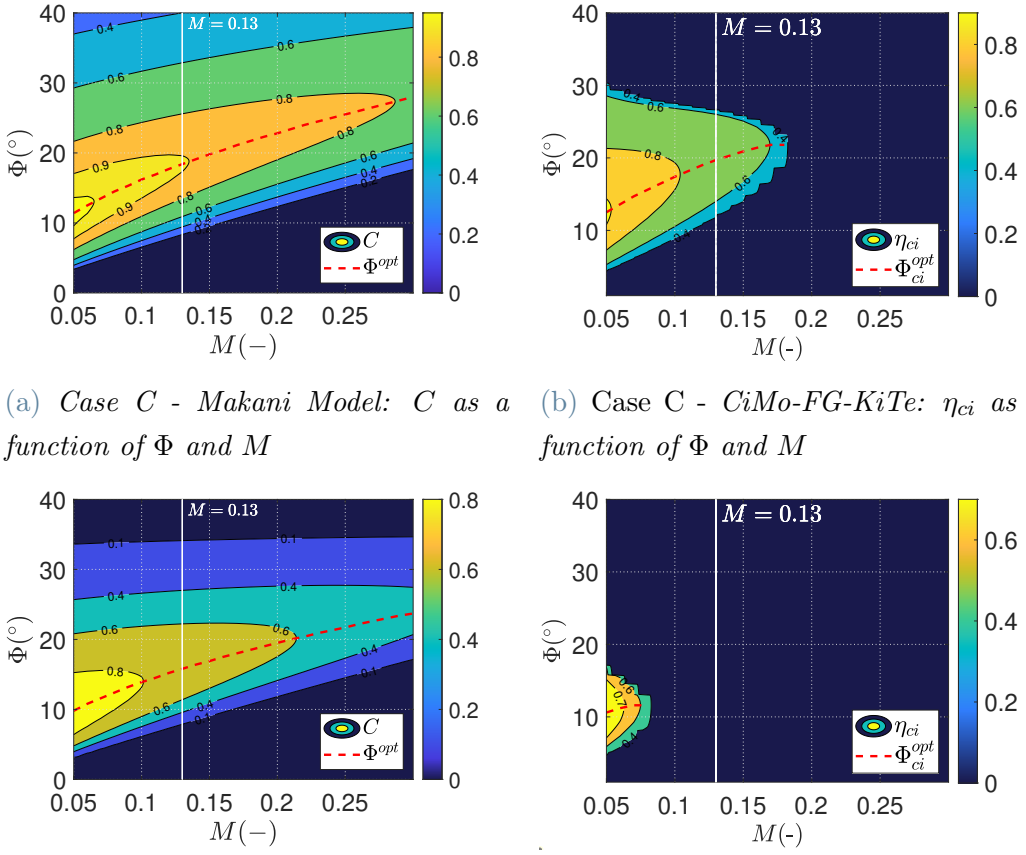


(a) *Case C - Makani Model: C as a function of* $\Phi$ *and* $M$

(b) Case C - *CiMo-FG-KiTe:* $\eta_{ci}$ *as a function of* $\Phi$ *and* $M$

(c) *Case D - Makani Model: C as a function of* $\Phi$ *and* $M$

(d) Case D - *CiMo-FG-KiTe:* $\eta_{ci}$ *as a function of* $\Phi$ *and* $M$

Figure 4.13: Comparison of system performance for cases C and D as a function of $M$ and $\Phi$ obtained with Makani Model and CiMo-FG-KiTe

Focusing on the optimal conditions, Figure 4.14 compares the trends of the optimal opening angle as a function of $M$. Again, the difference due to the no-fly zone is evident. Moreover, in case A, the CiMo-FG-KiTe provides a higher optimal opening angle because it accounts the physical effects of the elevation on the power losses (see Section 3.5.2).

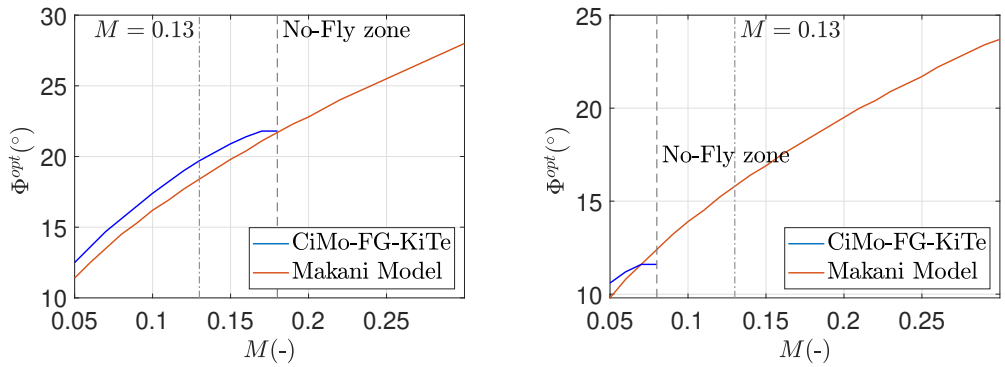


(a) *Case C* (b) *Case D*

Figure 4.14: Comparison between the trends of the optimal opening angles provided by the two models for cases C and D as a function of $M$

The numerical results for the calculated values of $M$ and $G_r$ are present in Table 4.4. The numbers confirm what was previously presented. The presence of elevation, makes the two models differ significantly in both cases. Regarding case C, even if $G_r$ is limited, the elevation causes almost 20 % difference in power generation estimation. For case D, with Makani Model power can be generated while with CiMo-FG-KiTe the kite cannot fly.

| Case | $V_w$ $[m/s]$ | $\beta$ [°] | $M$ [-] | $G_r$ [-] | CiMo-FG-KiTe | | Makani Model | |
|---|---|---|---|---|---|---|---|---|
| | | | | | $\Phi_{ci}^{opt}$ [°] | $\eta_{ci}^{max}$ [%] | $\Phi^{opt}$ [°] | $C^{max}$ [%] |
| C | 10 | 30 | 0.13 | 0.88 | 20.0 | 73.3 | 18.7 | 90.1 |
| D | 7.5 | 30 | 0.13 | 1.57 | - | - | 16.0 | 74.0 |

Table 4.4: Results for case C and case D in the optimal conditions

## 4.3. Critical perspective of Makani proposal

In this section, critical comments on Makani Model are provided downstream the results of the comparison.

The first difference of Makani Model is the decoupling of the various power losses contributions. Some physical aspect is inevitably lost because in Chapter 3 is demonstrated that the coupling between elevation and gravity is not linear and so the superposition principle is not valid.

As for the phenomenon linked to the centrifugal effects, Makani's team makes two additional hypotheses (ix) (small opening angle $\Phi$) and (x) (small roll angle $\phi$). Despite the

CiMo-FG-KiTe remains more general avoiding them, these approximations are not too impactful. Indeed, for the typical $M$ values coming from the state of the art, the opening angle remains limited to $20 \div 25°$. Up to these values the assumption on the small opening angle does not affect significantly the results. Similar conclusions can be drawn for the assumption related to the roll angle.

On the other hand, the assumptions for modelling the effect of gravity affect results in a greater way. Firstly, it is assumed that all the kite acceleration is given by the weight force while the other forces are in equilibrium (assumption (v)). Secondly, the average kite speed is weighted on the loop angle rather than the time (hypothesis (iv)). In particular, it is demonstrated that assumption (v) is the most impactful making the results of the two models very different. Moreover, where they are similar, it is not because the two hypotheses are more valid but because the phenomenon to be modeled is not very influential.

Furthermore, the decoupling of the losses does not take into account the physical effect that the elevation has on system performance. Indeed, the results considering also the elevation turn out to be very different.

The main advantage of Makani Model is its simplicity and its being completely analytical. The effort for obtaining the results is extremely small. However, the methodology and the additional assumptions make it less general. In the case elevation is not considered, the results partially match, under certain values of $M$ and $G_r$, those predicted with the CiMo-FG-KiTe. However, the no-fly region is not individuated because the assumptions start to be too strong for high values of $M$ and $G_r$. On the contrary, if elevation is considered, the modeling of Makani is less representative of physics because the coupling between the effects of gravity and elevation is not caught.

## 4.4. Summary and contributions

In this chapter, the model proposed by Makani's team for a FG-AWES flying a circular path is presented and compared with the CiMo-FG-KiTe.

Initially, in Section 4.1, the Makani proposal is presented and derived, focusing on the further assumptions needed for the model derivation. The effects of the centrifugal force, elevation and gravity are investigated.

In Section 4.2, a comparison between the Makani proposal and the CiMo-FG-KiTe is performed by steps. Firstly, the results are compared in the case elevation is not considered. The focus is on how the gravity has been modelled. The assumption made by Makani's

team for which all the kite acceleration is due to the weight force, while the other forces are constantly in equilibrium, turns out to be too strong above certain values of $M$ and $G_r$. Secondly, the results are compared in the case also elevation is considered. In this conditions, the results differ in a significant way because Makani Model does not catch the penalizing effects due to the coupling between gravity and elevation.

Finally, a critical perspective of the Makani Model is introduced in Section 4.3. It is highlighted that Makani Model is more simple but is less representative of physics for conditions in which gravity starts to have a relevant influence.

This chapter helps to understand how the model introduced by this thesis contributes to a greater comprehension of the phenomena related to the presence of gravity and elevation. The comparison presented in this chapter highlights that a further progress is made in the physics modeling through a low-fidelity model such as the CiMo-FG-KiTe (and so the GeMo-KiTe). With this purpose, comparisons with other models in the literature are suggested together with validations through high-fidelity simulations or experiments.

# 5 | Performance enhancement through non-circular trajectories

In this chapter of the thesis, a possible solution to reduce the inefficiency related to gravity is presented. The discussion is intended to be qualitative. The goal is only to provide a hint of what may be the right approach for performance enhancement exploiting the quasi-analytical model proposed in the thesis. The latter is used to analyse the effects of a new trajectory on system performance. In particular, the effects of the elliptical path in a FG-AWES are investigated.

A subscript *ell* will be present in the parameters that refer to the elliptical trajectory.

Section 5.1 is devoted to the explanation of the new trajectory and the motivations behind its choice.

The chapter is divided into four sections. In Section 5.2, the Elliptical Model for Fly Generation Tethered Kites (ElMo-FG-KiTe) is derived from the GeMo-KiTe. In Section 5.3, the model results are shown in the form of numerical examples. Firstly, they are presented with a null elevation, then, a mean elevation angle of 30° is considered. Finally, in Section 5.4, further qualitative comments on the obtained results and on the potential of what has been presented are provided.

## 5.1. Motivations

The results of Chapter 3 highlight the degrading effects of gravity on the performance of an AWES. In particular, as understood from the discussion about the power losses, the roll angle and the kite speed fluctuation are the main causes of efficiency degradation. A possible approach to reduce the roll angle effects is proposed to enhance performance.

In the quasi-analytical model proposed in this thesis, the system components considered are just the kite and the tether besides the wind speed. The latter is obviously a param-

eter on which it is impossible to act. On the other hand, the kite's attitude is already determined to maximize performances. Therefore, the idea is to actively use the tether to raise the efficiency of the system.

From Figure 3.18 (a), a lower radial tether traction, in the most impactful top part of the loop, can reduce the roll angle. On the contrary, in the bottom part, the radial tether traction should be higher to reduce the kite roll angle. In order to make the tether acts in this way, an elliptical trajectory is prescribed.

Starting from the circular trajectory, the new elliptical path is defined as in Figure 5.1. $x$, $r$ and $\alpha$ is the triad that defines the cylindrical reference system, the same adopted for the GeMo-KiTe. $F_1$ and $F_2$ are the foci of the ellipse, $a$ and $b$ are the major and minor axes respectively, $r$ is the path radius variable with the loop angle $\alpha$. The focus $F_1$ coincides with the center of the circular trajectory. Moreover, the elevation angle $\beta$ is referred to the focus $F_1$ and so it represents the mean elevation of the 'initial' circular path. The effective mean elevation angle of the elliptical orbit is called $\tilde{\beta}$ and will be defined in the following.
Since the tether length is constant and the kite does not fly on a circumference, the motion no longer lies on a plane but is three-dimensional. Therefore, what is actually prescribed is the projection of the 3D trajectory on the rotor plane where the 'initial' circular path lies. For readability, both 3D trajectory or elliptical path are used to refer to as the new orbit.

As visible from Figure 5.1, in the upper part of the loop the tether is less inclined than in the circular case and the radial tether traction is lower. The opposite happens in the bottom part of the loop. This way the cable is used to partially compensate for gravity by decreasing the roll angle of the kite during the loop.

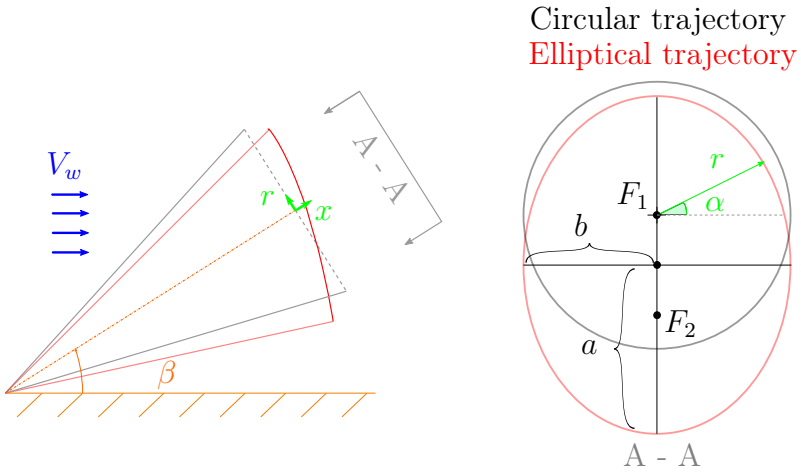


Figure 5.1: Definition of the elliptical trajectory starting from the circular one

To generalize the problem, the influence of a $\gamma$ angle is added as shown in Figure 5.2. $\gamma$ is defined as the angle between the ellipse's major axis and the vertical direction and it is positive counterclockwise. It represents the inclination of the elliptical path with respect to the vertical direction. In the following, it will be referred to as the orbital angle.

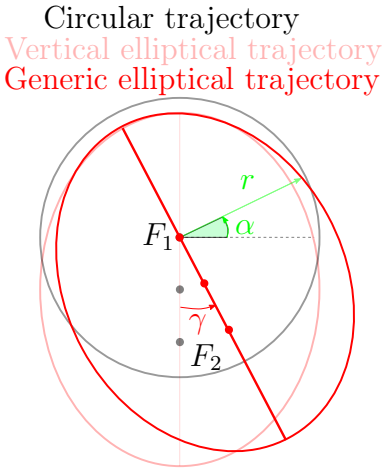


Figure 5.2: Generic elliptical path and definition of the orbital angle $\gamma$

The motivations behind the introduction of $\gamma$ are driven by the power losses due to elevation. As shown in Figure 3.11 (b), the descending part of the loop is characterized by a higher roll angle. Higher radial tether traction in this part of the motion can contribute to its reduction. Therefore, during the descending phase a higher tether inclination (i.e. higher radius) is desired in terms of elevation power losses. The opposite is true for the ascending phase.
Consequently, a 'horizontal' ellipse is promising to reduce power losses due to elevation. However, this trajectory contrasts with the promising 'vertical' ellipse in terms of gravity. Hence the need for the introduction of the $\gamma$ angle.

## 5.2. Derivation of the ElMo-FG-KiTe

In this first section, the model representing a FG-AWES flying a crosswind elliptical trajectory is derived starting from the GeMo-KiTe.

Assumptions (ix), (x) and (xi) are valid if the ellipse is not very accentuated. Therefore, only ellipses with small eccentricity are considered.

The steps needed to derive the ElMo-FG-KiTe from the GeMo-KiTe are:

1. Elliptical trajectory prescription.

2. Setting $\gamma_{out} = 0$ because in pure FG-AWES the reel-out velocity is null.

The first step for the model derivation is to prescribe the elliptical trajectory. Knowing that the eccentricity of the ellipse is defined as:

$$e = \sqrt{1 - \frac{b^2}{a^2}} \tag{5.1}$$

the classic equation of the ellipse in cartesian coordinates can be rewritten in polar coordinates relative to a focus as [70],:

$$r(\alpha) = \frac{a(1-e^2)}{1 - e\cos(\alpha + \pi/2)}$$

With reference to Figure 5.2, introducing the generalization determining by $\gamma$:

$$r(\alpha) = \frac{a(1-e^2)}{1 - e\cos(\alpha - \gamma + \frac{\pi}{2})} = \frac{a(1-e^2)}{1 + e\sin(\alpha - \gamma)} \tag{5.2}$$

Making the derivative with respect to time, the radial speed is:

$$\dot{r}(\alpha) = -ea(1-e^2) \cdot \frac{\dot{\alpha}\cos(\alpha - \gamma)}{\left[1 + e\sin(\alpha - \gamma)\right]^2} \tag{5.3}$$

Then, repeating the time derivative, the radial acceleration is:

$$\ddot{r}(\alpha) = -ea(1-e^2)\left[\frac{\ddot{\alpha}\cos(\alpha - \gamma) - \dot{\alpha}^2\sin(\alpha - \gamma)}{\left[1 + e\sin(\alpha - \gamma)\right]^2} - \frac{2e\dot{\alpha}^2\cos(\alpha - \gamma)^2}{\left[1 + e\sin(\alpha - \gamma)\right]^3}\right] \tag{5.4}$$

Since the trajectory is a three dimensional curve, an axial motion is present. With reference to Equation 2.12 and knowing that $\gamma_{out} = 0$, the axial position of the kite is identified only by the axial displacement with null reel-out $\Delta x$. Being $\Phi_{ci}$ the opening angle in case of circular trajectory (i.e, constant during the motion) with elevation $\beta$, the axial displacement in the case of no reel-out is:

$$\Delta x = l_t \cos\left(\arcsin\left(\frac{r}{l_t}\right)\right) - l_t \cos\Phi_{ci} \tag{5.5}$$

Then, by exploiting the identity $\cos\Big(\arcsin(y)\Big) = \sqrt{1-y^2}$ and being $\gamma_{out} = 0$, from

Equation 2.12, the axial kite coordinate can be rewritten as:

$$x = l_t \sqrt{1 - \frac{r^2}{l_t^2}} - l_t \cos \Phi_{ci} \tag{5.6}$$

Making the time derivative, the kite axial speed is found:

$$\dot{x} = -\frac{r \cdot \dot{r}}{\sqrt{l_t^2 - r^2}} \tag{5.7}$$

Making the time derivative a second time, the kite axial acceleration is:

$$\ddot{x} = -\frac{\dot{r}^2 + r \cdot \ddot{r}}{\sqrt{l_t^2 - r^2}} - \frac{r^2 \cdot \dot{r}^2}{\sqrt{(l_t^2 - r^2)^3}} \tag{5.8}$$

Equations 5.2 and 5.6 are substituted into Equation 2.12. Equations 5.3 and 5.7 are substituted into Equation 2.13. Equations 5.4 and 5.8 are substituted into Equation 2.14. In this way, the elliptical path is prescribed.

After the trajectory prescription, the model derivation and equations are the same of the ones present in Section 2.4. Therefore, Equations 2.17 to 2.30 remain the same.

The instantaneous power of a FG-AWES flying a crosswind elliptical trajectory with the reference system centered in one focus is:

$$P_{ell} = \frac{1}{2} \rho A \gamma_t C_D (\dot{\alpha} r K_2)^3 \tag{5.9}$$

For the efficiency derivation, an important premise must be done. As visible from Figure 5.2, the center of the ellipse does not correspond to the one of the circumference. Therefore, the new elliptical trajectory has a different mean elevation with respect to the circular path from which it is derived. Moreover, for the generalization introduced with $\gamma$, the centered of the trajectory is not perfectly downwind anymore but a certain mean azimuth angle with respect to the ground station will be present. Knowing that the distance between the focus and the center of the ellipse is given by $e \cdot a$, the mean azimuth angle is given by $\arctan\left(\frac{e\ a \sin\gamma}{l_t \cos \Phi_{ci}}\right)$ while the mean elevation angle of the ellipse, $\tilde{\beta}$, is defined as:

$$\tilde{\beta} = \beta - \arctan\left(\frac{e\ a \cos\gamma}{l_t \cos \Phi_{ci}}\right) \tag{5.10}$$

For this reasons, the efficiency is defined as the ratio between the generated power flying the elliptical trajectory and the ideal generated power flying at the same mean elevation $\tilde{\beta}$:

$$\eta_{ell} = \frac{1}{T_{loop}} \int_0^{T_{loop}} \left( \frac{\dot{\alpha} r K_2}{V_w E_t \cos \tilde{\beta}} \right)^3 \cdot dt = \overline{\left( \frac{\dot{\alpha} r K_2}{V_w E_t \cos \tilde{\beta}} \right)^3} \tag{5.11}$$

## 5.3. Model results

In this section, the results of the ElMo-FG-KiTe are presented.

Since the chapter aims only to provide a qualitative discussion about the elliptical trajectory, the results are directly shown through the same examples of Chapter 3 but in the case of an elliptical path. In this way, a direct comparison can be done. Firstly, the results are shown with null elevation, then, a mean elevation angle of 30° is considered. The generalization of the results as a function of non-dimensional parameters ($M$ and $G_r$) will be discussed in future works.

The results will show the efficiency obtained with the elliptical trajectory as defined in Equation 5.11. To understand if the elliptical orbit is promising, it must be compared with the optimal circular path at the same mean elevation $\tilde{\beta}$. The chronological steps to derived the right comparison are the following:

1. Firstly, the mean elevation $\beta$ is set and the efficiency of the optimal circular trajectory is found (same procedure done for the examples in Chapter 3).
2. Starting from this optimal path, the elliptical orbit is prescribed. The minor axis is set equal to the optimal radius of the circular path: $b = l_t \sin \Phi_{ci}^{opt}$. The eccentricity is set small to satisfy assumptions (x), (ix) and (xi): $e = 0.1$. The orbital angle $\gamma$ is varied to find its optimal value for which the efficiency of the system is maximized. Then, the mean elevation angle of the ellipse $\tilde{\beta}$ at $\gamma^{opt}$ is found with Equation 5.10.
3. Finally, the efficiency of the optimal circular path having the mean elevation $\tilde{\beta}$ is calculated. To distinguished this efficiency, it will be referred to as $\tilde{\eta}_{ci}$ with the tilde symbolizing it is related to the elevation $\tilde{\beta}$. More in general, the tilde symbolizes that the considered parameter is referred to the circular path at the mean elevation $\tilde{\beta}$ of the ellipse.

The effects of the new trajectory on system performance can be decoupled into two different ones. Firstly, the change in the mean elevation and, secondly, the non-circular

path itself. For clarity, the last effect will be called orbital effect. To isolate only the orbital effect, the reference parameter $\Delta\eta = \eta_{ell} - \tilde{\eta}_{ci}$ is defined. It will inform about the convenience of the elliptical path.

For a better understanding of the results, it is important to establish what are the consequences of the orbital effect on power losses. As explained in Section 5.1, the tether is actively used through the ellipse to reduce roll angle and related power losses. On the other hand, the path is more developed vertically, increasing the kite speed variation in the loop and the related power losses. Consequently, the elliptical path will be convenient when the roll angle power losses overcomes those for speed variation.

In the following, the results are obtained downstream a simulation performed with a time-marching code in *MATLAB*. A time step is set together with the input aerodynamic values and the initial conditions (angular position, kite speed, kite acceleration). Then, the input needed for the elliptical trajectory (eccentricity $e$ and minor axis $b$) are introduced.
For each time step, the path is prescribed through the implementation of Equations 5.2, 5.3, 5.4 representing the radial motion, Equation 2.15 determining the opening angle and Equations 5.6, 5.7 and 5.8 related to the axial motion. After that, Equations 2.29, 2.28, 2.24, 2.23 and 2.30 are implemented. As before, each instant of time has the results of the previous one as input, simulating time integration.
The consistency and reliability of the time-marching code is proved for various time steps: $\Delta t = 10^{-1}\ s$, $\Delta t = 10^{-2}\ s$, $\Delta t = 10^{-3}\ s$ and $\Delta t = 10^{-4}\ s$. The results converge from $\Delta t = 10^{-2}\ s$ onwards. Therefore, the latter time step is implemented for all the simulations performed. Downstream the simulations, a final check on the hypotheses (viii), (ix), (x) and (xi) is done.

The numbers that will be shown are not meaningful from the engineering point of view. However, on the physical side, they are. Indeed, the focus is on the message they carry. Again, the approach is qualitative with the aim of proposing a hint on which could be the right speculations to focus on.

### 5.3.1. Model results without elevation

In this subsection, the results of the ElMo-FG-KiTe with a null $\beta$ are shown. Case A and B of Section 3.6 are re-evaluated here in the case of the three-dimensional orbit.

Since a starting circumference with $\beta = 0°$ is used, from Equation 5.10, the 3D trajectory will have negative mean elevation angle $\tilde{\beta} < 0°$.

$\gamma^{opt}$ will be the results of several effects, summarized in the following and divided according

to the type of power loss they affect.

**Roll angle** As explained in Section 5.1, the more vertical is the ellipse, the more efficiently the tether is used to reduce the roll angle caused by gravity presence. Consequently, closer to 0° is $\gamma$, the better it is. As for the negative mean elevation, contrary to what is shown in Figure 3.11 (b), higher radial tether traction can contribute to roll angle reduction during the ascending motion. A higher radius is desired in this part of the loop. The opposite is true for the descending phase. Consequently, a 'horizontal' ellipse towards $\gamma = +90°$ is promising to reduce roll angle power losses. As a conclusion, in terms of kite roll angle, the optimal value will be in between 0° and 90°.

**Speed fluctuation** As explained in Section 3.3.2, higher is the vertical range of the path, higher is the kite speed fluctuation due to both gravity and elevation. However, the negative mean elevation causes a speed fluctuation inverse to that caused by gravity (see Section 3.3.2). Therefore, in terms of speed fluctuation, the optimal value will be that for which the two contributions will tend to balance more.

The inputs are the same of Table 3.8 and the necessary additional parameters are reported in Table 5.1. In Table 5.1 are also present the values of $M$ and $G_r$.

| Case | $V_w$ $[m/s]$ | $\beta$ [°] | $M$ [-] | $G_r$ [-] | $e$ [-] | $\Phi_{ci,g}^{opt}$ |
|---|---|---|---|---|---|---|
| A | 10 | 0 | 0.13 | 0.66 | 0.1 | 18.9 |
| B | 7.5 | 0 | 0.13 | 1.18 | 0.1 | 15.5 |

Table 5.1: Inputs parameters for the elliptical trajectory for cases A and B in addition to those reported in Table 3.8

Performing the simulations, the optimal elliptical paths for the two mentioned cases are shown in Figure 5.3 with their geometric values. As expected by the trade-off previously explained, the best performance is obtained for a positive value of $\gamma$.

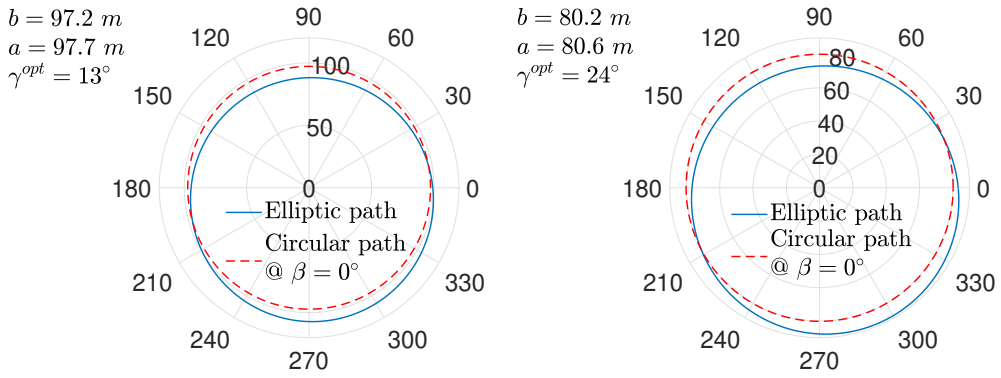


(a) *Case A* (b) *Case B*

Figure 5.3: Elliptical projection in the rotor plane of the 3D path for cases A and B

Finally, the numerical results are shown in Table 5.2. It seems to be counter intuitive, but in both cases, $\tilde{\eta}_{ci,g}^{max} > \eta_{ci,g}^{max}$. If gravity is considered, the highest efficiency of a circular path is not for null elevation. Indeed, the small negative elevation is beneficial because contrasts the gravitational effects. Moreover, $\eta_{ell,g}^{max} > \eta_{ci,g}^{max}$ meaning that the combination of lower mean elevation and orbital effect results to be beneficial.

Comparing $\eta_{ell,g}^{max}$ with $\tilde{\eta}_{ci,g}^{max}$, the effective gain due to orbital effect in case A is:

$$\Delta\eta = -0.1\%$$

while the effective gain due to orbital effect in case B is:

$$\Delta\eta = +0.6\%$$

For low $G_r$, the shift towards an ellipse is not convenient. Low $G_r$ means wide path and the power losses related to the kite speed variation are relatively more relevant than those due to roll angle. Therefore, the benefit brought by the ellipse from the roll angle side are overcome by the relatively higher power losses for kite speed variation. The opposite is true for the higher $G_r$. Higher is $G_r$, narrower is the path. Consequently, the power losses related to the roll angle are relatively higher than those for speed variation. Therefore, the benefits brought by the new orbit in terms of roll angle outweigh the disadvantages of a greater exchange of potential energy. The result is a positive orbital effect and performance increase.

| Case | Optimal circular path @ $\beta$ | | | Optimal ellipse | | | Optimal circular path @ $\tilde{\beta}$ | | |
|---|---|---|---|---|---|---|---|---|---|
| | $\beta$ [°] | $\Phi_{ci,g}^{opt}$ [°] | $\eta_{ci,g}^{max}$ [-] | $\tilde{\beta}$ [°] | $\gamma_g^{opt}$ [°] | $\eta_{ell,g}^{max}$ [%] | $\tilde{\beta}$ [°] | $\tilde{\Phi}_{ci,g}^{opt}$ [°] | $\tilde{\eta}_{ci,g}^{max}$ [%] |
| A | 0 | 18.9 | 92.0 | -1.9 | 13 | 92.6 | -1.9 | 19.0 | 92.7 |
| B | 0 | 15.5 | 69.7 | -1.5 | 24 | 72.0 | -1.5 | 15.5 | 71.4 |

Table 5.2: Results for case A and B in the optimal conditions related to the elliptical orbit

### 5.3.2. Model results with elevation

In this subsection, the results of the ElMo-FG-KiTe with the $\beta = 30°$ are shown. Case C and D of Section 3.6 are re-evaluated here in the case of the three-dimensional orbit.

Since a starting circumference with positive elevation is used, the 3D trajectory will have a positive elevation $\tilde{\beta}$ found with Equation 5.10.

As before, $\gamma^{opt}$ will be the results of several effects, summarized in the following and divided according to the type of power loss they affect.

**Roll angle** As previously explained, closer to 0° is $\gamma$, higher is the reduction of the roll angle due to gravity thanks to the tether exploitation. On the other hand, as explained in Section 5.1, a horizontal ellipse towards $\gamma = -90°$ is promising to reduce roll angle due to elevation. From this point of view, the optimal value will be in between 0° and −90°.

**Speed fluctuation** As explained in Section 3.3.2, in case of positive $\beta$, the elevation causes a speed fluctuation concordant to that caused by gravity. Therefore, closer to ±90° is $\gamma$, lower is the vertical range, the associated potential energy exchange and lower are the power losses.

The inputs are the same of Table 3.8 and the necessary additional parameters are reported in Table 5.3. In Table 5.3 are also present the values of $M$ and $G_r$.

| Case | $V_w$ $[m/s]$ | $\beta$ [°] | $M$ [-] | $G_r$ [-] | $e$ [-] | $\Phi_{ci}^{opt}$ |
|---|---|---|---|---|---|---|
| C | 10 | 30 | 0.13 | 0.88 | 0.1 | 20.0 |
| D | 7.5 | 30 | 0.13 | 1.57 | 0.1 | - |

Table 5.3: Inputs parameters for the elliptical trajectory for cases C and D in addition to those reported in Table 3.8

In the conditions of case D the kite is unable to fly in any circular trajectory for $\beta = 30°$.

Therefore, the minor axis of the ellipse, $b$, is varied to find a value for which the kite can fly in the elliptical orbit. The simulation provides a negative feedback: the kite cannot fly even if the elliptical path is prescribed. On the other hand, the optimal elliptical path for case C is shown in Figure 5.4 with its geometric values. As expected by the trade-off previously explained, the best performance is obtained for a negative value of $\gamma$.

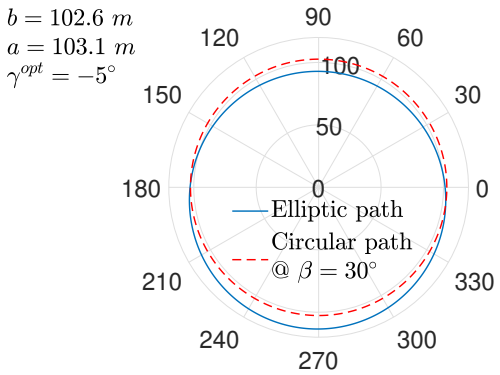


Figure 5.4: Case C: elliptical projection in the rotor plane of the 3D path

Finally, the results are shown in Table 5.4. $\tilde{\eta}_{ci}^{max} > \eta_{ci}^{max}$ because of the lower mean elevation. Again, $\eta_{ell}^{max} > \eta_{ci}^{max}$ meaning that the combination of lower mean elevation and orbital effect results to be beneficial.

Comparing $\eta_{ell}^{max}$ with $\tilde{\eta}_{ci}^{max}$, the effective gain due to orbital effect in case C is:

$$\Delta\eta = +0.3\%$$

This value of $G_r$ justifies again the shift towards an ellipse. As the $G_r$ value is between the two of the above examples, $\Delta\eta$ is too. Therefore, the advantages brought by the ellipse in terms of the roll angle overcome again the drawbacks in terms of higher kite speed variation and performance increases.

| Case | Optimal circular path @ $\beta$ | | | Optimal ellipse | | | Optimal circular path @ $\tilde{\beta}$ | | |
|---|---|---|---|---|---|---|---|---|---|
| | $\beta$ [°] | $\Phi_{ci}^{opt}$ [°] | $\eta_{ci}^{max}$ [-] | $\tilde{\beta}$ [°] | $\gamma^{opt}$ [°] | $\eta_{ell}^{max}$ [%] | $\tilde{\beta}$ [°] | $\tilde{\Phi}_{ci}^{opt}$ [°] | $\tilde{\eta}_{ci}^{max}$ [%] |
| C | 30 | 20.0 | 73.3 | 27.9 | -5 | 76.1 | 27.9 | 19.9 | 75.8 |
| D | 30 | - | - | - | - | - | - | - | - |

Table 5.4: Results for case C and D in the optimal conditions related to the elliptical orbit

## 5.4. Qualitative considerations and proposals

The goal of this section is to discuss the conclusions that can be drawn from the results presented in Section 5.3. What will be treated has no general validity but has only the purpose of promoting future reasoning to reach more general conclusions.

The results show that the efficiency of the system flying the elliptical trajectory is always higher than the one obtained with the circular path from which it is derived ($\eta_{ell} > \eta_{ci}$). Therefore, even if the orbital effect is negative, it is always overcome by the benefits due to the lower mean elevation.

What effectively informs about the convenience of the new path is the comparison with the efficiency of the optimal circular path at the same elevation ($\tilde{\eta}_{ci}$). The results show that the higher the $G_r$, the higher the efficiency gain with the elliptical path. This happens because, higher is $G_r$, narrower is the path. Consequently, power losses for kite speed variation become relatively less relevant than those for roll angle and the active action of the tether is beneficial.

These considerations and these results must be validated and generalized because are obtained only for certain conditions and specific eccentricity. Indeed, in addition to the conditions represented by the non-dimensional parameters, the values that can be varied are $e$, $b$ and $\gamma$.

Another similar methodology is to parameterize $\Delta x$, instead of the radius, as a function of $\alpha$. Then, the radius can be derived with Equation 5.5. In this way, the orbit prescription occurs along the axial direction.

Despite its specificity, the discussion presented in this chapter may be essential for further research and future works. Others trajectories and their effects on power losses can be easily investigated. As an example, a new path as described in Figure 5.5 can be promising. The potential energy exchange in the loop and the kite speed variation are likely to be lower than in the path proposed in this chapter. On the contrary, only the upper part of the loop contributes to reducing the roll angle while the bottom provides a further increase of it.

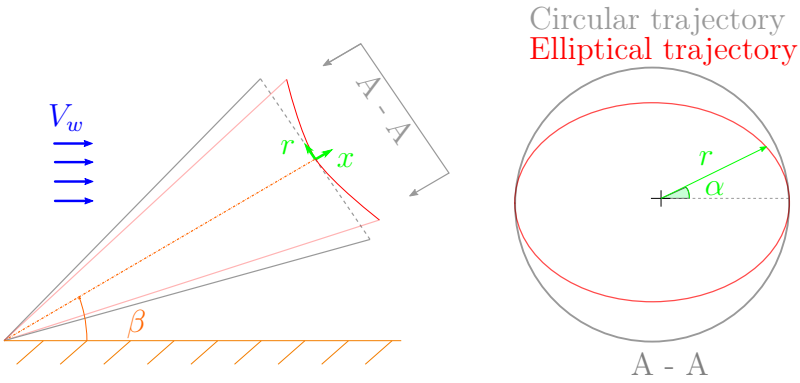


Figure 5.5: 3D path where the parameterization is a centered ellipse

Another example is provided in Figure 5.6. This path is parameterized with half ellipse and half circumference. Unlike the previous one, the benefit in terms of kite speed variation are lower but no drawback are present for the kite roll angle in the bottom part. For non-symmetrical orbits like this, attention must be paid to calculating the mean elevation angle.

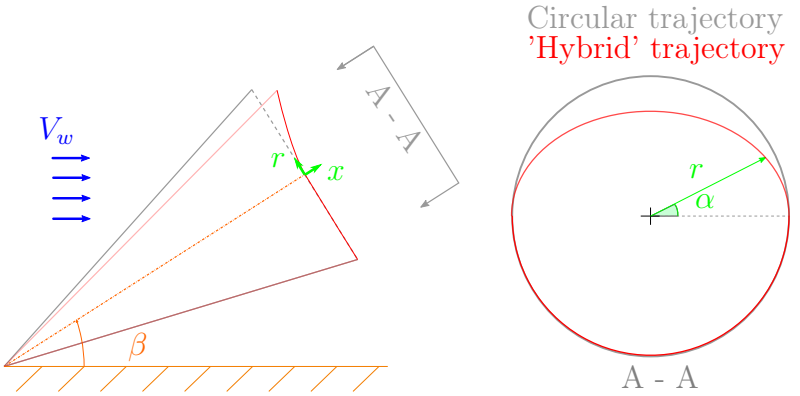


Figure 5.6: 3D path where the upper half of the trajectory is parameterized with an ellipse and the bottom with a circumference

Intuitively, there may not be a better trajectory among those shown. Indeed, the best path may depend on the conditions (i.e. on the pair of $M$ and $G_r$). More generally, future work is recommended on the generalization of the path with respect to circular trajectory. According to one methodology or the other, for each value of the loop angle, it is possible to optimize the displacement $\Delta r$ or $\Delta x$ from the circular path. The resulting generic optimal orbit could be something similar to what is reported in Figure 5.7.

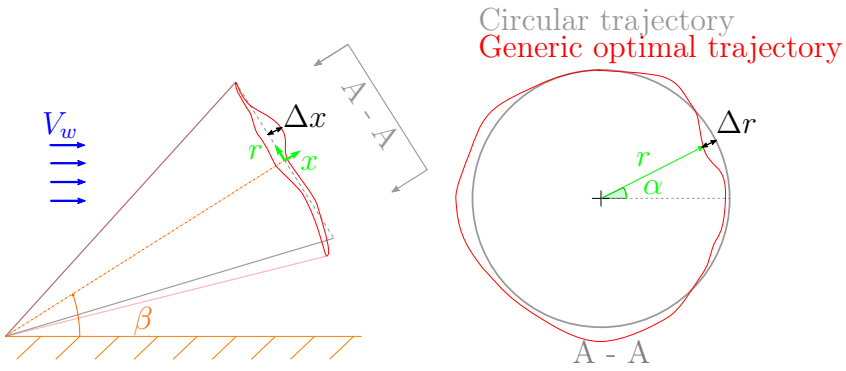


Figure 5.7: Theoretical 3D generic optimal trajectory obtainable through an optimization algorithm with respect to the circular path

## 5.5. Summary and contributions

In this chapter, a physical model of a generic crosswind AWES flying an elliptical path which takes into account centrifugal, elevation and gravity effects is presented.

Initially, Section 5.1 is devoted to a deep explanation behind the choice of the ellipse as a trajectory parameterization. The new path is defined and generalized as a function of the angle representing the inclination of the ellipse with respect to the vertical direction.

In Section 5.2, the model derivation is performed, focusing on the trajectory prescription and definition of the right efficiency. The power should be referred to the ideal power generated at the same mean elevation of the ellipse.

Then, in Section 5.3, the model results are shown exploiting examples. Moreover, it is explained how the elliptical path affects power losses. It is beneficial in terms of power losses due to roll angle but it is disadvantageous for power losses due to kite speed variation. In particular, the example with $\beta = 0°$, $G_r = 0.66$ and $M = 0.13$ shows that the ellipse is not convenient. The example with $\beta = 0°$, $G_r = 1.18$ and $M = 0.13$ and the example with $\beta = 30°$, $G_r = 0.88$ and $M = 0.13$ show that the ellipse is convenient. Finally, the example with $\beta = 30°$, $G_r = 1.57$ and $M = 0.13$ shows that even with the ellipse the kite cannot fly.

Finally, in Section 5.4 qualitative conclusions are drawn from the previous examples. In particular, higher is $G_r$, more the power losses due to roll angle becomes relatively higher than those for speed variation. Therefore, higher is $G_r$, higher is the efficiency gain thanks to the ellipse. Moreover, it is highlighted how the introduced approach can be useful for further research and promising non-circular trajectories are proposed.

The physical considerations discussed in this chapter can be helpful to the AWES research

community. Indeed, to the author's best knowledge, no literature sources show proposals to reduce the effects of gravity exploiting different flight paths. Particularly innovative is the simple, quasi-analytical but still physical approach that conducts to the above-mentioned considerations. They can be the starting points for future analyzes and further understandings of AWESs physics.

# 6 | Future developments

The open problems and questions raised within this work are several. The following list provides examples of possibles future research:

- The straightforward future work is to find an equation, through a fitting technique, of the maximum efficiency and optimal opening angle as a function of $\beta$, $M$ and $G_r$. In this way, the theory is even more generalized.
- Another straightforward future work is to improve the analysis made on the ellipse through the generalization as a function of dimensionless parameters.
- In the thesis, a comparison with the simple analytical model proposed by Makani's team is presented. In addition, it could be interesting to compare the GeMo-KiTe with other low-fidelity models present in the literature.
- It could be interesting to use the methodology presented in Chapter 5 to study the effects of new trajectories on system performance. For instance, two interesting paths could be those proposed in Section 5.4.
- It could be interesting to generalize the discussion without prescribing the path. The right approach could be to find the radial (or axial) deviation from the circumference that maximizes the power production as a function of the loop angle exploiting an optimization algorithm.
- It could be interesting to include in the model the wind speed variation with altitude. Intuitively, the wind shear might opposes to power losses due to gravity. Indeed, when the kite is flying upwards (and so decelerating), the increased in the wind speed is beneficial. In the same way, when the kite is flying downwards (and so accelerating), the wind speed decreases. The kite speed fluctuation and the related power losses might be reduced.
- It could be interesting to evaluate how the on-board turbines' drag variation affects the gravity power losses and so performance. The idea is to reduce drag during the upwards motion and increase it during the downwards motion to decrease the kite

speed variation. The optimal trend of $C_{D,t}$ during the loop could be evaluated as a function of the non dimensional parameters $M$ and $G_r$.

- More in general, the presented model can be the starting point for any study related to the physical effect on power generation of a phenomenon present in the AWESs.

# 7 | Conclusions

In this thesis, the main physical phenomena characteristic of Airborne Wind Energy Systems (AWESs) are analyzed through the use of a new quasi-analytical model related to power generation.

In Chapter 2, the derivation of a quasi-analytical model (GeMo-KiTe) for a generic crosswind AWES flying a generic trajectory is derived. The model considers centrifugal, elevation and gravity effects leaving the equations as a function of a generic trajectory. No model in the literature concerning the mentioned phenomena presents such a thorough approach to the analytical derivation and to the closure of the equations. The GeMo-KiTe can be helpful for the Airborne Wind Energy (AWE) researchers to study, in a conceptual design phase, the main physical effects of design quantities on system performance.

In Chapter 3, the model is applied for Fly Generation Airborne Wind Energy System (FG-AWES) flying a crosswind circular trajectory. The obtained equations are referred to as the Circular Model for Fly Generation Tethered Kites (CiMo-FG-KiTe). It allows a detailed understanding of how centrifugal forces, elevation and gravity affect the kite attitude and the system performance. Two contributions summarize how these three phenomena affect efficiency: power losses due to kite roll and power losses due to kite speed variation during the loop. The effects of elevation on power losses and, in particular, its coupling with gravity turn out to be extremely penalizing. All the discussion is performed as a function of two non-dimensional terms. The first, $M$, represents the ratio between centrifugal and aerodynamic forces. The second, $G_r$, represents the ratio between the gravity and centrifugal forces and has been introduced for the first time in this thesis. The chapter is useful for AWE community to enrich the basic physical knowledge about the main phenomena present in AWESs.

In Chapter 4, the analytical model proposed by Makani for FG-AWESs flying circular path is derived and discussed. The theoretical knowledge provided in Chapter 3 is exploited to compare Makani model with CiMo-FG-KiTe. The assumption made by Makani's team for which all the kite acceleration is due to the weight force, while the other forces are constantly in equilibrium, is too strong above certain values of $M$ and $G_r$. Moreover,

the power losses decoupling made by Makani's team does not catch the degrading effects due to the combination of gravity and elevation. The results of the chapter show that a further progress is made in the physics modeling through a low-fidelity model such as the CiMo-FG-KiTe (and so the GeMo-KiTe).

After having introduced the right framework in the previous four chapters, Chapter 5 shows how to exploit the GeMo-KiTe for a further understanding of AWESs physics and qualitatively propose solutions for performance enhancement. With this aim, a quasi-analytical model (ElMo-FG-KiTe) for a FG-AWES flying a crosswind elliptical trajectory is derived starting from the GeMo-KiTe. The results show that the elliptical path has the potential to increase performance especially when the power losses due to kite roll angle are relatively higher than those for kite speed variation. The higher is $G_r$, the more likely this condition is met. In addition to the qualitative results obtained for the ellipse, the approach shown in this chapter can be useful for AWE developers for future research on how to enhance performance with the prescription of non-circular trajectories.

# Bibliography

[1] Edward Anthony Wrigley. Energy and the English Industrial Revolution. *Philosophical Transactions of the Royal Society A: Mathematical, Physical and Engineering Sciences*, 371(1986):20110568, 2013.

[2] Antonello Cherubini. *Advances in Airborne Wind Energy and Wind Drones*. PhD thesis, Scuola Superiore Sant'Anna, 2017.

[3] IEA. Net Zero by 2050. `https://www.iea.org/reports/net-zero-by-2050`, 2021, Paris. (accessed November 8, 2021).

[4] Wikipedia contributors. George Pocock (inventor) - Wikipedia, The Free Encyclopedia, 2020. (accessed November 8, 2021).

[5] Loyd, Miles L. Crosswind Kite Power. *Journal of energy*, 4(3):106–111, 1980.

[6] Paula Echeverri, Tobin Fricke, Geo Homsy, and Nicholas Tucker on behalf of the Makani team. *The energy kite: Selected Results from the Design, Development and Testing of Makani's Airborne Wind Turbines. Part I*, 2020.

[7] Makani Team. *The energy kite: Selected Results from the Design, Development and Testing of Makani's Airborne Wind Turbines. Part II*, 2020.

[8] Makani Team. *The energy kite: Selected Results from the Design, Development and Testing of Makani's Airborne Wind Turbines. Part III*, 2020.

[9] IEA. IEA TASK 48. `https://iea-wind.org/task48/`. (accessed October 25, 2021).

[10] Jochem Weber, Melinda Marquis, Aubryn Cooperman, Caroline Draxl, Rob Hammond, Jason Jonkman, Alexsandra Lemke, Anthony Lopez, Rafael Mudafort, Mike Optis, et al. Airborne Wind Energy. Technical report, National Renewable Energy Laboratory, 2021.

[11] Kate Marvel, Ben Kravitz, and Ken Caldeira. Geophysical limits to global wind power. *Nature Climate Change*, 3(2):118–121, 2013.

[12] Cristina L. Archer. An Introduction to Meteorology for Airborne Wind Energy. In *Airborne Wind Energy* [71], pages 81–94.

[13] Cristina L Archer and Ken Caldeira. Global Assessment of High-Altitude Wind Power. *Energies*, 2(2):307–319, 2009.

[14] Philip Bechtle, Mark Schelbergen, Roland Schmehl, Udo Zillmann, and Simon Watson. Airborne Wind Energy Resource Analysis. *Renewable Energy*, 141:1103–1116, 2019.

[15] Zillmann, Udo and Petrick, Kristian and Thoms, Stefanie. Introduction to Airborne Wind Energy. `https://airbornewindeurope.org/wp-content/uploads/2020/07/AWEurope_Intro-Airborne-Wind-Energy_2020-03-23.pdf`, 2020. (accessed October 27, 2021).

[16] Marcelo De Lellis, Romeu Reginatto, Ramiro Saraiva, and Alexandre Trofino. The Betz limit applied to Airborne Wind Energy. *Renewable Energy*, 127:32–40, 2018.

[17] Antonello Cherubini, Andrea Papini, Rocco Vertechy, and Marco Fontana. Airborne Wind Energy Systems: A review of the technologies. *Renewable and Sustainable Energy Reviews*, 51:1461–1476, 2015.

[18] Lorenzo Fagiano and Mario Milanese. Airborne Wind Energy: An overview. In *2012 American Control Conference (ACC)*, pages 3132–3143. IEEE, 2012.

[19] Enerkite. `https://www.enerkite.de/en/`. (accessed October 8, 2021).

[20] SkySails Group. `https://skysails-group.com/`. (accessed October 8, 2021).

[21] Stephanie Mann. An Introduction to Airborne Wind. `https://ore.catapult.org.uk/analysisinsight/an-introduction-to-airborne-wind/`, 2020. (accessed October 10, 2021).

[22] Zeashan Khan and Muhammad Rehan. Harnessing Airborne Wind Energy: Prospects and challenges. *Journal of Control, Automation and Electrical Systems*, 27(6):728–740, 2016.

[23] Moritz Diehl. Airborne Wind Energy: Basic Concepts and Physical Foundations. In *Airborne Wind Energy* [71], pages 3–22.

[24] Marcelo De Lellis Costa de Oliveira. *Airborne Wind Energy with Tethered Wings: Modeling, Analysis and Control*. PhD thesis, Federal University of Santa Catarina, 09 2016.

[25] Massimo Canale, Lorenzo Fagiano, and Mario Milanese. Power Kites for Wind Energy Generation. *IEEE Control Systems Magazine*, 27(6):25–38, 2007.

[26] M. Canale, L. Fagiano, and M. Milanese. KiteGen: A revolution in wind energy generation. *Energy*, 34(3):355–361, 2009.

[27] Ahrens, Uwe. A breakthrough that could power the world. `https://www.slideshare.net/UweAhrens/xwind-presentation`. (accessed November 2, 2021).

[28] Ahrens, Uwe. The future of energy: X-Wind-technology. `https://www.slideshare.net/UweAhrens/the-future-of-renewable-energy-34347917`. (accessed November 10, 2021).

[29] AWESCO. `http://awesco.eu/awe-explained/`. (accessed October 10, 2021).

[30] Airborne Wind Energy Online. Experimental setup for automatic launching and landing of a 25 $m^2$ traction kite. `https://www.youtube.com/watch?v=w4oWs_zNpr8`, 2014. (accessed October 8, 2021).

[31] Skysails Group. SkySails Power: Operation of Airborne Wind Energy System. `https://www.youtube.com/watch?v=UZ82rK_RS4U`. (accessed October 8, 2021).

[32] Kitepower. `https://thekitepower.com/`. (accessed October 8, 2021).

[33] Ampyx Power. Ampyx Power 50 minutes fully automatic flight. `https://www.youtube.com/watch?v=oP8t4zHFxD0`, 2012. (accessed October 8, 2021).

[34] M Kruijff and R Ruiterkamp. Status and Development Plan of the PowerPlane of Ampyx Power, 2015.

[35] Sören Sieberling and Richard Ruiterkamp. The PowerPlane an Airborne Wind Energy System Conceptual Operations. In *11th AIAA Aviation Technology, Integration, and Operations (ATIO) Conference, including the AIAA Balloon Systems Conference and 19th AIAA Lighter-Than*, page 6909, 2011.

[36] Richard Ruiterkamp and Sören Sieberling. Description and Preliminary Test Results of a Six Degrees of Freedom Rigid Wing Pumping System. In *Airborne wind energy*, pages 443–458. Springer, 2013.

[37] Ampyx Power. `https://www.ampyxpower.com/`. (accessed October 8, 2021).

[38] Kitemill. `https://www.kitemill.com/`. (accessed October 8, 2021).

[39] TwingTec. `https://twingtec.ch/`. (accessed October 8, 2021).

[40] Skypull. Skypull Autonomous Flight TD. https://www.skypull.technology/media-video. (accessed October 8, 2021).

[41] Skypull. Skypull flight modes. https://www.skypull.technology/tech. (accessed October 8, 2021).

[42] Skypull. https://www.skypull.technology/. (accessed October 8, 2021).

[43] KiteGen. http://kitegen.com/. (accessed October 9, 2021).

[44] Makani Documentary. https://www.youtube.com/watch?v=qd_hEja6bzE. (accessed October 15, 2021).

[45] Makani. Makani flight test video collection. https://archive.org/details/makani-power, 2020. (accessed October 15, 2021).

[46] Makani. Makani - Energy Kite technical videos. https://www.youtube.com/playlist?list=PL7og_3Jqea4VRCZmMNK4LDH64sYgkLZzv, 2020. (accessed October 15, 2021).

[47] Makani. Makani code repositories. https://github.com/google/makani, 2020. (accessed October 15, 2021).

[48] Makani. Makani flight logs. https://console.cloud.google.com/marketplace/product/bigquery-public-datasets/makani-logs?pli=1, 2020. (accessed October 15, 2021).

[49] Makani. Makani simulation tool KiteFAST. https://github.com/rafmudaf/openfast/tree/kitefast, 2020. (accessed October 15, 2021).

[50] KiteKraft. Kitekraft All Phases of Flight. https://www.youtube.com/watch?v=42jvQpgfm94. (accessed October 9, 2021).

[51] KiteKraft. https://www.kitekraft.de/. (accessed October 9, 2021).

[52] Windlift. https://windlift.com/. (accessed October 9, 2021).

[53] Minesto. Minesto Faroe Islands Project. https://minesto.com/projects/faroe-islands. (accessed October 9, 2021).

[54] Minesto. Minesto video collection. https://www.youtube.com/channel/UCKkIlf3CMb_ejhh39jHg2Ug/videos. (accessed October 15, 2021).

[55] Minesto. https://minesto.com/. (accessed October 15, 2021).

[56] Kiteswarms. `https://www.kiteswarms.com/tether-technology/`. (accessed October 8, 2021).

[57] Kitenergy. `http://www.kitenergy.net`. (accessed October 9, 2021).

[58] eWind Solutions. `http://www.ewindsolutions.com/`. (accessed October 9, 2021).

[59] Windswept and Interesting Ltd. Windswept and Interesting Ltd. `https://windswept-and-interesting.co.uk/`. (accessed October 25, 2021).

[60] Fagiano, Lorenzo and Zgraggen, Aldo U. and Morari, Manfred. On Modeling, Filtering and Automatic Control of Flexible TetheredWings for AirborneWind Energy. In *Airborne Wind Energy* [71], pages 167–180.

[61] Horn, Greg and Gros, Sébastien and Diehl, Moritz. Numerical Trajectory Optimization for Airborne Wind Energy Systems Described by High Fidelity Aircraft Models. In *Airborne Wind Energy* [71], pages 205–218.

[62] Zanon, Mario and Gros, Sébastien and Diehl, Moritz. Model Predictive Control of Rigid-Airfoil Airborne Wind Energy Systems. In *Airborne Wind Energy* [71], pages 219–233.

[63] Malz, EC and Koenemann, J and Sieberling, S and Gros, S. A reference model for airborne wind energy systems for optimization and control. *Renewable Energy*, 140:1004–1011, 2019.

[64] Trevisi, Filippo and Gaunaa, Mac and McWilliam, Michael. Unified engineering models for the performance and cost of Ground-Gen and Fly-Gen crosswind Airborne Wind Energy Systems. *Renewable Energy*, 162:893–907, 2020.

[65] Filippo Trevisi, Mac Gaunaa, and Michael Mcwilliam. The Influence of Tether Sag on Airborne Wind Energy Generation. In *Journal of Physics: Conference Series*, volume 1618, page 032006. IOP Publishing, 2020.

[66] Rolf H Luchsinger. Pumping Cycle Kite Power. In *Airborne wind energy* [71], pages 47–64.

[67] Mihkel Talmar. Quasi-Steady Model Enhancements of Airborne Wind Energy Systems. Master's thesis, Delft University of Technology, 2021.

[68] Rolf van der Vlugt, Anna Bley, Michael Noom, and Roland Schmehl. Quasi-steady model of a pumping kite power system. *Renewable Energy*, 131:83–99, 2019.

[69] Trevisi, Filippo and Croce, Alessandro and Riboldi, Carlo E. D. Flight Stability of Rigid Wing Airborne Wind Energy Systems. *Energies*, 14(22), 2021.

[70] Wikipedia contributors. Ellipse - Wikipedia, the free encyclopedia. https://en.wikipedia.org/w/index.php?title=Ellipse&oldid=1051907505, 2021. (accessed October 27, 2021).

[71] Roland Schmehl, Uwe Ahrens, and Moritz Diehl. *Airborne Wind Energy*. Springer Berlin Heidelberg, 2013.

# List of Figures

# List of Tables

# Nomenclature

**Greek letters**

| | |
|---|---|
| $\alpha$ | Loop angle |
| $\ddot{\alpha}$ | Kite angular acceleration |
| $\dot{\alpha}$ | Kite angular speed |
| $\overline{\dot{\alpha}}$ | Kite angular velocity averaged on the loop angle $\alpha$ |
| $\beta$ | Elevation angle |
| $\tilde{\beta}$ | Mean elevation angle of the elliptical path having one focus in the center of the circular path from which it is derived |
| $\Delta$ | Additional kite inclination angle due to flying mass |
| $\eta\prime$ | Efficiency of a FG-AWES flying circular path derived with angular integration |
| $\eta$ | Efficiency of a generic AWES derived with the GeMo-KiTe |
| $\eta_{ce}$ | Efficiency considering the circular trajectory (Circular Model) |
| $\eta_{ci}$ | Efficiency of a FG-AWES flying circular path derived with the CiMo-FG-KiTe |
| $\eta_{ell}$ | Efficiency of a FG-AWES flying elliptical path derived with the ElMo-FG-KiTe |
| $\eta_{gr}$ | Efficiency of a GG-AWES flying a generic flight path |
| $\eta_{lin}$ | Efficiency considering the gravitational force during the linear trajectory (Linear Gravity Model) |
| $\eta_{on}$ | Efficiency of a FG-AWES flying a generic flight path |
| $\gamma$ | Inclination angle of the elliptical trajectory. It is defined as the angle between the major axis of the ellipse and the vertical direction and it is positive counterclockwise |
| $\gamma_{out}$ | Reel-out ratio |
| $\gamma_t$ | Ratio between drag given by on-board turbines and aerodynamic drag |

$\phi$ Kite tilt (or inclination) angle with respect to the plane of rotation. In the text, it is called as roll angle

$\Phi$ Opening angle of the cone generated by the tether motion

$\Phi_{ce}^{opt}$ Optimal opening angle derived analytically with the 'Centrifugal Model' (Section 2.3)

$\psi$ Kite tilt (or inclination) angle with respect to the radial direction in the plane of rotation. In the thesis, it is called as yaw angle

$\rho$ Air density

$\tau$ Reference time used for the adimensionalization of the time

$\overline{\zeta_v}$ Performance metric $\zeta_v$ averaged on the loop angle

$\zeta_L$ Ideal performance metric derived from Loyd [5]

$\zeta_v$ Performance metric for gravity losses due to kite speed fluctuation

**Other symbols**

$A$ Wing area of the kite. Sometimes in the document is called area of the kite

$a$ Semi-major axis of the elliptical trajectory

$b$ Semi-minor axis of the elliptical trajectory

$C$ Efficiency of Makani model comprehensive of centrifugal and gravity effects

$C_\beta$ Power coefficient related to elevation effects derived by Makani

$C_{ce}$ Power coefficient related to centrifugal effects derived by Makani

$C_{grav}$ Power coefficient related to gravity effects derived by Makani

$C_{grav}^{V}$ Power coefficient related to the gravity losses due to kite speed deviation from the optimal Loyd's value

$C_{grav}^{grid}$ Power coefficient related to the gravity losses due to the grid exploitation

$C_D$ Drag coefficient

$C_{D,t}$ Drag coefficient of the on-board wind turbines

$C_L$ Lift coefficient

$D$ Aerodynamic drag force of the kite

$D_t$ Aerodynamic drag force of the on-board turbines

| | |
|---|---|
| $E$ | Glide ratio or aerodynamic efficiency of the profile |
| $e$ | Eccentricity of the elliptical trajectory |
| $E_t$ | Glide ratio of the profile accounting for the drag of on-board turbines |
| $\Delta E_k$ | Variation of the kite kinetic energy during the trajectory |
| $\Delta E_p$ | Variation of the kite potential energy during the trajectory |
| $E_k$ | Average loop kinetic energy of the kite |
| $E_{k,id}$ | Kinetic energy of the kite flying in the ideal conditions |
| $F_g$ | Gravity force |
| $F_Y$ | Side forces due to the interaction between the wind and all the kite's components |
| $F_C$ | Centrifugal forces in the circular trajectory |
| $\eta_{FG}$ | Efficiency of a FG-AWES flying a generic trajectory |
| $\eta_{GG}$ | Efficiency of a GG-AWES flying a generic trajectory |
| $g$ | Gravity acceleration constant |
| $G_r$ | Gravity ratio. Ratio between the potential energy variation in the loop and the ideal kinetic energy or, alternatively, ratio between the gravity and centrifugal forces |
| $L$ | Aerodynamic lift force |
| $M$ | Non dimensional mass parameter. Ratio between the centrifugal and aerodynamic forces |
| $m$ | Flying mass |
| $\vec{\ddot{p}}$ | Kite acceleration vector |
| $\vec{\dot{p}}$ | Kite speed vector |
| $\vec{p}$ | Kite position vector |
| $P_0$ | Ideal power derived from Loyd [5] |
| $P_{ce}$ | Power production considering the centrifugal forces derived with the 'Centrifugal Model' |
| $P_{ci}$ | Power generation of a FG-AWES flying circular path derived with the CiMo-FG-KiTe |

$P_{FG}$ Power generation of a FG-AWES flying a generic trajectory

$P_{gr}$ Power generated at ground level

$P_{id}$ Power production of an ideal linear crosswind FG-AWES

$P_{lin}$ Power production considering the gravitational force during the linear trajectory (Linear Gravity Model)

$P_{on}$ Power generated on-board

$\ddot{r}$ Kite radial acceleration

$\dot{r}$ Kite radial speed

$R$ Radius of the circular trajectory

$r$ Kite radial position

$R_a$ Aerodynamic resultant force

$\vec{s}$ Span-wise unit vector directed toward the external wing tip

$s_x$ Axial component of the unit span-wise vector $\vec{s}$ describing the kite attitude

$s_r$ Radial component of the unit span-wise vector $\vec{s}$ describing the kite attitude

$s_\alpha$ Tangential component of the unit span-wise vector $\vec{s}$ describing the kite attitude

$T$ Traction force acting on the tether

$t$ Time

$T_{loop}$ Time interval in which the kite flies one full loop

$\Delta V_k$ Kite speed variation in the loop

$\overline{V_k}$ Average kite speed weighted on the loop angle

$V_\tau$ Speed felt by the leading edge of the airfoil

$V_k$ kite velocity

$V_w$ Wind velocity

$V_{k,L}$ Optimal Kite speed derived by Loyd [5]

$V_{out}$ Reel-out speed

$V_{w,eff}$ Effective aerodynamic wind speed hitting the airfoil on the pressure side. For readability it will be called only as effective aerodynamic wind speed or even effective wind speed

$V_a$ Relative wind velocity

$\ddot{x}$ Kite axial acceleration

$\Delta x$ Kite position in case of no reel-out

$\Delta x_{out}$ Kite axial displacement due to reel-out

$\dot{x}$ Kite axial speed

$x$ Kite axial position

# Acronyms

**AWE** Airborne Wind Energy. i, 1–3, 5, 8, 10, 11, 13, 15, 31, 105, 106, 113, 127

**AWES** Airborne Wind Energy System. 3, 6, 16, 19, 22, 29, 31, 62, 64, 87, 100, 105, 119, 129, 133

**AWESs** Airborne Wind Energy Systems. i, 1, 2, 5–8, 11, 15, 16, 23, 33, 55, 63, 101, 104–106, 113

**CiMo-FG-KiTe** Circular Model for Fly Generation Tethered Kites. 3, 33, 34, 37, 40, 41, 49, 57, 61, 63, 68, 72–74, 76–85, 105, 106, 114, 115, 117, 119, 121

**ElMo-FG-KiTe** Elliptical Model for Fly Generation Tethered Kites. 87, 89, 92, 93, 96, 106, 119

**FG** Fly Generation. 12, 19, 33

**FG-AWES** Fly Generation Airborne Wind Energy System. 3, 9, 16, 23, 29, 31, 33–35, 37, 49, 54, 61, 84, 87, 89–91, 105, 106, 119, 121, 122

**FG-AWESs** Fly Generation Airborne Wind Energy Systems. i, 3, 8, 9, 12, 13, 18, 105, 113

**GeMo-KiTe** Generic Model for Tethered Kites. 3, 16, 17, 31, 33, 34, 61, 63, 85, 87–89, 103, 105, 106, 119

**GG** Ground Generation. 11, 12

**GG-AWES** Ground Generation Airborne Wind Energy System. 9, 16, 23, 29, 31, 119, 121

**GG-AWESs** Ground Generation Airborne Wind Energy Systems. 3, 8, 9, 113

**GS** Ground Station. 8, 11, 12

**HAWT** Horizontal Axis Wind Turbine. 7, 64

**HAWTs** Horizontal Axis Wind Turbines. 5–7

**HTOL** Horizontal Take-Off and Landing. 12

**LCOE** Levelized Cost Of Electricity. 7

**NREL** National Renewable Energy Laboratory. 2

**VTOL** Vertical Take-Off and Landing. 12, 13

# Acknowledgements

I want to acknowledge Università di Pisa, which taught me the right approach to face many challenges of the academic world. Thanks to my friends from Pisa, an incredible team with whom I am glad to share university and non-university memories. Thanks for the many laughs we had together. Thanks to Prof. Pietro Maria Scipione Galbiati, who introduced me to the world of physics, I still remember the time spent in face-to-face discussions to speculate on the most disparate concepts. Thanks to Prof. Daniele Testi who makes my passion for energy alive.

I acknowledge Politecnico di Milano, which allowed me to broaden my vision of the energy sector and to focus my studies on renewable energy. I have met wonderful friends who have taught me so many things that I hope to always carry with me. I acknowledge my advisor Prof. Alessandro Croce and co-advisors Prof. Carlo Emanuele Dionigi Riboldi and Filippo Trevisi for allowing me to write this work and discover AWE. In particular, thanks to Filippo who helped me throughout the work and with whom I sincerely hope to stay in touch also in the future. I only became aware of this sector nine months ago, but my passion has grown and I hope this thesis is just the beginning of a new journey.

Thanks to old friends from my city, Livorno. For all the moments of fun and reflection over the years.

Thanks to my family that allows me to live such an incredible university experience and that supported my studies in Milan. Thanks, mom and dad. Thank you, brother and sisters. Thanks to all the other components.

Thanks to my girlfriend, Matilde, for understanding me in times of pressure, for trying to cheer me up in times of difficulty and for rejoicing with me in times of happiness. I hope to give you at least half of what you have given me so far.

# A | Derivation of the models in Sections 2.1, 2.2, 2.3

## A.1. Derivation of the Linear Ideal Model

The power production of a generic ideal AWES can be expressed as:

$$P = P_{ob} + P_{gr} = \vec{D_t} \cdot \vec{V_a} + \vec{T} \cdot \vec{V_{out}} \tag{A.1}$$

where $P_{ob}$ is the power generated by the on-board turbine and $P_{gr}$ is the ground generated power. With reference to Figure 2.2, the ratio between the lift and drag force acting on the kite is:

$$\frac{V_\tau}{V_w \cos\beta(1-\gamma_{out})} = \frac{L}{D_t + D} = \frac{C_L}{C_{D,t} + C_D} = E_t \tag{A.2}$$

Defining $\gamma_{out} = \frac{V_{out}}{V_w \cos\beta}$ and from Figure 2.2, Equation A.2 and assumption (ii), the relative wind speed is:

$$V_a = V_w \cos\beta E_t^2 (1-\gamma_{out}) \tag{A.3}$$

The productive drag of the on-board turbines is $D_t = \frac{1}{2}\rho A \gamma_t C_D V_a^2$. Therefore, substituting Equation A.3, the on-board generated power is:

$$P_{ob} = \frac{1}{2}\rho A \gamma_t C_D V_w^3 \cos\beta^3 E_t^3 (1-\gamma_{out})^3 \tag{A.4}$$

From Figure 2.2, $T = R_a$ which is the vectorial sum of lift and drag:

$$T = \frac{1}{2}\rho A C_D (1+\gamma_t)(1-\gamma_{out})^2 V_w^2 \cos\beta^2 E_t^3 \tag{A.5}$$

The product between the latter and $V_{out}$ gives the ground generated power:

$$P_{gr} = \frac{1}{2}\rho A C_D (1+\gamma_t)\gamma_{out}(1-\gamma_{out})^2 V_w^3 \cos\beta^3 E_t^3 \tag{A.6}$$

From Equation A.1, the total generated power is:

$$P_{id} = \frac{1}{2}\rho A C_D (1-\gamma_{out})^2 V_w^3 \cos\beta^3 E_t^3 \Big[\gamma_t(1-\gamma_{out}) + \gamma_{out}(1+\gamma_t)\Big] \tag{A.7}$$

## A.2. Derivation of the Linear Gravity Model

Considering the angle $\Delta$ (Equation 2.2), the relative wind speed is:

$$V_a = V_w E_t \left[\cos(\beta+\Delta) - \gamma_{out}\cos\beta\cos\Delta\right] \tag{A.8}$$

From Figure 2.3, the resultant aerodynamic force is obtained from the vectorial sum of lift and drag:

$$R_a = \frac{1}{2}\rho A C_D (1+\gamma_t) V_w^2 E_t^3 \Big[\cos(\beta+\Delta) - \gamma_{out}\cos\beta\cos\Delta\Big]^2 \tag{A.9}$$

From Figure 2.3, the force balances along the $x_t$ and $y_t$ axes respectively are:

$$\begin{cases} T = R_a\cos\Delta - F_g\sin\beta & \text{(A.10a)} \\ R_a\sin\Delta - F_g\cos\beta = 0 & \text{(A.10b)} \end{cases}$$

The tether traction force is $T = R_a\eta_\Delta$ where $\eta_\Delta = \cos\Delta - \sin\Delta\tan\beta$ ($\eta_\Delta = 1$ for $\Delta = 0°$). Therefore, the ground generated power is the product between the tether traction and the reel-out speed:

$$P_{gr} = \frac{1}{2}\rho A C_D (1+\gamma_t) V_w^3 E_t^3 \cos\beta\gamma_{out}\eta_\Delta \Big[\cos(\beta+\Delta) - \gamma_{out}\cos\beta\cos\Delta\Big]^2 \tag{A.11}$$

The on-board generated power is the product between the productive drag of the on-board turbines and the relative wind speed:

$$P_{ob} = \frac{1}{2}\rho A \gamma_t C_D V_w^3 E_t^3 \Big[\cos(\beta+\Delta) - \gamma_{out}\cos\beta\cos\Delta\Big]^3 \tag{A.12}$$

Therefore, the total generated power considering the gravity force is the sum between $P_{gr}$ and $P_{on}$:

$$\begin{aligned} P_{lin} = \frac{1}{2}\rho A C_D \Big[\cos(\beta+\Delta) - \gamma_{out}\cos\beta\cos\Delta\Big]^2 V_w^3 E_t^3 \cdot \\ \cdot \Big\{\gamma_t\Big[\cos(\beta+\Delta) - \gamma_{out}\cos\beta\cos\Delta\Big] + (1+\gamma_t)\gamma_{out}\eta_\Delta\cos\beta\Big\} \end{aligned} \tag{A.13}$$

The efficiency is:

$$\begin{aligned} \eta_{lin} = \frac{P_{lin}}{P_{id}} = \frac{\Big[\cos(\beta+\Delta) - \gamma_{out}\cos\beta\cos\Delta\Big]^2}{\cos\beta^3(1-\gamma_{out})^2} \cdot \\ \cdot \frac{\gamma_t\Big[\cos(\beta+\Delta) - \gamma_{out}\cos\beta\cos\Delta\Big] + (1+\gamma_t)\gamma_{out}\eta_\Delta\cos\beta}{\gamma_t(1-\gamma_{out}) + \gamma_{out}(1+\gamma_t)} \end{aligned} \tag{A.14}$$

## A.3. Derivation of the Centrifugal Model

The starting point for the model derivation is the definition of the relative wind speed, $\vec{V_a}$:

$$\vec{V_a} = \begin{pmatrix} V_x \\ V_r \\ V_\alpha \end{pmatrix} = \begin{pmatrix} V_w\cos\beta(1-\gamma_{out}) \\ -V_w\sin\beta\sin\alpha \\ -V_w\sin\beta\cos\alpha - \dot{\alpha}R \end{pmatrix} \tag{A.15}$$

where $\gamma_{out} = \frac{V_{out}}{V_w\cos\beta}$, $V_x$, $V_r$ and $V_\alpha$ are the relative wind speed components along the $x$, $r$ and tangential axes respectively. Since the model is derived in case of no elevation, the relative wind velocity becomes:

$$\vec{V_a} = \begin{pmatrix} V_w(1-\gamma_{out}) \\ 0 \\ -\dot{\alpha}R \end{pmatrix} \tag{A.16}$$

With assumption (iii), the magnitude of the relative wind velocity becomes:

$$|\vec{V_a}| \approx \dot{\alpha}R \tag{A.17}$$

The lift force is defined as:

$$\vec{L} = \begin{pmatrix} L_x \\ L_r \\ L_\alpha \end{pmatrix} = \frac{1}{2}\rho A C_L |\vec{V_a}| \vec{V_a} \times \vec{s} = \frac{1}{2}\rho A C_L (\dot{\alpha} R) \begin{pmatrix} V_r s_\alpha - V_\alpha s_r \\ V_\alpha s_x - V_x s_\alpha \\ V_x s_r - V_r s_x \end{pmatrix} \tag{A.18}$$

Substituting Equation A.16 into Equation A.18 and collecting $(\dot{\alpha}R)$:

$$\vec{L} = \frac{1}{2}\rho A C_L (\dot{\alpha} R)^2 \begin{pmatrix} s_r \\ -s_x - \frac{V_w(1-\gamma_{out})}{\dot{\alpha}R} s_\alpha \\ \frac{V_w(1-\gamma_{out})}{\dot{\alpha}R} s_r \end{pmatrix} \tag{A.19}$$

The drag force is defined as:

$$\vec{D} = \begin{pmatrix} D_x \\ D_r \\ D_\alpha \end{pmatrix} = \frac{1}{2}\rho A C_D (1+\gamma_t) |\vec{V_a}| \vec{V_a} = \frac{1}{2}\rho A C_D (1+\gamma_t)(\dot{\alpha} R) \begin{pmatrix} V_x \\ V_r \\ V_\alpha \end{pmatrix} \tag{A.20}$$

Substituting the apparent velocity $\vec{V_a}$ (Equation A.16) into Equation A.20 and collecting $\dot{\alpha}R$:

$$\vec{D} = \frac{1}{2}\rho A C_D (1+\gamma_t)(\dot{\alpha} R)^2 \begin{pmatrix} \frac{V_w(1-\gamma_{out})}{\dot{\alpha}R} \\ 0 \\ -1 \end{pmatrix} \tag{A.21}$$

The equations underlying the model are:

$$\begin{cases} \vec{s} \cdot \vec{V_a} = s_x V_x + s_r V_r + s_\alpha V_\alpha = 0 & \text{(A.22a)} \\ |\vec{s}|^2 = s_x^2 + s_r^2 + s_\alpha^2 = 1 & \text{(A.22b)} \\ L_x + D_x - T\cos\Phi = 0 & \text{(A.22c)} \\ L_r + D_r - T\sin\Phi + mR\dot{\alpha}^2 = 0 & \text{(A.22d)} \\ L_\alpha + D_\alpha = 0 & \text{(A.22e)} \end{cases}$$

where the Equation A.22a represents assumption (xi), Equation A.22b is for the unit vector definition and Equations A.22c, A.22d and A.22e represent the force balance along the axial, radial and tangential axes respectively. With the procedure present in [65], it is possible to obtain the on-board generated power as the product between $\vec{D_t} = \frac{1}{2}\rho A \gamma_t C_D V_a \cdot \vec{V_a}$ and $\vec{V_a}$:

$$P_{on} = \frac{1}{2}\rho A \gamma_t C_D (\dot{\alpha} R)^3 \tag{A.23}$$

Still referring to [65], the ground generated power is $P_{gr} = T \cos\Phi V_{out}$ and can be expressed as:

$$P_{gr} = \frac{1}{2}\rho A C_D (1+\gamma_t)(\dot{\alpha} R)^3 \frac{\gamma_{out}}{1-\gamma_{out}} \tag{A.24}$$

Therefore, the total power harvested by a generic AWES flying a crosswind circular trajectory if only centrifugal forces are considered is:

$$P_{ce} = \frac{1}{2}\rho A C_D (\dot{\alpha} R)^3 \left[\gamma_t + (1+\gamma_t)\frac{\gamma_{out}}{1-\gamma_{out}}\right] \tag{A.25}$$

The efficiency $\eta_{ce}$ is the ratio between $P_{ce}$ and $P_{id}$ (Equation 2.1):

$$\eta_{ce} = \frac{P_{ce}}{P_{id}} = \left(\frac{\dot{\alpha} R}{V_w E_t (1-\gamma_{out})}\right)^3 \tag{A.26}$$

Solving the system following the procedure made by Trevisi et al. in [65], it is possible to obtain the kite tangential speed:

$$\dot{\alpha} R = V_w E_t (1-\gamma_{out}) \cos\Phi \left[M + \sqrt{1 - \frac{M^2}{\tan\Phi^2}}\right] \tag{A.27}$$

Substituting the last equation into Equation A.26:

$$\eta_{ce} = \cos\Phi^3 \left(M + \sqrt{1 - \frac{M^2}{\tan\Phi^2}}\right)^3 \tag{A.28}$$